Nano Energy 128 (2024) 109872

Contents lists available at ScienceDirect

Nano Energy

journal homepage: www.elsevier.com/locate/nanoen

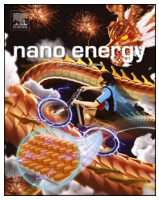

Review

Emerging Strategies to Achieve Interfacial Solar Water Evaporation Rate Greater than 3 kg·m^{-2}·h^{-1} under One Sun Irradiation

Anastasiia Taranova [a], Elisa Moretti [a], Kamran Akbar [a,*], Ghulam Dastgeer [b,*], Alberto Vomiero [a,c,**]

[a] Department of Molecular Sciences and Nanosystems, Ca' Foscari University of Venice, Via Torino 155, Venezia Mestre 30172, Italy
[b] Department of Physics and Astronomy, Sejong University, Seoul 05006, South Korea
[c] Division of Materials Science, Department of Engineering Sciences and Mathematics, Luleå University of Technology, Luleå SE-971 87, Sweden

ARTICLE INFO

Keywords:
Solar steam generation
Water evaporation
Photothermal materials
2D evaporators
3D evaporators
Energy conversion

ABSTRACT

Solar water evaporation is vital for addressing global water scarcity, particularly in regions with limited freshwater. Through the utilization of photothermal materials, solar water evaporation harnesses solar radiation to generate heat, which in turn accelerates the evaporation of water, producing clean drinking water. Subsequently, the vapor is condensed to produce fresh water, offering a sustainable solution to water scarcity. This research field has garnered immense scientific interest, with over six thousand publications. Reported solar absorber evaporation rates exceed 100 kg m^{-2} h^{-1} under one sun irradiation, far surpassing the theoretical limit of 1.47 kg m^{-2} h^{-1} achievable on two-dimensional absorber surfaces, assuming constant latent heat at 2444 J g^{-1}. This review addresses this significant discrepancy in theoretical and practical values. A cut-off of 3 kg m^{-2} h^{-1} (under one sun irradiation) is considered to narrow focus, facilitating analysis of high-rate evaporators. Critical challenges and factors contributing to high evaporation rates are discussed, providing comprehensive insights into field advancements.

1. Introduction

With the world's population continuing to grow and climate change causing more frequent droughts and water shortages, the need for clean water is becoming increasingly urgent. According to the United Nations [1], more than 2.3 billion people live in countries experiencing high water stress. Desalination is removing salt and other minerals from seawater or brackish water to produce fresh water. The development of sustainable methods to obtain freshwater has become paramount, and in this context, solar water evaporation has emerged as a promising approach among various water desalination technologies [2,3]. Water desalination plays a vital role (though not conclusive for all the 2.3 billion people mentioned above) in addressing the challenges posed by freshwater scarcity, particularly in arid regions and coastal areas abundant in seawater. Reverse osmosis (RO) remains the prevalent method of desalination, particularly in regions such as the United Arab Emirates, Saudi Arabia, and Israel. RO is a high-consumption energy process, so the development of alternative and complementary technologies for water desalination is crucial [4–6]. In this respect, solar water evaporation represents an appealing alternative approach that harnesses the abundant and clean energy from the sun [7,8]. The energy efficiency of solar steam evaporation (20–30 %) is relatively lower compared to reverse osmosis technology (70–90 %) primarily because of the indirect heating method employed in solar steam evaporation. Nevertheless, ongoing advancements in solar thermal technologies are steadily improving efficiency levels. By utilizing solar energy to drive the evaporation process, this method offers the potential for an environmentally sustainable solution to freshwater production. Solar evaporation capitalizes on natural energy sources to evaporate water, separating it from salts and impurities and enabling the collection of clean freshwater. The solar vapour generation approach holds immense promise for mitigating water scarcity challenges while minimizing the reliance on energy-intensive and environmentally taxing methods.

The solar evaporation can be a viable solution for addressing water scarcity due to several key factors. Firstly, solar energy is widely available and renewable, providing a sustainable power source for the

* Corresponding authors.
** Corresponding author at: Department of Molecular Sciences and Nanosystems, Ca' Foscari University of Venice, Via Torino 155, Venezia Mestre 30172, Italy.
E-mail addresses: kamran.akbar@unive.it (K. Akbar), gdastgeer@sejong.ac.kr (G. Dastgeer), alberto.vomiero@ltu.se (A. Vomiero).

https://doi.org/10.1016/j.nanoen.2024.109872
Received 5 April 2024; Received in revised form 6 June 2024; Accepted 7 June 2024
Available online 13 June 2024

evaporation process [9]. Unlike conventional desalination methods that often rely on fossil fuels or electricity, solar evaporation harnesses the natural heat and light from the sun, making it environmentally friendly and cost-effective in the long run. It is important to note, however, that solar energy availability varies depending on factors such as weather conditions and time of day. While solar energy is abundant during daylight hours, other sources of clean energy, such as wind and hydroelectric power (or even solar energy through photovoltaic cells), can complement solar energy to ensure a consistent and reliable power supply for water desalination processes [10–12]. Additionally, solar evaporation systems are often noted for their relatively straightforward in design and operation, which can translate to reduced infrastructure demands and maintenance requirements compared to complex desalination plants. This inherent simplicity renders solar evaporation especially well-suited for deployment in remote or off-grid areas where conventional water treatment facilities may be lacking. However, the spatial footprint or land area needed for maximizing solar energy capture, a crucial aspect of solar evaporation systems, varies depending on factors such as solar irradiance, climate conditions, and system efficiency. Detailed assessments of floor space requirements are essential for effectively implementing solar evaporation technology at large scale but are out of the scopes of this review. Furthermore, solar evaporation has the advantage of utilizing a natural evaporation cycle, which inherently purifies water by leaving behind salts and impurities, resulting in cleaner freshwater for various applications [13,14]. The viability of solar evaporation lies in its compatibility with renewable energy, simplicity of implementation, and its inherent water purification capabilities, making it an attractive and sustainable solution to address water scarcity challenges [11,15,16].

There are different categories of solar water evaporation based on the material and device design, such as interfacial solar evaporation, where photothermal materials float at the water-air interface [17]; bulk solar evaporation, where photothermal materials immersed in the water body to heat the entire water volume; membrane-based solar evaporation, where the porous membrane separates the photothermal materials from the water body and allow only vapor to pass through [18]; hierarchical solar evaporation, where multiple layers of materials manage water transportation, restriction, and evaporation [19]. This review focuses on the interfacial solar evaporation process. One of the advantages of interfacial solar evaporation over other categories is its ability to achieve high energy conversion efficiency, which is facilitated by strategically placing photothermal materials near the evaporation surface to localize heat and reduce heat loss to the environment, resulting in significantly enhanced steam production. Another advantage is that it can avoid or mitigate the scaling problem by separating the photothermal materials from the water body or using anti-fouling coatings. Scaling is the accumulation of salt or mineral deposits on the surface of the materials, which can reduce their performance and durability. Interfacial solar evaporation can also produce high-quality freshwater with low salinity and impurities, as well as harvest atmospheric water from humid air.

Interfacial solar water evaporation offers the possibility to utilize both two-dimensional (2D) and three-dimensional (3D) evaporators as shown in Fig. 1. 2D evaporators are planar structures that fully face or are parallel to the water surface. Various photothermal materials, such as carbon-based materials, metal-based materials, or hybrid materials are used as 2D evaporators [20–23]. 3D evaporators (usually porous materials, such as sponges, fabrics, or foams, coated with photothermal materials) are structures that are perpendicular to the water surface or suspended above the bulk water. Under one sun irradiation (standard air mass 1.5 global, AM 1.5 G, 100 mW•cm^{-2}) and assuming 100 % solar-to-vapor energy transfer efficiency, a 2D solar evaporator can achieve a theoretical maximum evaporation rate of 1.47 kg m^{-2} h^{-1} considering that the latent heat of water evaporation remains constant at 2444 J•g^{-1} [24,25]. Despite this theoretical limit, a recent study reported the evaporation rate of 126.5 kg m^{-2} h^{-1} exceeding the limit [26]. Purpose of this review is to critically analyze published high evaporation rates beyond theoretical limits, therefore a cutoff at 3 kg m^{-2} h^{-1} has been utilized. We will discuss key challenges associated with calculations, thermodynamic considerations, and strategies to surpass theoretical limits.

1.1. How 3D evaporators get an unfair advantage over 2D evaporators

In the pursuit of enhancing interfacial solar water evaporation rates, it is crucial to critically evaluate the methodologies used for calculating evaporation rates, particularly concerning the comparison between 2D and 3D evaporators. The formula utilized to calculate the evaporation rate for both 2D and 3D evaporators is shown in Eq. (1).

$$\dot{m} = \frac{\Delta m}{S} \tag{1}$$

where $\dot{m}$ - evaporation rate [kg m^{-2} h^{-1}]; Δm - the amount of evaporated water under solar irradiation in one hour [kg h^{-1}]; S - the surface area of the evaporator [m^2].

According to the current model in the field, the evaporation rate is

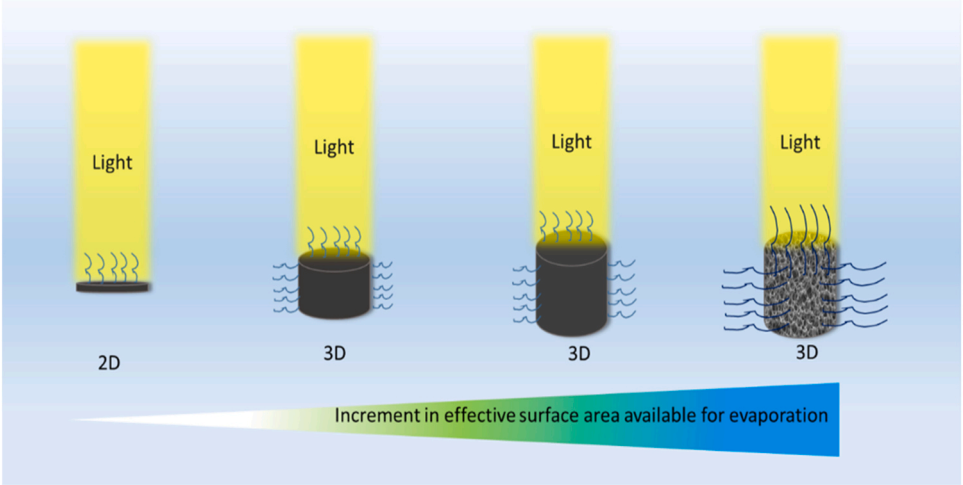

Fig. 1. Schematic illustration of increment in the effective surface is with a constant projected area of illumination. From left to right: The 2D surface experiences only top surface evaporation, the 3D evaporator next to 2D also exhibits side area evaporation on top of evaporation from its top surface. In the third case the side evaporation surface area is increased via increased z-direction and lastly in the porous 3D structure evaporation also occurs from inside its pores.

calculated based on the projected area of illumination (see Fig. 1) [27]. Although it is noticeable that the projected area of illumination is the same for all evaporators, the effective area of evaporation kept increasing from left to right – more water can evaporate from the surface of some evaporators than others. However, Eq. (1) considered the projected area of illumination as the denominator, which is constant for all evaporators, instead of the effective area of evaporation. This leads to artificially high evaporation rates for 3D evaporators, as the numerator in Eq. (1) increases from left to right (Fig. 1), while giving 2D evaporators a disadvantage. This also prevents a fair comparison between 2D and 3D evaporators. This convention essentially puts the 2D evaporators at a disadvantage in terms of "record-breaking" water evaporation rates attained by 3D counterparts. Therefore, we suggest using the entire surface area of the evaporator as the denominator in the evaporation rate calculations, rather than the projected area of illumination.

Another crucial factor that is often overlooked, and that would enable a more valid comparison of results from different studies, is the measurement of the evaporation rate without illumination (in the dark). This should be considered when calculating the net evaporation rate under illumination, using Eq. (2).

$$\dot{m}_{net} = \dot{m}_{sun} - \dot{m}_{dark} \tag{2}$$

where $\dot{m}_{net}$ – net evaporation rate [kg m^{-2} h^{-1}]; $\dot{m}_{sun}$ – evaporation rate under sun illumination, [kg m^{-2} h^{-1}]; $\dot{m}_{dark}$ – evaporation rate in the dark condition [kg m^{-2} h^{-1}].

This method eliminates the influence of the projected area, as it only focuses on the effect of sunlight on evaporation rate while keeping other factors such as environmental energy harvesting, wind speed, enthalpy reduction, etc. constant for both scenarios. Only a few publications considered thoroughly these issues, when determining the evaporation rate under simulated solar light. For instance, Gao et al [28] reported an evaporation rate of 7.6 kg m^{-2} h^{-1} of a 3D evaporator under one sun irradiation. However, under dark conditions, their evaporator already exhibits an evaporation rate of 5.0 kg m^{-2} h^{-1} which in turn means the net evaporation rate induced by solar light was only 2.6 kg m^{-2} h^{-1}, which is typically achieved by most 2D evaporators. Therefore, we strongly suggest either avoiding the use of the projected area of illumination or, if it is used, then reporting and subtracting the evaporation rate without light illumination to obtain the net evaporation rate for a fair comparison between different reports. There can however be one concern associated when dealing with dark area evaporation rate subtraction. This is because in dark evaporation, all surfaces have a lower temperature than the ambient temperature, resulting in energy harvesting from the surroundings.

1.2. Past gap and objectives

The emergence of solar water evaporation as a viable solution to global water scarcity has been met with both excitement and scrutiny within the scientific community. Despite the promising potential of this technology, a significant gap has persisted between theoretical predictions and practical achievements in terms of evaporation rates [29–32]. While theoretical models suggest a maximum evaporation rate of 1.47 kg m^{-2} h^{-1} for 2D absorber surfaces under one sun irradiation, empirical data from reported studies have demonstrated evaporation rates exceeding 100 kg m^{-2} h^{-1}. Dang et al. [26] performed 35 cm-high multichannel photothermal rod array, which achieved an evaporation rate of 126.5 kg m^{-2} h^{-1} in an outdoor environment. This vast discrepancy underscores the need for a comprehensive review to bridge the gap between theoretical predictions and experimental observations in the field of solar water evaporation.

The primary objective of this review is to address the discrepancy between theoretical and practical values of solar water evaporation rates. By considering a cutoff of 3 kg m^{-2} h^{-1} under one sun irradiation, we aim to narrow our focus to high-rate evaporators and systematically analyze the critical challenges and factors contributing to their enhanced performance. Through a thorough examination of recent advancements in the field, we seek to provide comprehensive insights into the mechanisms underlying high evaporation rates and identify potential avenues for further research and development. By elucidating the key factors driving the discrepancy between theoretical and practical values, this review aims to contribute to a deeper understanding of solar water evaporation and facilitate the development of more efficient and sustainable water desalination technologies.

2. Strategies to improve the evaporation rate

Achieving high evaporation rates is crucial for enhancing the efficiency and effectiveness of solar water evaporation systems. Various strategies have been developed to achieve higher evaporation rates while addressing key challenges inherent in the process. One fundamental approach involves optimizing water transport mechanisms to ensure uniform distribution of water across the evaporator surface. This can be achieved through the implementation of capillary structures, microfluidic channels, or porous materials designed to facilitate the efficient movement of water molecules to the evaporation site. Additionally, lowering the enthalpy of water evaporation is essential for reducing the energy required to vaporize water molecules. Strategies such as surface engineering to enhance wettability, employing hydrophilic coatings, or incorporating nanostructured materials can help decrease the energy barrier for evaporation, resulting in higher evaporation rates. From optimizing water transport mechanisms to harnessing environmental energy sources, each strategy plays a pivotal role in maximizing the performance of solar evaporation technologies.

In this section, we will explore the strategies employed to achieve high evaporation rates, addressing pertinent challenges along the way.

2.1. Efficient water transport

Efficient water transport is crucial for achieving higher evaporation rates as it leads to continuous water supply to the heated regions of evaporators. This is especially true for 3D evaporators since the water needs to travel a longer distance within them. Water is transported within evaporators via capillary action and/or with the help of hydrophilic regions present in the evaporator. Hydrophilicity can be improved by chemical treatments that attach functional groups such as –OH and –COOH, which have a high affinity for water molecules. To improve water transport via capillary action, smaller-sized channels perform better than larger-sized water channels. Various structures exhibit better water transport, such as structures with microporous channels and hydrophilic contacts. Various natural carbonaceous materials, such as wood, carbonized wood or organic matter, and hydrogels, are typical examples of materials with efficient water transport. As a result, such materials are among the materials that show a high evaporation rate above 3.

Numerous bio-derived materials exhibit excellent evaporation rates, for instance, Bian et al. [33] utilized the 3D carbonized bamboo and attained an evaporation of 3.13 kg m^{-2} h^{-1} under 1 sun illumination. The structure is depicted in Fig. 2 (a–c): carbonized bamboo possesses a porous structure with numerous side branches and shows excellent water transport due to partial pumping. Another advantage of this design is that it allows confined evaporation within the smaller branched network. This lowers the enthalpy requirement for evaporation (more about enthalpy reduction in the next section), which translates into higher evaporation efficiency and evaporation rates. The authors further compare the performance of 2D carbonized bamboo with its 3D counterpart (Fig. 2 (d–j)). 2D carbonized bamboo achieved an evaporation rate of 1.547 kg m^{-2} h^{-1} suggesting that growth in z-direction in 3D bamboo also plays a significant role in achieving higher efficiency.

Feng et al. [34] investigated the development of solar water

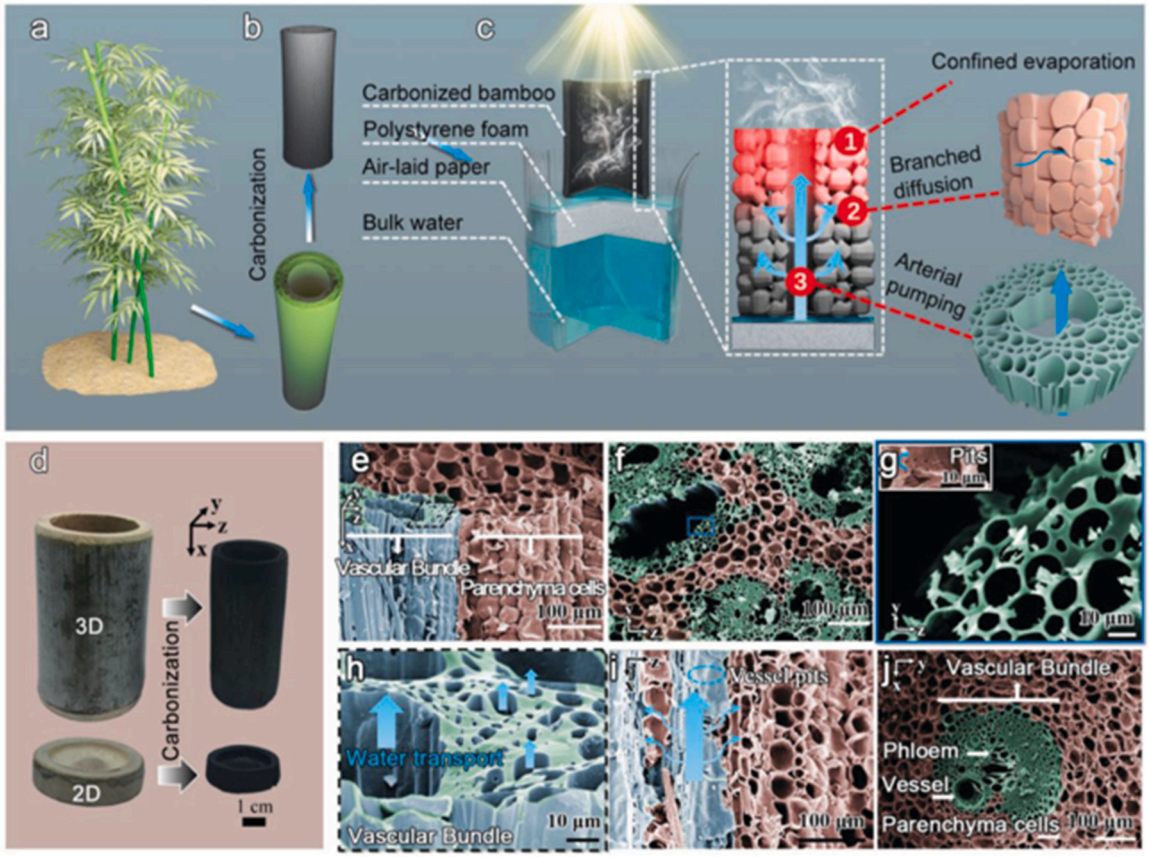

Fig. 2. The illustration of the design concept for a bamboo-based solar vapor-generation device. (a) Water transport from the bottom upward and photosynthesis by absorbing sunlight. (b) Cutting of bamboo perpendicular to the growth direction and controllable carbonization. (c) Illustration of a carbonized bamboo-based 3D solar vapor-generation device. The evaporation of water confined in the bamboo mesh increases under sunlight. The vapor can be supplied via 1) branched water diffusion, 2) pumping, 3) based on the parenchyma cells and vascular bundles. (d) The natural bamboo before and after carbonization. (e) Artificially colored SEM (scanning electron microscopy) images of the carbonized bamboo in the x, y, and z directions. (f) SEM images of the y–z plane presenting the rated distribution of the vascular bundle. (g, h) The fast longitudinal water transport channels from the magnified SEM images (e, f). Cross-transport of water is provided by pits on the cell walls shown in the inset (g) image. (i) Longitudinal SEM images of the carbonized bamboo. (j) Cross-section of the carbonized bamboo. The vascular bundles are incorporated in the parenchyma. Reproduced with permission from Ref. [33]. Copyright Wiley, 2019.

evaporators using sunflower stalks and discovered that evaporators containing stem pith exhibited superior performance. These evaporators (with a height of 16 cm) achieved an impressive evaporation rate of 11.62 kg m^{-2} h^{-1} and an energy efficiency of 344.69 %. The carbonization process implemented during fabrication modified the pore size and wettability of the carbonized biochar, thereby enhancing the water transport capability of the evaporator. This transformation, coupled with the optimization of design parameters such as carbonization temperature and evaporator height, contributed to the exceptional evaporation rate observed. The study highlights the importance of stem pith and the carbonization process in enhancing the performance of biomass-derived solar water evaporators, presenting promising implications for sustainable water treatment applications.

Hydrogels possess not only a microporous structure but also excellent hydrophilicity making them ideal for solar water evaporation. Most of the hydrogels are transparent materials and thus are combined with black absorber materials before utilization in solar water evaporation experiments. Further, hydrogels have low thermal conductivity, which improves energy conversion efficiency as low thermal conductivity minimizes heat loss and allows heat concentration. Working on similar lines of vertical pores within hydrogel structures, Li et al. [35] reported an evaporation rate of 6.35 kg m^{-2} h^{-1} under one sun. The improvement here was based on the reduction in the size of microporous channels: narrower channels possess stronger capillary forces and thus provide rapid water transport compared to wider channels. PVA/Ti_3C_2 (polyvinyl alcohol/Ti_3C_2) composite hydrogels with different pore sizes were employed as shown in Fig. 3 (a, b). Ti_3C_2 was chosen for its photothermal conversion efficiency close to 100 %. The best-performing system has a height of 8 cm with pore sizes in the sub-micron range (Ti_3C_2-PVA-0 h). It is interesting that the height of hydrogels also shows a significant effect on the evaporation rate. For instance, Ti_3C_2-PVA-0 h with a height of 1 cm showed an evaporation rate of 1.94 kg m^{-2} h^{-1} while the same sample with 8 cm of height showed an evaporation rate of 6.35 kg m^{-2} h^{-1} (Fig. 3 (c–f)). On the other hand, the Ti_3C_2-PVA-2 h having larger pore sizes show an evaporation rate of 5.38 kg m^{-2} h^{-1} proving that increasing area in 3D can improve the performance.

Excellent hydrophilicity can also be found in inorganic structures. Ding et al. [36] utilized conventional inexpensive ordinary chalk and ink, which avoids the need for pricey raw materials and specialized equipment. This strategy is especially well suited for less developed locations where access to sophisticated fabrication techniques and expensive resources may be limited. The fundamental breakthrough is the invention of ink-stained chalk (ISC), which benefits from chalk's outstanding hydrophilicity and black ink's strong sunlight absorption. Under one sun exposure, the resultant ISC displays an outstanding evaporation rate of up to 20.49 kg m^{-2} h^{-1}. Furthermore, the researchers use the ISC to successfully desalinate real seawater samples, demonstrating very effective (8.97–19.91 kg m^{-2} h^{-1}) and stable (24-hour) sun desalination capabilities. This achievement opens the door to the construction of 3D solar evaporators that enable low-cost and

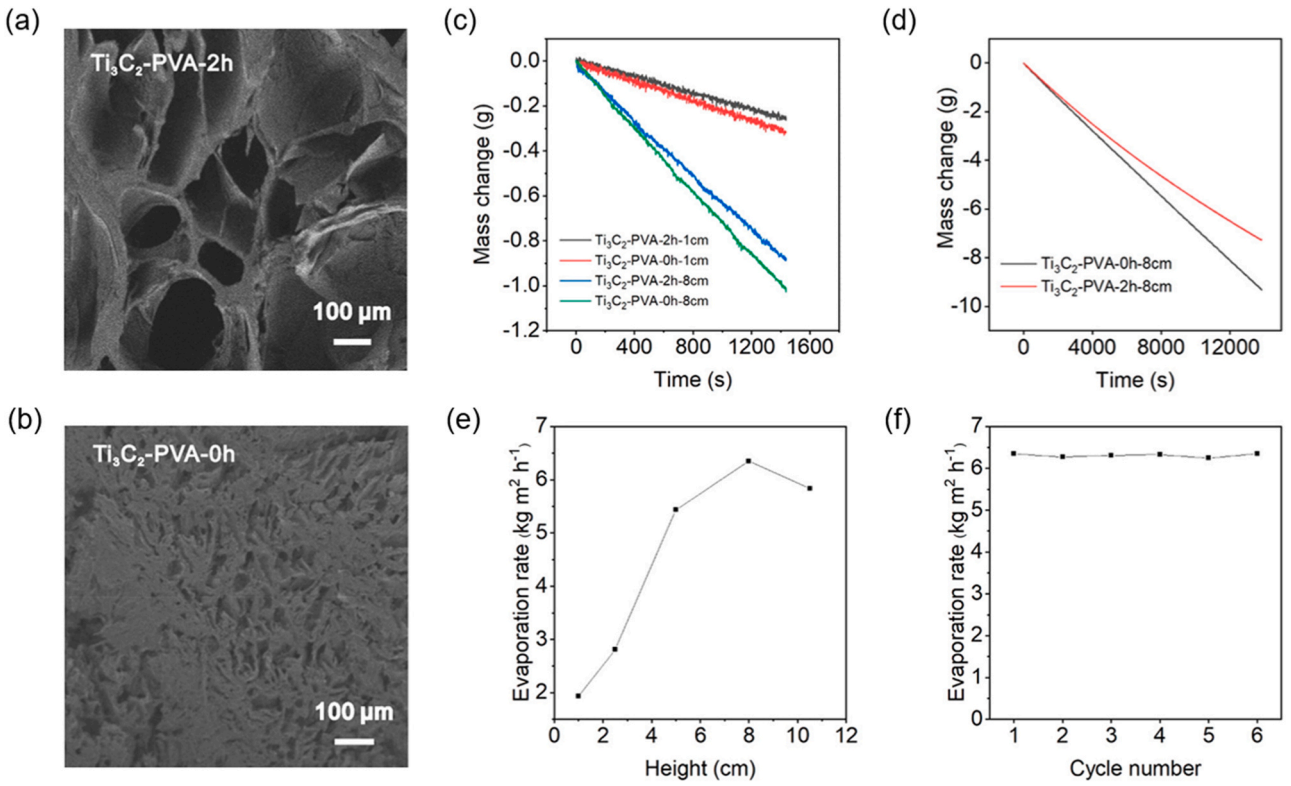

Fig. 3. The Ti_3C_2/PVA composite hydrogels as a solar evaporator for steam generation. (a, b) SEM images of incorporated Ti_3C_2 nanosheets into PVA hydrogels with different channel sizes. (c) Water mass changes of Ti_3C_2/PVA under 1 sun. The higher water evaporation rates for PVA-0 h-based hydrogels compared to PVA-2 h-based hydrogels are due to stronger capillary forces from narrowed channels. (d) Stability test for the water mass change. (e) The evaporation rate of hydrogels with increasing the height of the sample. (f) Stability test for evaporation rate conducted on different days. Reproduced with permission from Ref. [35]. Copyright ACS, 2020.

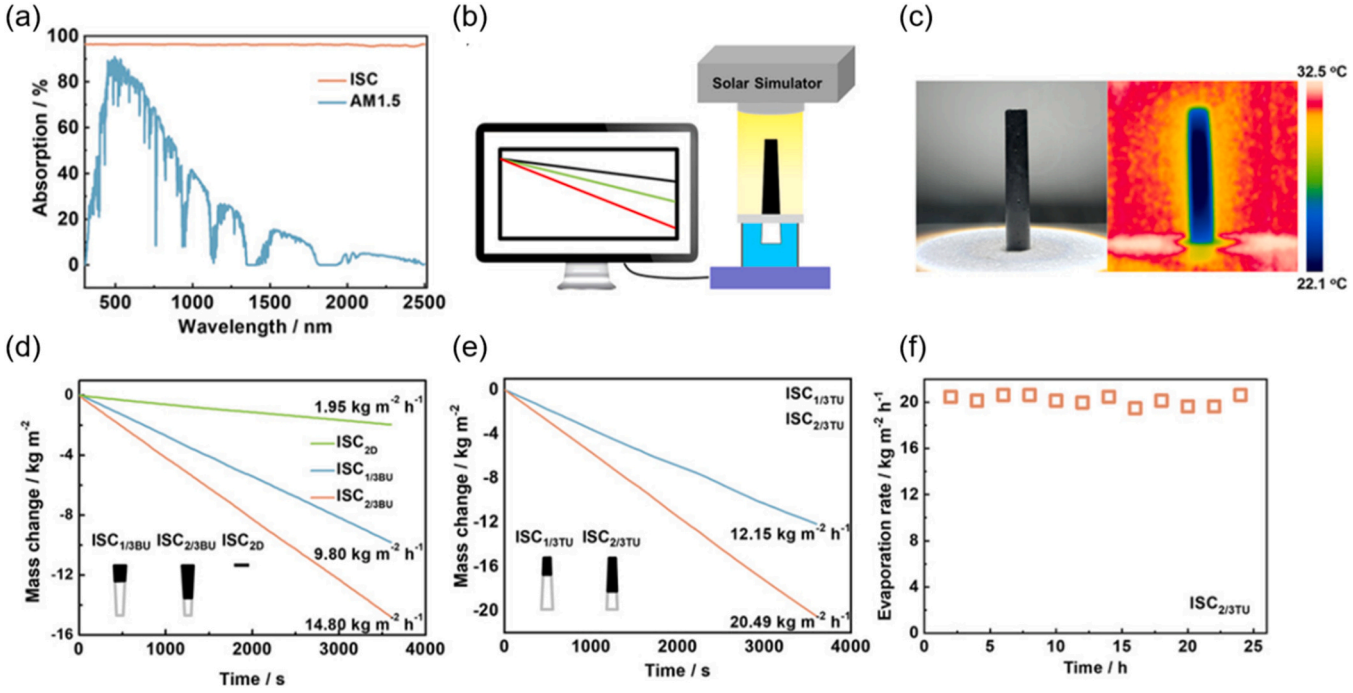

Fig. 4. (a) The image depicts the absorption spectrum of ink-stained chalk (ISC) in comparison to the solar spectrum of AM 1.5 G. (b) The experimental apparatus utilized for the solar steam generation test schematically. (c) ISC's photo and infrared radiation thermal image. (d) The figure depicts the mass change of water over time with ISC1/3BU, ISC2/3BU, and ISC2D under one sun illumination. (e) The mass change of water over time with ISC1/3TU and ISC2/3TU under one sun illumination. (g) The evaporation rates of ISC2/3TU under one solar irradiation are presented over a 24-hour period. Reproduced with permission from Ref. [36]. Copyright Wiley, 2023.

high-efficiency saltwater desalination, making it an appealing solution for distant and underdeveloped areas experiencing freshwater scarcity.

The optical characteristics and solar evaporation performance of ink-stained chalk as a photothermal material for solar desalination are shown in Fig. 4. The reflectance and absorptance spectra of ISC depicted in Fig. 4 (a) show a broad absorption range of roughly 96 % of solar energy from 300 to 2500 nm, indicating its potential as a promising photothermal material. Fig. 4 (b, d) shows the simulated sunlight illumination and solar evaporation performance of ISC utilizing an electrical balance. The inner structure of chalk aids in the effective transfer of brine to the top of ISC, while the gain of energy from the surrounding environment for the 3D solar evaporator is presented in Fig. 4 (c). ISC with top-up – 1/3 top-up and 2/3 top-up are referred to as ISC1/3TU and ISC2/3TU; ISC with bottom-up – 1/3 bottom-up and 2/3 bottom up are referred to as ISC1/3BU and ISC2/3BU. Fig. 4 (d) shows a comparison of evaporation rates for several ISC variants: ISC1/3BU and ISC2/3BU have rates of 9.80 and 14.80 kg m^{-2} h^{-1} under one solar illumination, respectively, while ISC2D only has a rate of 1.95 kg m^{-2} h^{-1}. A wider effective irradiation area (Fig. 4 (e), samples labeled as ISC1/3TU and ISC2/3TU) produces greater evaporation rates of 12.15 and 20.49 kg m^{-2} h^{-1}, respectively. Furthermore, in dark conditions, the researchers tested multiple ISC versions, finding that ISC1/3TU, ISC2/3TU, ISC1/3BU, and ISC2/3BU had evaporation efficiencies of 700 %, 1185 %, 514 %, and 790 %, respectively. These findings show that even broken or old chalk can be utilized to construct 3D solar evaporators with outstanding evaporation performance. Furthermore, Fig. 4 (f) shows ISC2/3TU's outstanding stability, with an average evaporation rate of 20.16 kg m^{-2} h^{-1} under continuous 24-hour lighting. These findings highlight the promise of ISC-based 3D solar evaporators as an efficient and dependable alternative for solar desalination in the face of freshwater scarcity.

In a recent study, solar-driven evaporation employing hydrogels and photothermal materials is presented as a feasible freshwater harvesting device. However, because of the high vaporization enthalpy of water, significant energy input is required for efficient water collecting. To solve this issue, a temperature-sensitive polyacrylamide-poly(N-isopropylacrylamide) (A-PNIPAm) gel is proposed for high water collection rates under low-energy settings, allowing quick liquid water acquisition via simple and reversible hydrophilic/hydrophobic transitions. A multifunctional hydrogel (ADS-PNIPAm) with outstanding adsorption and filtration capabilities is created by combining polydopamine with sodium alginate, allowing for the removal of contaminants and the quick creation of fresh water [37]. The ADS-PNIPAm hydrogel achieves water collection rates of 5.89 and 9.8 kg m^{-2} h^{-1} under 0.6 and 1 solar irradiation, respectively. Furthermore, ADS-PNIPAm performs admirably in sewage purification by eliminating oils, algae, and coloring contaminants. ADS-PNIPAm presents a viable method for quick freshwater generation using just solar irradiation, giving a novel approach to alleviating water source scarcity.

However, it is worth mentioning that studies that completely put the burden of improved evaporation rate on "efficient water transport" might also benefit from other factors at play, which will be discussed in the sections below.

2.2. Lowering enthalpy of water evaporation

The enthalpy of vaporization, also known as the (latent) heat of vaporization or heat of evaporation, is the amount of energy that must be added to a liquid substance to transform one mole (or unit weight) of that substance into a gas. For pure water, its latent heat of evaporation is 2444 J g^{-1}. However, the solute dilution effect should also be considered when measuring enthalpy values. Simulating sea saltwater conditions at 3.5 % NaCl solution would have different enthalpy requirements than pure water. Enthalpy values with added nonvolatile solute are always higher than pure. The added nonvolatile solute has a vapor pressure of zero, so the vapor pressure of the solution is lower than the vapor pressure of the solvent. Thus, more energy is now required to attain equivalent vapor pressure between solution and pure solvent.

Several studies blame enthalpy reduction as the sole factor for a higher evaporation rate [38–41]. One key strategy discussed to attain this target is to increase the amount of so-called "intermediate water" (IW) within the evaporator [42]. To increase this IW amount, Li et al. [43] finely tuned channel spacing in vertically aligned reduced graphene oxide (V-RGO) foams. They systematically controlled the channel spacing via dynamic compression and obtained foams with different channel diameters. The best results were obtained with foam with dynamic compression of 47.1 % reaching an evaporation rate of 3.39 kg m^{-2} h^{-1}. The author divided the water in pore channels into three distinct categories. First is free water (FW), which is surrounded by other water molecules, it has an average of four hydrogen bonds with no significant interaction with the host and is equivalent to bulk water. This type of water can be found in the center of the host structure (porous channels, polymeric network, etc.). FW has the same evaporation enthalpy as ordinary bulk water possesses owing to its strong self-interactions. The second type of water is bound to water (BW), this kind is present close to the walls of the host and exhibits strong interactions with it via hydrogen bonds. Third is IW which is neither strongly bound to walls nor inside a bulk solvent. This kind of water displays the highest evaporation rate as the bound water is strongly bound to the walls and thus requires high energy to evaporate like the bulk water, which is surrounded by other water molecules and has strong hydrogen bonding. All these kinds of water can be distinguished via Raman spectra. In this study, authors have found that the best performing sample also possesses the highest amount of intermediate water and thus exhibits the highest evaporation rates.

Another reported direction to lower the enthalpy of vaporization is confined evaporation. Confined evaporation is the evaporation in a confined space, and it happens inside the evaporator as opposed to evaporation on its outer surface. This is a direct physical approach, in which water is forced to evaporate in tiny spaces. Numerous materials such as hydrogels, carbonaceous, and various synthetic microporous structures take advantage of this effect and will be discussed in detail in their respective sections.

The first structure ever exhibiting a solar water evaporation rate larger than 3 kg m^{-2} h^{-1} was hierarchically nanostructured hydrogel (HNG) based on polyvinyl alcohol (PVA) and polypyrrole (PPy). In a typical solar vapor generation system, the water in the molecular mesh has a reduced evaporation enthalpy; the evaporated water can be rapidly restored via branched water diffusion and pumping based on micron channels and internal gaps. This report came out in 2018 and work was carried out by Zhao et al [44]. Authors managed to attain an evaporation rate of 3.2 kg m^{-2} h^{-1} with a conversion efficiency of 94 % under 1 sun irradiation. The thickness of the optimized HNG sample was ~ 400 μm while possessing micron channels which resulted in confined evaporation in these smaller-sized branches. The overall HNG structure was hydrophilic owing to the PVA-supported polymeric networks. The micron channels were essential to achieving higher evaporation rates as it allows efficient water transport via arterial pumping. Further, these micron channels have numerous connected branches, which can quickly transport water evenly throughout the membrane, and allow water distribution in the polymeric network via hierarchical water pathways. Finally, the light-absorbing polymer (PPy) converts the absorbed water penetrating the molecular meshes of the HNG into its vapor form with significantly reduced vaporization enthalpy.

Further improvement in the evaporation rate shown in Fig. 5 (a) comes from a tree-inspired design reported by Shi et al. [45]. To further improve the water evaporation rate within hydrogel structures, vertical microchannels (width of ~ 50 μm) were created via unidirectional freezing. The vertical channels can significantly improve water transport, which in the end resulted in the evaporation rate of 5.15 kg m^{-2} h^{-1} under 1 sun irradiation. In this structure, TiN nanoparticles were used as an absorber layer and agar gel provided a hydrogel structure.

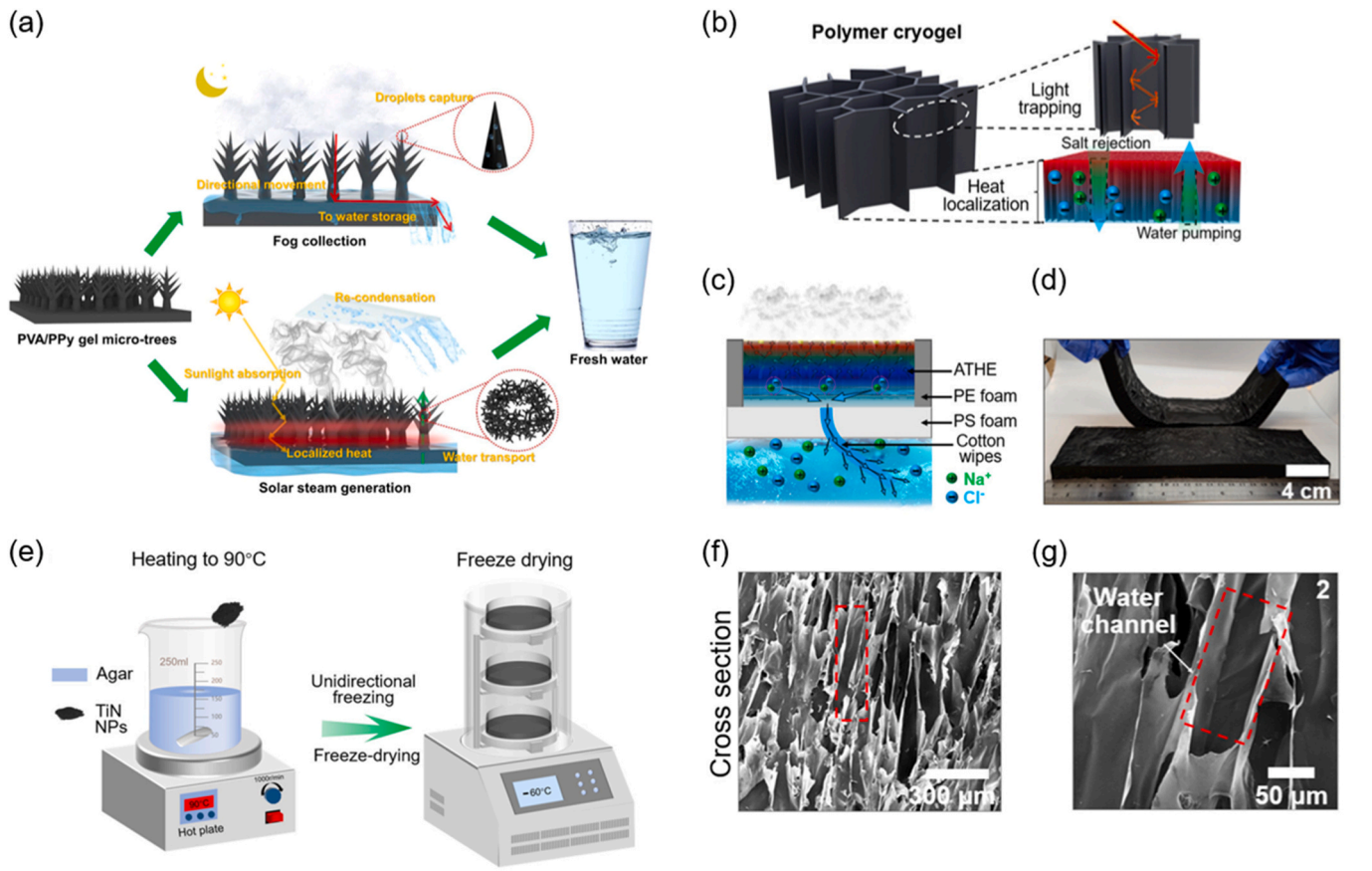

Fig. 5. (a) Design of the bifunctional PVA/PPy hydrogel membrane capable of 24 hours freshwater harvesting. Copyright Springer Nature, 2021. (b) The polymer cryogel of the agar and TiN hydrogel-based evaporator (ATHEs) effectively absorbs solar flux due to vertically aligned light trapping channels that simultaneously pump out water and remove salts. (c) The design of the experimental setup. The polystyrene (PS) insulation foam floating on the water reduces the heat dissipation from ATHEs to the bulk water. The cotton supplies water to ATHEs and dissipates salt to the bulk saltwater. ATHEs are surrounded by PE polyethylene (PE) foam to limit vapor diffusion from the sidewalls and localize heat within ATHEs. (d) The image of ATHEs showing its flexibility. Ice template-induced self-assembly and freeze-drying processes. (f, g) SEM image of a cross-section of ATHEs showing vertically aligned channels for water transport and rough surface with TiN nanoparticles embedded within the agar wall. Copyright Elsevier, 2022.
(a) Reproduced with permission from Ref. [45]. (b) Reproduced with permission from Ref. [46].

The total thickness of the final product was 1.5 cm and the system was utilized in a 2D configuration for solar water evaporation. A low thermal conductivity of 0.28 W m^{-1} K^{-1} was recorded for this hybrid hydrogel structure, which is also a contributing factor toward achieving a higher evaporation rate. It is evident from the above discussion that microchannels play a critical role in water transport and hence evaporation rate. Numerous natural materials possess microchannels, such as wood, which have been used extensively for solar water evaporation. Similar to hydrogels, natural wood is not an efficient light absorber and thus needs to be carbonized or dyed with black materials before utilization in solar water evaporation. With the tree-inspired design, Tian et al. [46] achieved a water evaporation efficiency of 3.6 kg m^{-2} h^{-1}: conical-shaped branches not only provide larger surface area, but also the confined water in hydrogel structure can evaporate at low enthalpy values (Fig. 5 (b–g)). An added advantage of this structure was the collection of fog during nighttime and its conversion into freshwater proving another utility of this unique design.

Koh et al. [47] utilized 3D printing technology and created a microporous structure made up of regenerated cellulose. The resulting 3D structure exhibits an evaporation rate of 3.01 kg m^{-2} h^{-1} under 1.0 sun illumination. Moreover, water molecules are found to be more locally ordered in 3D connected structures, leading to more hydrogen bonding in the hydrated cellulose than in bulk. According to the authors, these bonds are weaker and have longer lengths, thus resulting in enthalpy reduction. Moreover, due to the connected cellulose structure, the rehydration rate after evaporation is much faster, and under 3.0 sun irradiation an evaporation rate of 7.35 kg m^{-2} h^{-1} can be achieved.

2.2.1. Thermodynamic considerations about lowering enthalpy of water evaporation

Several studies have suggested that the lowered enthalpy of evaporation is the main factor for high evaporation rates. However, from a thermodynamic point of view, this does not seem to be valid. A lower vaporization enthalpy will not impact the overall process efficiency or thermodynamics. Previous reports claimed that IW, which has weaker hydrogen bonds, can evaporate with less energy than bulk water or FW. However, in a continuous vapor generation process, the IW needs to be replaced by new water within the photothermal material. In this step, new bulk water enters the photothermal material and some of its hydrogen bonds need to be broken to form IW. This step also requires energy. Accordingly, the vaporization enthalpy must consist of two parts: one is the phase-change energy demand for IW evaporating to vapor, and another for the formation of IW from bulk water. This additional energy requirement assures that the overall thermodynamics requirement for water evaporation remains constant. Thus, if the reported measurements of solar water evaporation are correct, there must be another reason for the high efficiency besides the weak bonding of the IW molecules.

One possible reason for enhanced evaporation rate within narrow/confined regions is that these structures possess a larger surface area.

This is because more water molecules are exposed to air, and they can acquire more heat energy from the surroundings and escape into the gas phase. A second possible reason for the enhanced evaporation rate might be that water separates into sheets with different diffusion coefficients when confined in nanochannels, such as carbon nanotubes (CNTs), with diameters between 3.0 and 4.5 nm [48]. The central sheet of water has a very high diffusion coefficient, up to four times that of bulk water, which could enhance the evaporation rate. However, the CNTs structure is hydrophobic and water morphology might be different within hydrophilic nanoconfined channels.

2.3. Thermal management

Thermal management is an essential component of solar-to-vapor efficiency during desalination [11,49]. To achieve high efficiency in water evaporation, it is crucial to reduce the amount of heat that escapes from the system. Heat can be lost to the surroundings in three ways: by conduction, which is the transfer of heat through direct contact; by convection, which is the transfer of heat through fluid motion; and by radiation, which is the emission of electromagnetic waves.

A widely adopted method to reduce heat loss is to place a layer of thermal insulator (such as polystyrene) below the absorber layer (as shown in Fig. 6). The purpose of this layer is to prevent the heat from reaching the bulk water and thus keep it within the absorber layer. This way, the heat can be concentrated and used for water evaporation. However, some recent studies have proposed a different approach, which is to use a layer of thermal conductor below the absorber layer. We will discuss these studies in more detail in the section on environmental energy harvesting.

A possible way to minimize these heat losses is to use a material with low thermal conductivity for the evaporator. Thermal conductivity measures how well a material can conduct heat. A low thermal conductivity means that heat will not easily flow through the material, but rather stays within it. This way, the evaporator can retain more heat while absorbing light, and reach a higher temperature that enhances water evaporation. For instance, Wang et al. [51] prepared polydimethylsiloxane (PDMS)-based foam with embedded Cu_7S_4-MoS_2-Au nanoparticles (CMA) – CMA/PDMS. A salient feature of this synthetic absorber was its low thermal conductivity of 0.0746 W m^{-1} K^{-1}. This lower thermal conductivity avoids heat dissipation to water and heat was mainly concentrated on the porous network where evaporation takes place, resulting in an enhanced evaporation rate. The fabrication process of CMA/porous photothermal nanostructure (PPN) is shown in Fig. 7 (a). The facile gas foaming process was adopted for foam fabrication with the aid of gas bubbles produced from ammonium bicarbonate during the polymerization process. This resulted in the fabrication of a 3D interconnected PDMS network with embedded absorber CMA nanoparticles. The sponge-like porous PDMS with and without CMA is shown in Fig. 7 (b). Further, the foam was treated with acrylic acid to improve hydrophilicity. The diameter of the internal gap of the cross-section of CMA/PPN was about 100 μm (Fig. 7 (c)). Due to the presence of Cu_7S_4-MoS_2-Au nanoparticles, the foam exhibits absorption in UV–vis–NIR regions as shown in Fig. 7 (d). Finally, the foam was tested for solar water evaporation under one sun illumination and exhibited an evaporation rate of 3.824 kg m^{-2} h^{-1} and 96.6 % photothermal conversion efficiency.

Similarly, Li et al. [52] synthesized porous foam possessing low thermal conductivity from expanded polymethyl methacrylate (PMMA) embedded with a typical D-A-D molecule (TPA-BTDH) (Fig. 8 (a)). TPA-BTDH is a photosensitizer that possesses good photothermal conversion along with the production of reactive oxygen species when excited via external light. Generated reactive oxygen species can endow the evaporator with anti-biofouling properties. SEM micrographs of cross-sections are presented in Fig. 8 (b). The proposed material shows relatively good absorption properties in the range of 550–1000 nm but low absorption beyond 1000 nm (Fig. 8 (c)). From Fig. 8 (d, c) upon 1 sun illumination from the top of the evaporator, the top surface temperature was increased to 46.5 °C but the side temperature was only 28.9 °C and the corresponding evaporation rate was 2.4 kg m^{-2} h^{-1}. However, when the evaporator was illuminated from the side with an incident angle of 60°, the corresponding temperatures were 44.5 and 39.5 °C, respectively. In this case, as the entire evaporator surface was heated, the evaporation rate increased to 3.6 kg m^{-2} h^{-1}. The side area under illumination absorbs the light and collects additional energy, allowing a significant increase in the evaporation rate of almost 50 %. The authors also tested the thermal conductivity values of the foam and found that the thermal conductivity increased from 0.0579 to 0.0605, 0.0651, and 0.0666 W m^{-1} K^{-1} as the temperature increased from 30 to

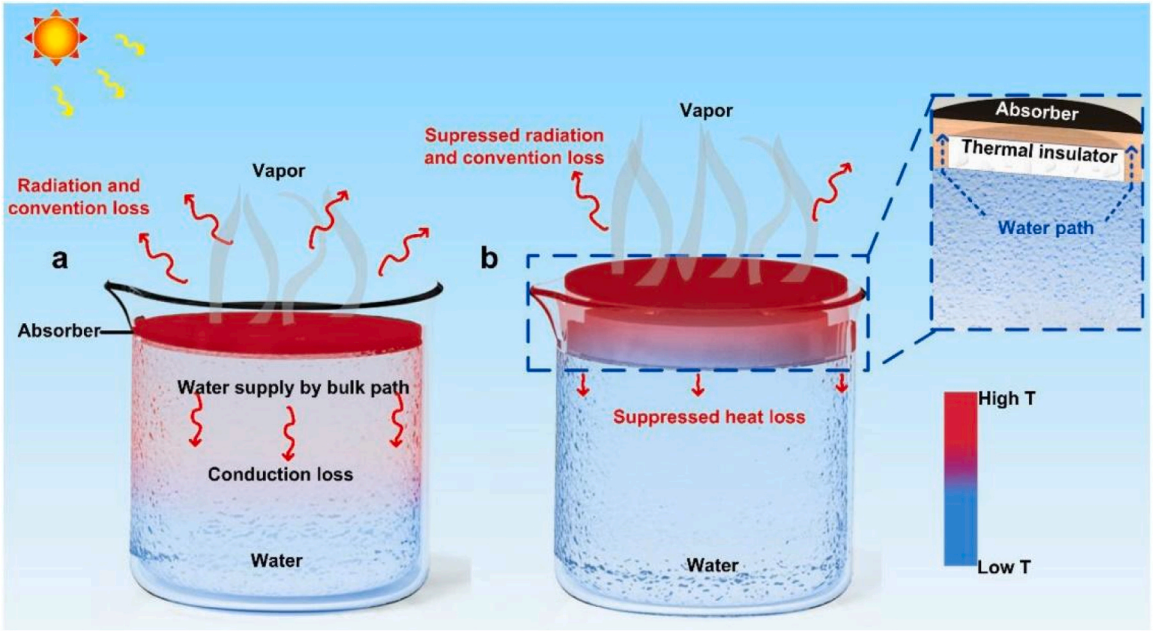

Fig. 6. (a) Illustration of traditional solar water evaporation with direct water contact. (b) Illustration of solar water evaporation device with inhibited heat loss. Reproduced with permission from Ref. [50]. Copyright Elsevier, 2021.

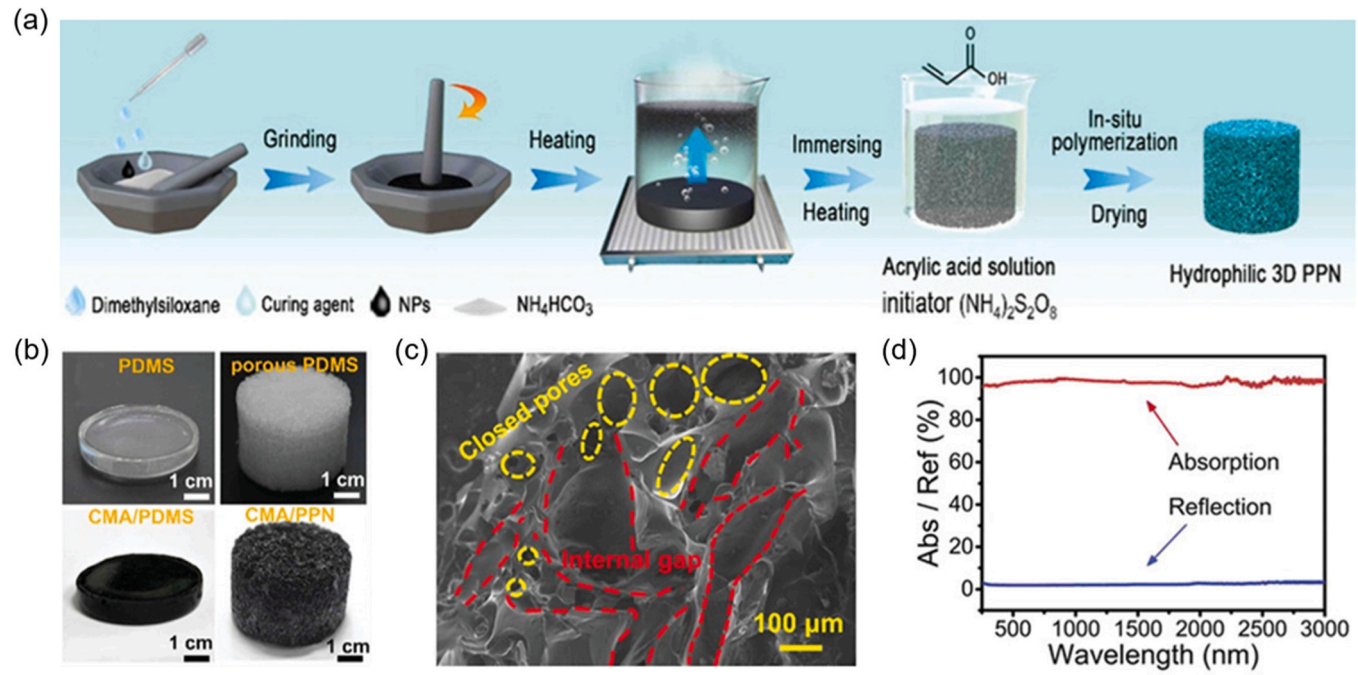

Fig. 7. The methodology of synthesis and characterization of CMA/PPN. (a) The scheme of the formation process of CMA/PPN by an in-situ gas-foaming together with polymerization surface coating strategy. (b) The images of CMA/PPN with and without CMA doping. (c) The SEM image of the cross-section of CMA/PPN. (d) Absorption and reflection spectra of CMA/PPN. Reproduced with permission from Ref. [51]. Copyright Wiley, 2020.

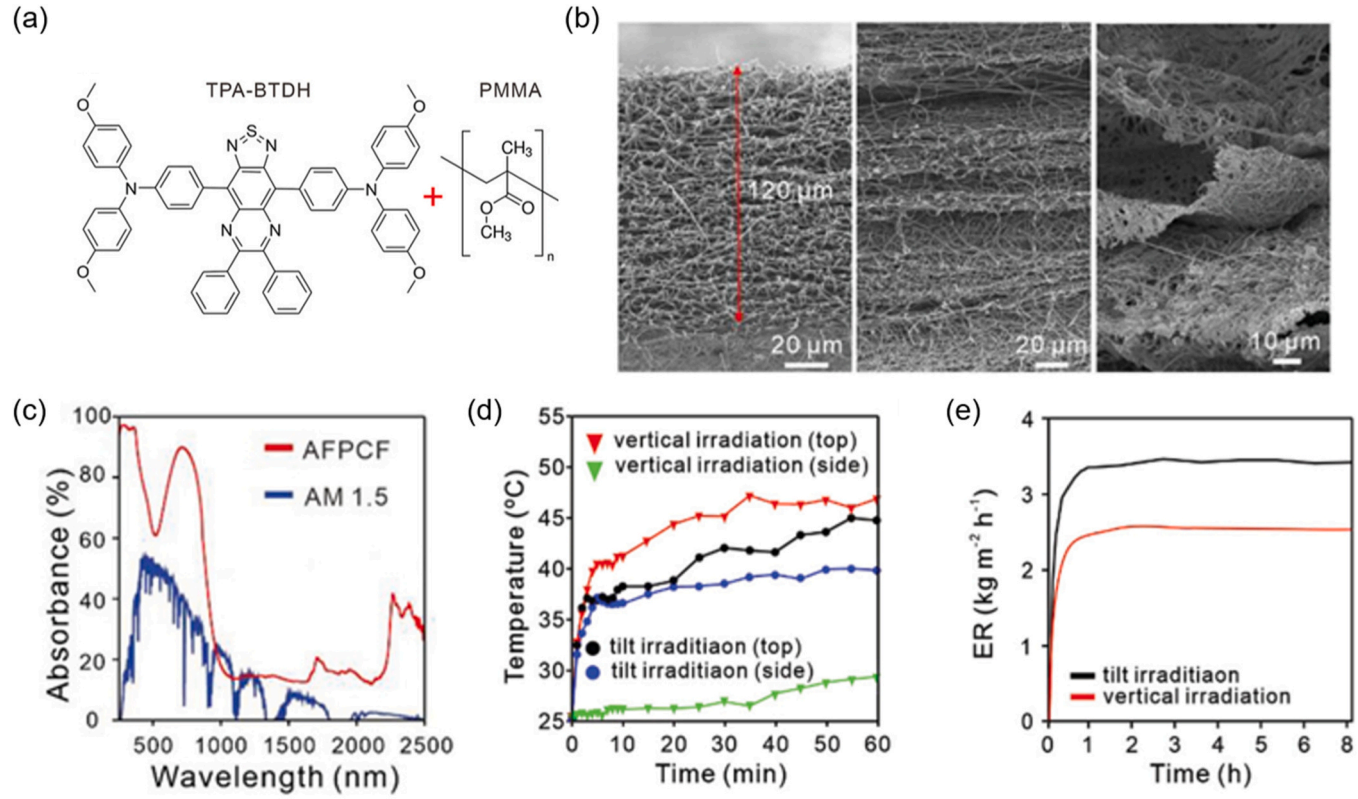

Fig. 8. (a) The structure of TPA-BTDH. (b) SEM micrographs of the cross-sections of TPA-BTDH/PMMA nanofibrous mat before and after treatment in the $NaHB_4$ solution (1 M) for 10 and 60 min. (c) The absorption spectra of the all-fiber porous cylinder-like foam (AFPCF) are in the range of 250 – 2500 nm and solar spectral irradiance is set at 1 sun. (d) Photothermal behavior of the surface and side of AFPCF upon the vertical and tilted irradiation of 1 sun irradiation for 60 min. (e) The evaporation rate of AFPCF under vertical and tilted irradiation at 1 sun. Reproduced with permission from Ref. [52]. Copyright Wiley, 2021.

40, 50, and 60 °C, demonstrating a low thermal conductivity.

2.4. Environmental energy harvesting

Although it is generally considered that a thermal insulator underneath a 2D absorber is necessary to minimize the heat loss to water and the environment, Wang et al. [53] proposed that it is not the case for a 3D absorber. They argue that, since a 3D absorber can also harvest energy from the surrounding environment, air, and bulk water, the use of a thermal insulator will hinder energy extraction from water. To prove their point, they replaced the thermal insulator (expanded polyethylene foam – EPE foam) with thermally conductive steel and aluminum underneath the absorber layer, as depicted in Fig. 9 (a). The thermal conductivity of steel is lower than that of aluminum, hence it can extract less stored heat from bulk water (Fig. 9 (b)). It is worth noting that bulk water possesses a much higher volumetric heat capacity ($4.2\bullet10^6$ J m^{-3} K^{-1}) compared to air ($1.2\bullet10^3$ J m^{-3} K^{-1}). Thus, highly thermally conductive evaporator support can extract a greater amount of heat from the water and increase the evaporation rates. As a result, the evaporator with aluminum support attains an evaporation rate of 5.40 kg m^{-2} h^{-1} compared to merely 3.81 kg m^{-2} h^{-1} for EPE foam (an insulator) support under one sun (Fig. 9 (c)). Maximum reduction in the temperature of bulk water was also observed for aluminum during evaporation experiments as depicted in Fig. 9 (d). Evaporation stability experiments in an outdoor setting improved the evaporation rate for all absorbers since the flow of air over the evaporation surface is also a significant contributor to higher evaporation rates (Fig. 9 (e)). It is worth noting that the maximum surface temperature of the absorber surface attained in this study was less than 30 °C suggesting that the rate can be further improved via the utilization of other absorber materials capable of attaining higher surface temperature.

This concept of energy harvesting from the environment has been demonstrated in other studies as well. For instance, Gao et al. [54] attained an evaporation rate of 7.6 kg m^{-2} h^{-1} under one sun. They have utilized a 3D hollow and compressible photothermal evaporator (HCE) composed of a spring frame, over which a photothermal aerogel sheet was mounted and was prepared by cotton sheet, reduced graphene oxide (rGO), and sodium alginate (SA). This design managed to maintain its surface temperature lower than the environment during sun illumination and thus enabling energy harvesting from the environment. Further, it possesses the unique advantage of zero energy loss to the environment. The photothermal layer is composed of cotton cloth coated with graphene oxide aerogel with light absorption of 97.0 % across the UV–vis–NIR regions. The evaporation rates were 4.7, 6.1, and 7.6 kg m^{-2} h^{-1} for evaporator heights of 4.5, 9.0, and 14.0 cm, respectively. It suggests that the height of the evaporator has a significant effect as it would increase the evaporation surface area while the projected area of illumination stays constant. It is interesting however that the evaporation rate of 5.0 kg m^{-2} h^{-1} was observed for the 14.0 cm evaporator under dark conditions, thus the evaporator exhibits a net evaporation rate of only 2.6 kg m^{-2} h^{-1}. Such a high evaporation rate under dark conditions suggests that the evaporator is already harvesting sufficient energy from the environment. However, the authors did not clarify in detail the choice of the area for the calculation of the evaporation rate. This makes the result slightly questionable: if the projected area was considered, then the evaporation rate would have been much lower by considering the entire area of the evaporator. In our opinion, it is important to mention these values and the precise method for the calculation of the evaporation rate, as it would allow a fair comparison between 2D and 3D evaporators. Further, along with the text, the authors mention that the overall energy conversion efficiency of the evaporator was 178.6 %. This is beyond theoretical limits, however, the authors calculated energy contributions from the environment during evaporation and it turns out that the evaporator had gained additional

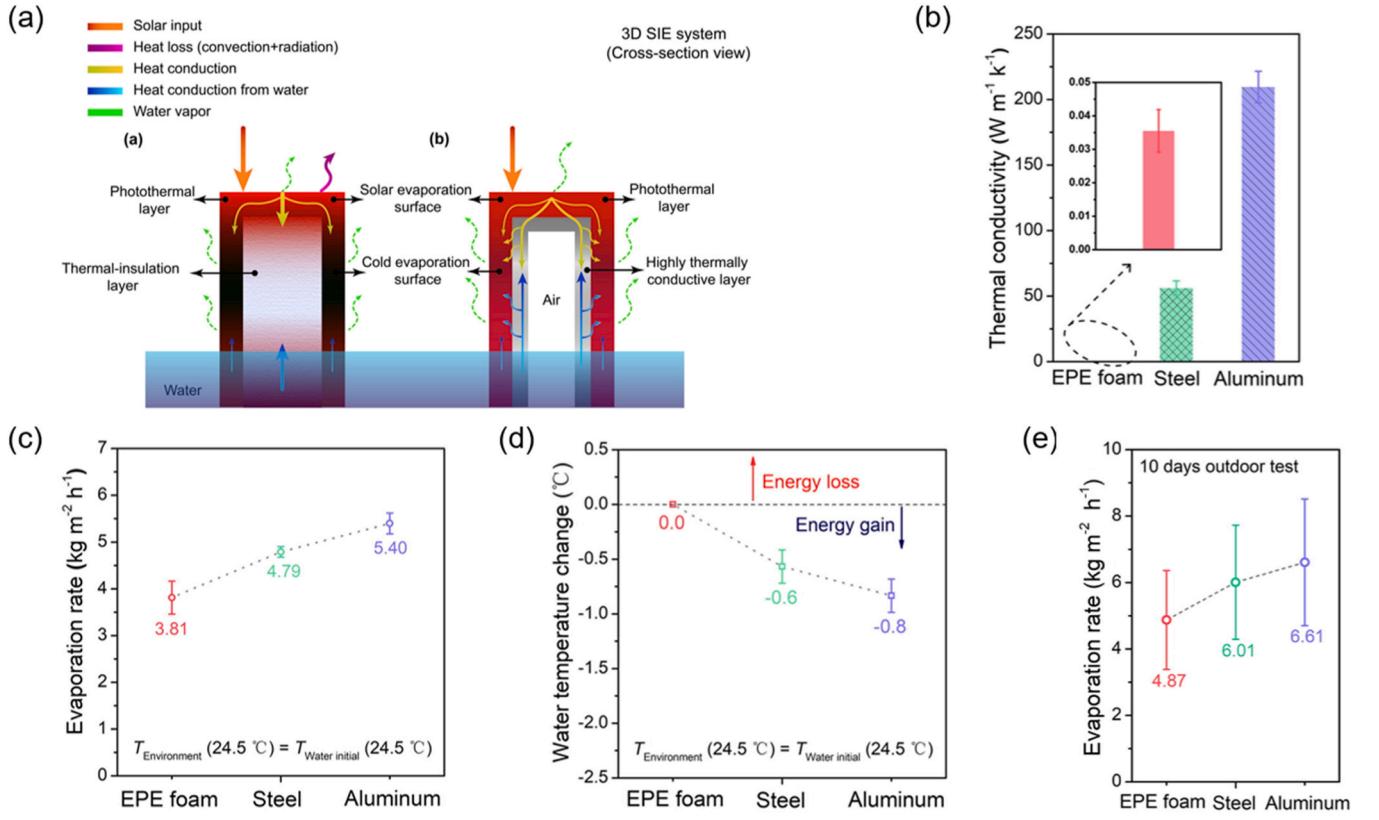

Fig. 9. (a) Energy flow in a 3D evaporator with thermal insulation and inclusion of thermal isolation support. (b) Thermal conductivity, (c) evaporation rate, (d) water temperature change, and (e) evaporation rate during the long-term outdoor test of the EPE foam, steel, and aluminum. Reproduced with permission from Ref. [53]. Copyright Elsevier, 2021.

energy from surrounding air, as its surface temperature was lower than the surrounding temperature. It is worth mentioning here that energy obtained from the sun is 1 kW m^{-2} h^{-1} at AM 1.5 G standard.

Similarly, Wu et al. [49] utilized a heatsink strategy to extract energy from the environment. The absorber was made up of bamboo paper coated with porous black carbon material (Fig. 10 (a)). Their design consists of a hollow cylinder where the sides are covered with 2D fabric fins. The temperature of fins is essentially lower than the temperature of the environment due to continuous evaporation, this allows heat to be absorbed from the surrounding environment as well as from underneath water (Fig. 10 (b)). Further, the radiation and convection loss from the top evaporation surface during solar steam generation was fully eliminated as all excess heat was transferred immediately to the hanging fins. Following this heatsink approach, the authors obtained an evaporation rate of 4.10 kg m^{-2} h^{-1} under 1 sun illumination (Fig. 10 (c)). Owing to the unconventional design, authors claimed that their optimized evaporator harvested 4.26 W extra energy from the environment compared to 2.4 W obtained from light illumination under one sun. This extra energy harvesting resulted in an energy conversion efficiency of 282 % which was over 170 % of the energy of the incident light.

Dang et al [26] utilized multichannel photothermal rod (MCPR) made from modified rattan wood for solar-driven interfacial evaporation. MCPR surface is further modified with photocatalytic H-TiO_2 needles, which provide self-cleaning and antifouling properties. This prevents the accumulation of micropollutants and organic pollutants on the surface of the MCPR, maintaining its efficiency and performance. A 10-cm-high MCPR can produce 18.8 kg m^{-2} h^{-1} under 1 sun. When the light is incident at 30°, the evaporation rate can be increased to 31.3 kg m^{-2} h^{-1}. In an outdoor environment, the evaporation rate can even be raised to 126.5 kg m^{-2} h^{-1} by using a magnified evaporation system constructed of a 35-cm-high MCPR array. The high evaporation rate of the MCPR evaporator can be attributed to several factors. Firstly, the design of the MCPR array optimizes material efficiency and system structure, leading to improved energy efficiency. The 3D structure of the MCPR array increases the area of the MCPR-air interface, enhancing air turbulence and facilitating steam escape. This results in a higher steam production rate and condensate collection rate. Secondly, the MCPR array can capture omnidirectional solar radiation, allowing it to maintain a consistent evaporation rate even with changes in incident angles and sunlight intensity. This ensures stable and reliable performance of the evaporator system. Furthermore, the height of the MCPR array plays a role in enhancing evaporation. Increasing the height of the MCPR array increases the area of the MCPR-air interface, reinforcing air turbulence and accelerating steam escape, resulting in higher steam production rate.

Overall, the combination of optimized material design, enhanced energy efficiency, omnidirectional solar radiation capture, self-cleaning properties, and increased MCPR height contribute to the high evaporation rate of the MCPR evaporator.

The high evaporation rate reported in this study under outdoor conditions has also been observed in other studies. For instance, Wen et al. [55] observed that their Janus hydrogen-based evaporator showed an evaporation rate of 24.5 kg m^{-2} h^{-1} under outdoor conditions. However, this evaporator exhibited an evaporation rate of only 3.35 kg m^{-2} h^{-1} while testing indoors. Outdoor wind and reduced humidity levels are likely to improve the evaporation rate significantly.

The need for efficient and sustainable purification methods, the risk of evaporator blockages and fouling due to undissolved salt, the requirement for effective antibacterial properties to maintain water quality, and the lack of a reliable predictive formula for evaporation rates under varying environmental conditions are all challenges in seawater desalination. In response to these issues, Jin et al [56] provides a hollow cylinder-shaped nonwovens/modified ceramic solar evaporator that overcomes them. Under increased convective airflow and low ambient relative humidity, the 3D hollow cylinder-shaped structure offers a greater evaporation area and effective vapor diffusion, resulting in an outstanding evaporation rate of 28.9 kg m^{-2} h^{-1}. To effectively remove blockages brought on by undissolved salt, acid treatment should

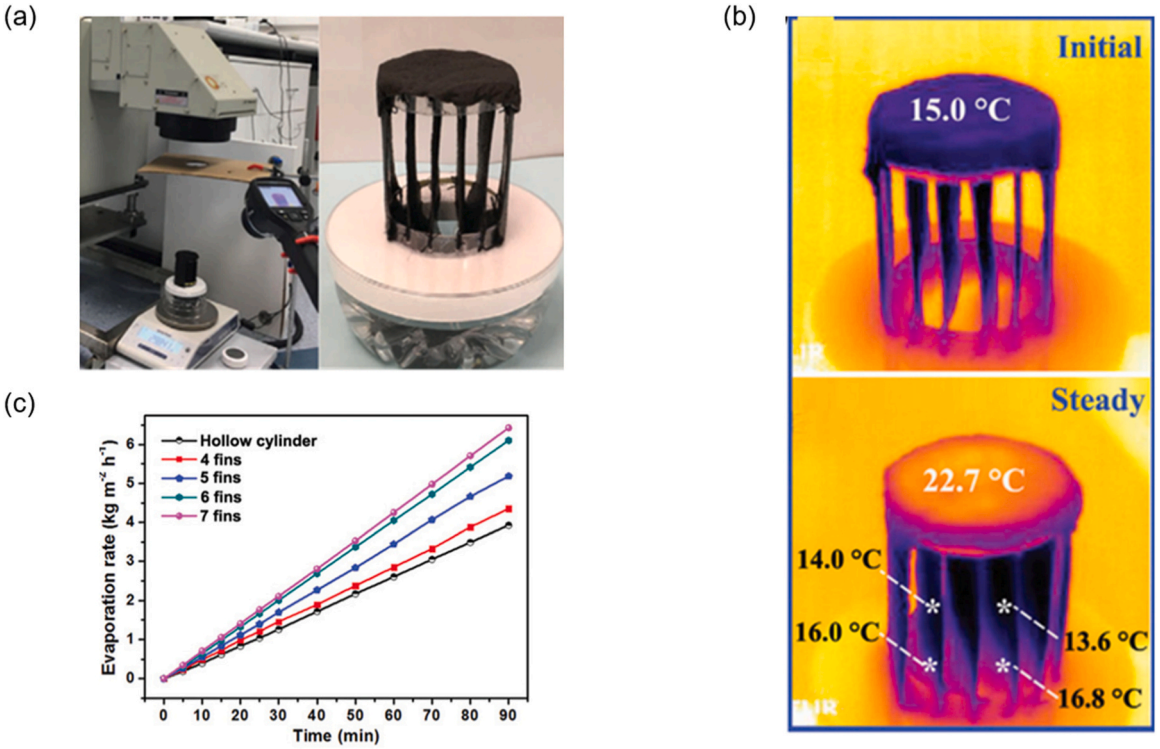

Fig. 10. (a) Digital photographs of the test setup for solar steam generation. (b) Initial (upper) and steady (lower) IR images of the 6-fin HSE under 1.0 sun irradiation after 30 min. (c) Evaporation rate over cylinder evaporator and HSEs with different numbers of the fin. Reproduced with permission from Ref. [49]. Copyright Wiley, 2021.

be applied in the evaporator. Additionally, the evaporator demonstrates a remarkable 91.7 % antibacterial ratio thanks to the modification of the ceramic with photocatalyst activity (Fe_2O_3/Ag/TiO_2), maintaining water quality throughout the purifying process. This study also develops a predictive empirical model for evaporation rates, enabling customized design and evaporator optimization under diverse climatic conditions. Making important advancements in the field of solar-driven water purification, this cutting-edge solar evaporator offers a viable solution for effective and sustainable saltwater desalination and zero-liquid discharge applications.

On the other hand, Peng et al. [57] introduced a considerable improvement in evaporation rates by using a 3D evaporator with multi-vertical sheets that were created through 3D printing and assembly. The unique design improved convection flow, resulting in an ultra-high evaporation rate of 28.4 kg m^{-2} h^{-1}, which outperformed prior results. The relationship between convection flow and evaporation rate was found to be linear, and the mechanism underlying the enhanced performance was discovered. The 3D evaporator displayed outstanding cumulative mass change and ion concentration standards for desalinated seawater, making it a suitable contender for practical water treatment applications. This study provides important insights into improving the efficiency of solar vapor generation, which aids in the development of environmentally friendly technologies.

2.5. Wind energy

Using wind energy to enhance solar evaporation is a promising method to achieve a high evaporation rate. Wind energy is a renewable resource that is widely available on the earth's surface. By blowing wind over a solar evaporator, the evaporation rate can be greatly increased because the wind removes the vapor that is produced by the sun's heat. Wind speed affects the evaporation rate of water by moving the saturated air away from the water surface and replacing it with drier air. This creates a gradient of vapor pressure between the air and the water, which drives the diffusion of water molecules into the air.

Consequently, Li et al. [58] were able to attain an evaporation rate larger than 10.9 kg m^{-2} h^{-1} with the help of 3D interconnected porous carbon foam at a wind speed of 6 m s^{-1}. The evaporation rate under zero wind speed was merely 2.5 kg m^{-2} h^{-1}. Such high evaporation rates were the result of convective airflow (provided with a fan) passing through a 3D porous carbon structure as depicted in Fig. 11 (a). Authors argue that a connected porous structure is imperative for a higher evaporation rate as it would allow fast removal of generated vapors from the surface of the absorber. This would not be the case with a solar absorber with a closed pore structure. The design of such a porous connected carbon structure was achieved by an inexpensive method utilizing commercially available sucrose and sulphuric acid. It is worth noting (Fig. 11 (b, c)) that this structure is also able to achieve a high evaporation rate (wind flow 6 m s^{-1}) larger than 10 kg m^{-2} h^{-1} without the use of sunlight, proving that wind energy is a major contributor in driving the evaporation rate. This proves the utility of connected porous structures as blown wind through its tunnels can take away a significant amount of generated vapor.

To prove the utility of connected porous structure, the authors fabricated and compared 3D aerogels with vertically aligned and interconnected channels, presented in Fig. 12. From Fig. 12 (e, f), the vertically aligned porous structure does not allow the passage of particles with diameter below 2.5 μm (PM 2.5) and evaporation rate of that structure at different wind flow is significantly lower than those of the interconnected porous one. The experiment proved that using configuration of interconnected channels allows convective flow to pass through the whole system and improve the performance.

Along similar lines, Choi et al. [59] utilized carbonized luffa sponges (CLS). The obtained rate was 14.5 kg m^{-2} h^{-1} at the wind speed of 2 m s^{-1} and one sun irradiation. The evaporation rate without wind was only 3.7 kg m^{-2} h^{-1} suggesting significant contributions from the wind. This carbonized luffa sponge is highly porous and pore sizes are in the range of 100 micrometers. As evidenced in Fig. 13, by increasing the wind speed, the temperature of CLS decreased significantly. The temperature of the air was recorded by the authors before and after it went through

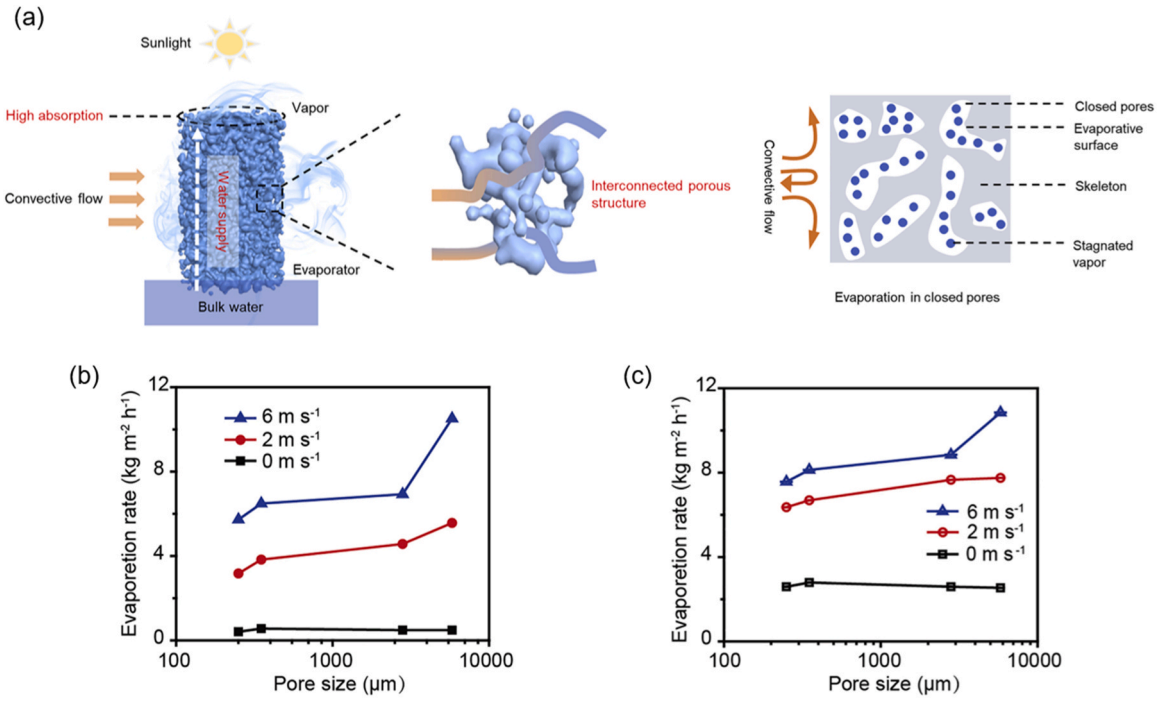

Fig. 11. (a) The design concept of the 3D interconnected porous evaporator providing a high evaporation rate. Illustration of the interconnected porous structure assures effective diffusion with a natural convective flow. Illustration of evaporation in traditional evaporator within closed pores resulting in ineffective diffusion and low evaporation. (b, c) The evaporation rates of the 3D for different pore sizes with different convection flows (b) without sunlight illumination and (c) under 1 sun. Reproduced with permission from Ref. [58]. Copyright Elsevier, 2020.

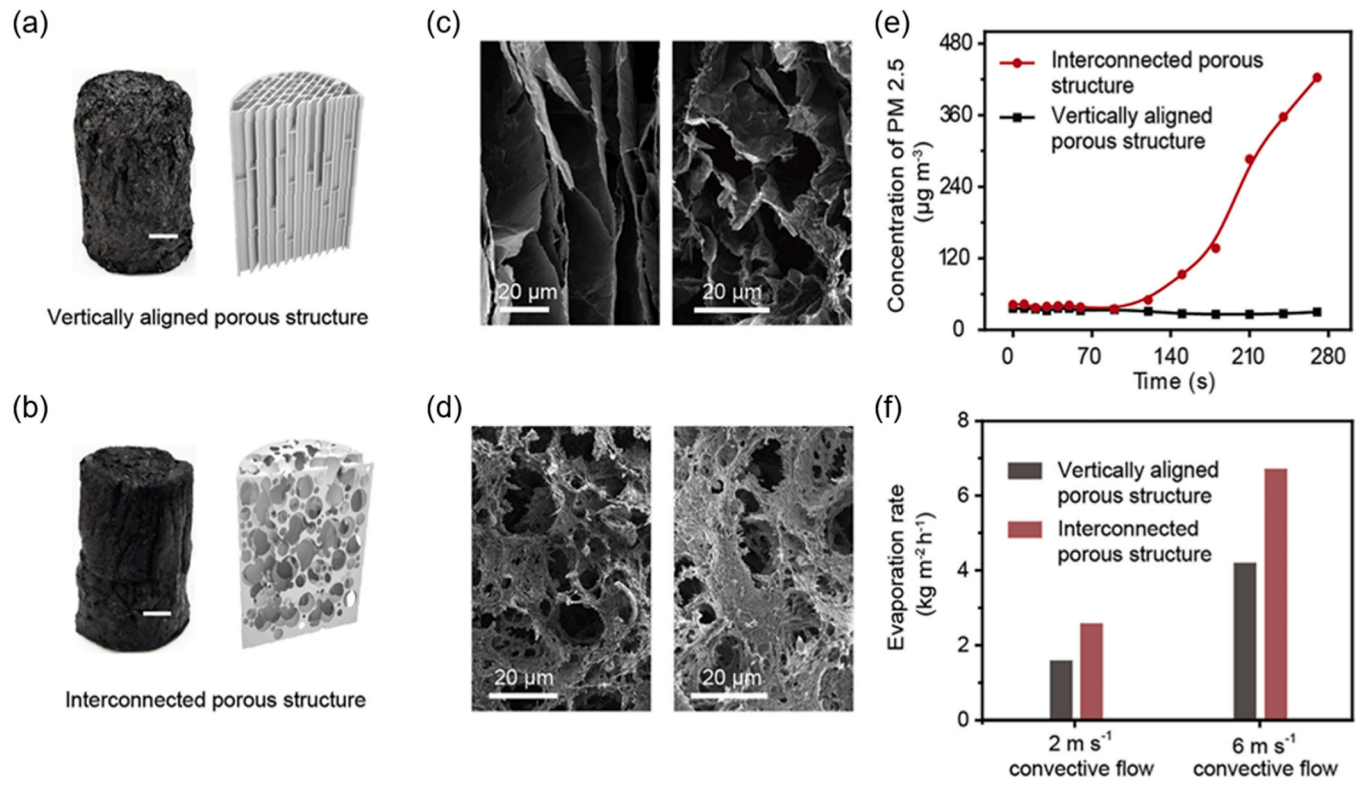

Fig. 12. 3D aerogels with (a) vertically aligned porous structure and (b) interconnected porous structure. Optical images (left panel) and schematics (right panel). SEM micrographs of (c) vertically aligned porous structure and (d) interconnected porous structure. Cross-section view (left panel) and bird's view (right panel). (e) Permeability of PM 2.5 through two different morphologies. (f) Evaporation rates of the 3D aerogel with two different morphologies assisted with convective flows of 2 and 6 m s^{-1}. Reproduced with permission from Ref. [58]. Copyright Elsevier, 2020.

the sponge structure. They observed that the air became cooler by 3.6 °C after passing through the sponge, which indicated that some energy was transferred from the air to the water. The amount of heat that the carbonized luffa sponge absorbed while evaporating water was estimated to be 9.7 kW m^{-2} when exposed to sunlight and wind at 2 m s^{-1}. This value was much higher than the amount of solar energy that reached the same area (1 kW m^{-2}). The carbonized luffa sponge had a high light absorption of 97 % in the wavelength range of 300–2000 nm.

Some studies have shown that the absorber's temperature can drop below the ambient temperature when there is wind and evaporation, which means that the device can harvest energy from the environment. However, this phenomenon was not observed in a study by Yin et al. [60], who used a 2D evaporator to achieve a high evaporation rate of 7.6 kg m^{-2} h^{-1} under 1 sun irradiation and a wind speed of 3 m s^{-1}. The evaporator was made of nanotextured copper sponges, which had a porous structure that allowed the vapor to escape quickly in the presence of wind (Fig. 14 (a–e)). The wind speed also affected the evaporator's surface temperature, but it did not go below the ambient temperature.

Apart from these designs, other novel approaches are worth mentioning. For instance, Liu et al. [61] compared the evaporation rate of 2D surfaces vs 3D ones by deploying super-hydrophilic solar absorber based on carbon nanotubes-coated air-laid paper as depicted in Fig. 14 (f, g). Authors have obtained an evaporation rate of 5.5 kg m^{-2} h^{-1} for a wavy 3D structure compared to 3.11 kg m^{-2} h^{-1} for 2D design at an airflow of 5 m s^{-1}. This high rate of a 3D surface is due to the validity of dual evaporative surfaces and the reduction in solar reflection loss due to the wavy design.

Liu et al. [62] fabricated a 3D pyramid-shaped electrospun nanofiber solar water evaporator by using a homogenized electrospun PAN/CNT nanofiber membrane. This innovative design features high light absorptance at 98.3 % and a low enthalpy, significantly boosting the evaporation rate. The hierarchical structure of the evaporator enhances vapor generation, achieving an evaporation rate of 2.62 kg m^{-2} h^{-1} under one sun irradiation without convective flow, which increases to 8.31 kg m^{-2} h^{-1} with a convective flow of 4 m s^{-1}. Additionally, the evaporator maintains high evaporation rates and demonstrates excellent self-cleaning properties even in high-concentration brine, making it highly effective in various conditions.

Li et al. [63] designed a 3D hybrid aerogel (rGP) via a hydrothermal process using reduced graphene oxide and polyvinyl alcohol phosphate ester. Through testing various heights of the material, the 3 cm tall evaporator demonstrated the highest performance, reaching an impressive evaporation rate of 4.89 kg m^{-2} h^{-1} under one sun illumination and an enhanced evaporation rate of 16.22 kg m^{-2} h^{-1} when subjected to a convective flow of 2.5 m s^{-1} over 7 days. The 3D rGP structure promoted solar vapor generation through water activation and environmental energy enhancement effects. Additionally, high-throughput evaporative desalination was achieved by coupling the rGP with natural convection, showcasing its potential for efficient solar desalination applications.

In a pioneering study, Wang et al. [64] developed an ultrablack Cu–$Cu(OH)_2$-MOF foam with intricate hierarchical structures, achieving exceptional light absorption (99.01 %) and capillary force enhancement. This led to a biface evaporator with sub-ambient surface temperature, yielding a high evaporation rate of 3.27 kg m^{-2} h^{-1}, surpassing traditional methods. Notably, when cooled in seawater with airflow 5.8 m s^{-1}, it achieved a superior evaporation rate of 11.58 kg m^{-2} h^{-1} and efficiency of 160.07 %, marking a significant advancement in sustainable water harvesting.

Tian et al. [65] introduced a novel 3D cylinder evaporator, SMNG, integrating catalytic Ag-MnO_2 nanostructures with N-doped graphene aerogel, resulting in exceptional performance. Under one sun irradiation, SMNG exhibits an impressive evaporation rate of 6.46 kg m^{-2} h^{-1}.

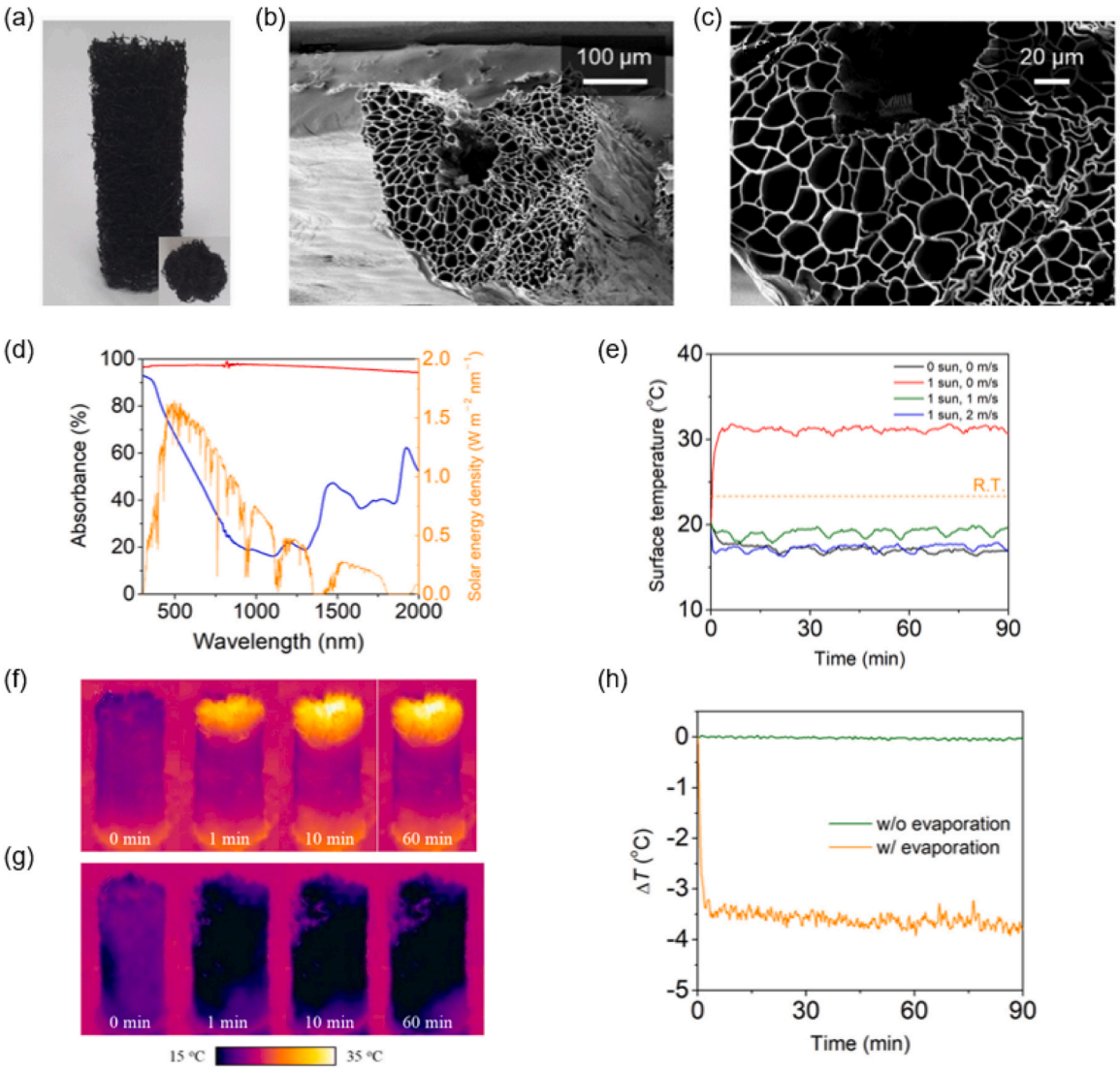

Fig. 13. (a) The image of CLS with inset of cross-sectional image. (b) SEM image of CLS fiber in cross-section. (c) Magnified image. (d) The absorption spectra of the dried luffa sponge (blue) and CLS (red). (e) Photothermal behavior of the top surface of CLS under various conditions. (f, g) Time-lapse IR images of the CLS (f) under 1 sun and 0 m s^{-1} wind, (g) under 1 sun and 2 m s^{-1} wind. (h) The differences between the inlet and outlet temperatures of the CLS with and without water evaporation. Reproduced with permission from Ref. [59]. Copyright Springer Nature, 2021.

In outdoor experiments, it achieves a remarkable seawater evaporation rate of 8.57 kg m^{-2} h^{-1}, highlighting its practical viability. The high evaporation rate of SMNG can be attributed to factors such as light intensity and wind speed, particularly the acceleration of vapor diffusion induced by wind. This superior performance can be also explained by unique 3D columnar architecture, large surface area facilitating efficient water vapor transport, and the synergistic effects of Ag-MnO_2 nanostructures, enhancing both evaporation and purification capabilities.

In a recent study, Li et al. [66] created all-in-one interfacial steam generators (SGs) employing monolithic, self-standing, and robust aerogel matrices made using composite photothermal inks and ink-extrusion 3D printing. These cutting-edge SGs go beyond various performance obstacles that traditional 3D structures encounter. Rapid prototyping was used to create multiscale hierarchical structures that increase actual evaporation areas, improve evaporation efficiency, and efficiently use environmental energy input. The SGs were among the best-performing solar-powered interfacial SGs, with high water evaporation rates of 3.74 kg m^{-2} h^{-1} in calm air and a remarkable 25.3 kg m^{-2} h^{-1} under a gentle breeze of 2 m s^{-1}. Additionally, the hydrophobic alteration and 3D-printed microchannels created an icephobic surface that allowed for the quick and self-propelled removal of ice droplets, adding a new use for photothermal interfacial deicing. This work demonstrates hierarchical photothermal materials' rational construction and provides a path to circumventing current restrictions on solar-powered interfacial evaporation and clean water production.

In this study, researchers used composite photothermal inks and ink-extrusion 3D printing to create 3D aerogel matrices with various heights and pore diameters. According to Fig. 15 (a), the matrices were created to have square cross-sections with predicted areas of 20 × 20 mm^2 and wall thicknesses of 400 μm. Two conventional aerogels (SG1) and four aerogel matrices (SG2, SG3, SG4, and SG5) with different unit cell sizes were created for comparison. Among the 2 cm long aerogels, SG4 had the maximum water evaporation rate of 2.86 kg m^{-2} h^{-1} under 1 sun, outperforming SG2, SG3, and SG5. As shown in Fig. 15 (b), for aerogels with a height of 4 cm, SG4 had the maximum water evaporation rate of 3.74 kg m^{-2} h^{-1}, while SG1 had the lowest rate of 3.04 kg m^{-2} h^{-1}. Aerogels' higher height enhanced water evaporation rates due to larger actual evaporation regions. The water evaporation rates of the aerogels were determined in the presence of solar irradiation and airflow, as shown in Fig. 15 (c). When compared to calm air, the aerogels with

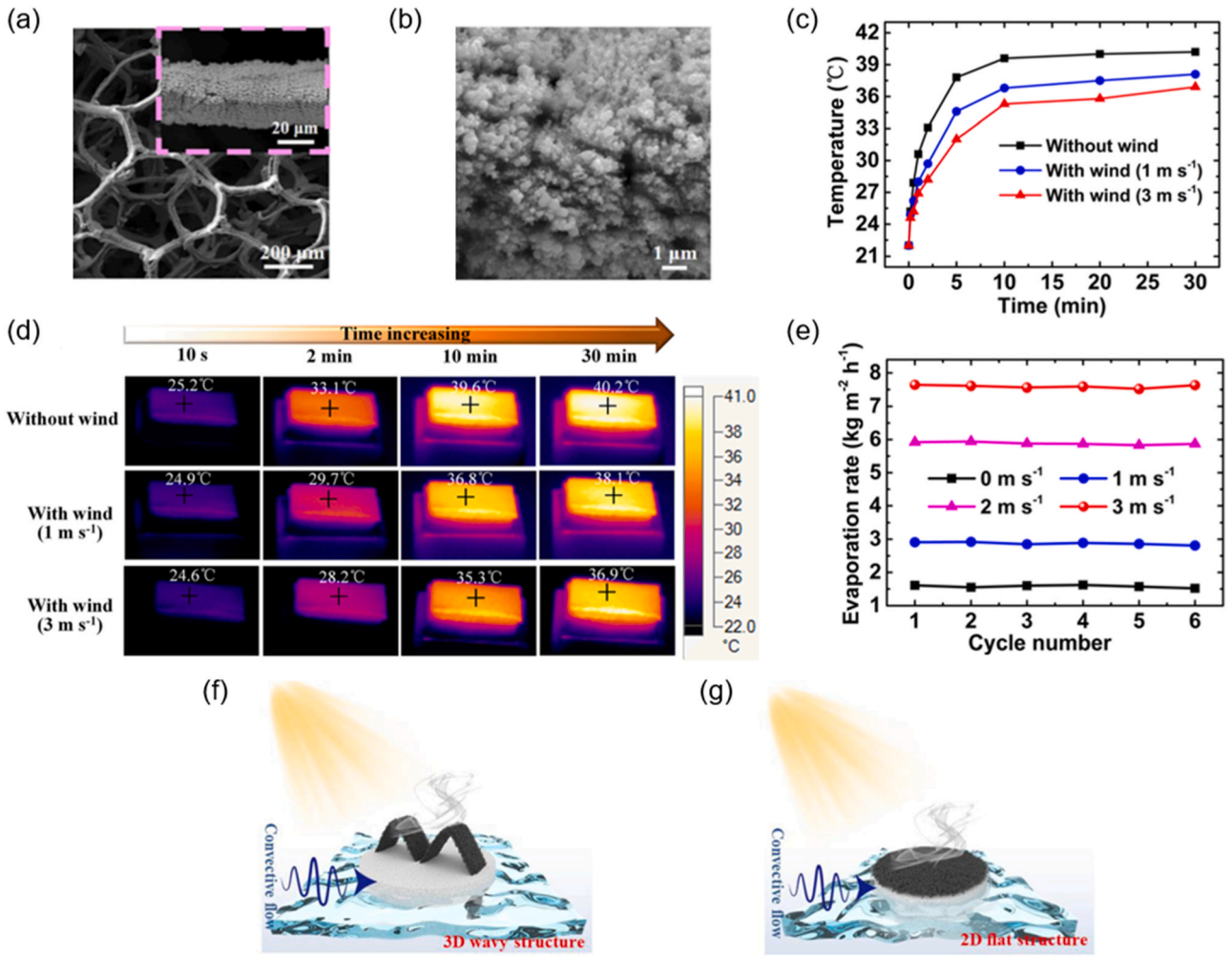

Fig. 14. The SEM image of the laser-treated copper foam at (a) low and (b) high magnification. (c) Photothermal behavior and (d) time-lapse IR images of the top surface of the laser-treated copper foam without and with the wind (1 and 3 m s^{-1}). (e) The cycle solar vapor test of the as-prepared evaporator without and with the wind (1, 2, and 3 m s^{-1}) under 1 sun. Copyright AIP Publishing, 2022. Illustration of solar evaporation in (f) the 3D wavy and (g) 2D structures under convective flow. Copyright Elsevier, 2021.
(a) Reproduced with permission from Ref. [60]. (b) Reproduced with permission from Ref. [61].

increased height (SG2-SG5) exhibited significantly higher evaporation rates under airflow. Water evaporation was aided by airflow in the lattice-structured 3D-printed aerogels (SG4 and SG5). Fig. 15 (d) shows thermal pictures and temperature distribution of 4 cm height aerogels captured with an infrared camera. The aerogels had "warm evaporation" portions on top and "cold evaporation" areas on the sides. Lower temperatures on the surface and lateral portions were caused by airflow, allowing for higher solar evaporation at lower temperatures. Fig. 15 (e, f) depicts computer models of air velocity and relative humidity distributions around the aerogels (SG1 and SG4). The SG4 lattice structure and through holes increased water vapor release while decreasing relative humidity on the outer surfaces and within the macroscopic pores. The simulations demonstrated the lattice structures' usefulness in airflow-enhanced steam generation. The schematics of the evaporation area and its actual pore size of SG1 to SG5 is shown in Fig. 15 (g) and (h), respectively. The real evaporation areas in still air and airflow were greatly increased because of the lattice structures of 3D-printed aerogels. Greater input of environmental energy and improved steam generation and release resulted from the lateral surfaces of SG2-SG5 being bigger than those of the traditional aerogel (SG1). Fig. 15 (i) demonstrates that the 3D-printed aerogel matrices (SG2-SG5) perform better in terms of water evaporation rates than traditional aerogels (SG1). One of the most effective 3D interfacial steam generators was SG4 with a lattice structure with through holes, which had the maximum evaporation rate of 3.74 kg m^{-2} h^{-1} in the presence of one sun and calm air. One of the highest recorded evaporation rates under various air velocities was achieved by SG4 with a mild breeze of 2 m s^{-1}. SG4's improved performance and cost-effectiveness are highlighted by the fact that it uses fewer raw materials than SG1 does. SG4 was hence picked for solar desalination tests and outdoor trials.

The solar-driven interfacial water evaporation has received a lot of attention because of the potential benefits, such as energy savings and low-cost water treatment. Photothermal-based evaporators have shown promising results by utilizing porous materials and hydrophilic coatings to efficiently create water vapor. However, water vapor transport inside these materials is frequently hampered by stagnation forces between the pores and vapor moisture, reducing water production. Zhang et al. [67] examined the most recent advances in solar-driven interfacial water evaporation, with a focus on the development of efficient solar evaporators for water treatment applications. Fig. 16 (a) emphasizes the importance of stable vapor diffusion for outdoor solar evaporators under variable wind flow directions and sun irradiation angles. Their novel strategy entails the creation of a low-tortuosity porous evaporator (LTPE) with 3D-interpenetrated channels inspired by nature. The LTPE's unique properties, such as its boundary layer thickness being independent of convective flow and its steady vapor diffusion capabilities in

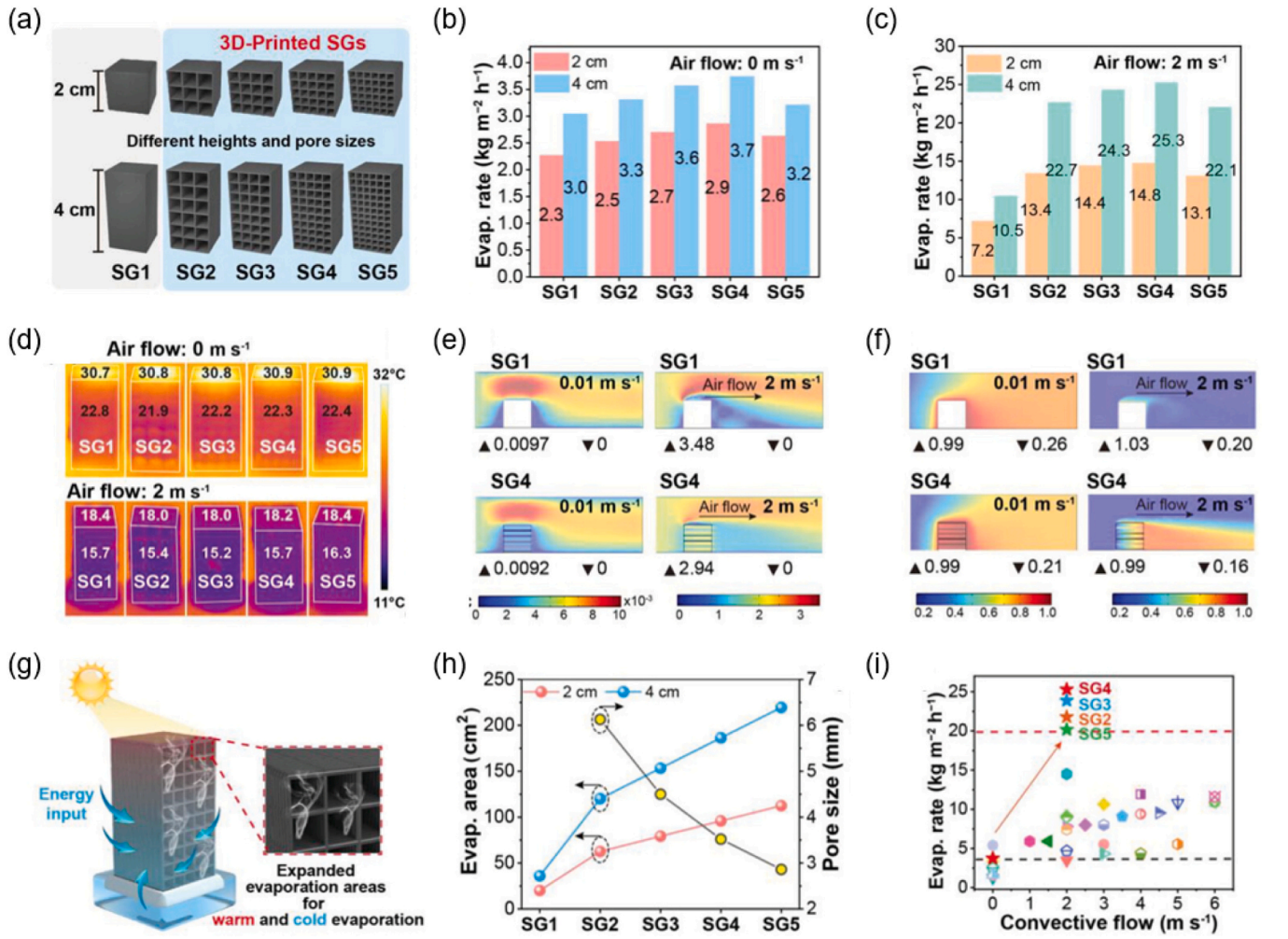

Fig. 15. (a) Schematic illustration of SG1-SG5. (b) Water evaporation rates under one sun with no breeze. (c) Water evaporation rates under 1 sun with airflow. (d) Infrared images and temperature distributions of SG1-SG5 with and without airflow under one sun. (e) The simulation of the distribution of air velocity around SG1 and SG4, whereas (f) the distribution of relative humidity at different air velocities. (g) The SG4 design for larger evaporation areas. (h) SG1-SG5 surface areas and macroscopic pore diameters. (i) The evaporation rates of SG1-SG5 at various air velocities. Reproduced with permission from Ref. [66]. Copyright Wiley, 2021.

arbitrary wind flow directions, pave the way for increased water evaporation rates. These results presented in Fig. 16 (b) demonstrate the promising potential of LTPE-based solar evaporators for practical water evaporation, particularly in energy-saving wastewater applications. Furthermore, as shown in Fig. 16 (c), the LTPE exhibits outstanding outdoor evaporation stability, giving a cumulative mass change of 47 kg m^{-2} and an average water evaporation rate of 3.9 kg m^{-2} h^{-1} during 12 hours of continuous exposure to natural wind and solar radiation. Under specified conditions, this study shows an astonishing record-high water evaporation rate of 16.8 kg m^{-2} h^{-1} for the LTPE as illustrated in Fig. 16 (d). The high solar and wind energy utilization efficiency of LTPE, together with its resistance to salt accumulation as shown in Fig. 16 (e), makes it a particularly appealing option for scalable and cost-effective water treatment solutions in distant and underdeveloped places. The findings of this work add to our understanding of sun-driven interfacial water evaporation and provide useful insights for constructing high-performance and sustainable solar evaporators for freshwater generation and wastewater treatment.

2.6. Other strategies

2.6.1. Electric energy input

Solar interfacial evaporators with excellent salt resistance and all-weather high evaporation performance are greatly desired for practical solar desalination yet are very challenging to develop. High evaporation performance and salt resistance are constrained by each other. High evaporation rate results in salt precipitation more easily, whereas excellent salt resistance is often at the sacrifice of the evaporation rate. However, highly salt-resistant, and all-weather solar interfacial evaporators have been reported [68–70]. The evaporators, which combine hydrophilic and hydrophobic layers, each of which is responsible either for the photothermal or electrothermal effects, feature a remarkably high evaporation rate under 1 sun as compensation, continuous vapor generation even in gloomy and dark environments, and long-term excellent salt-resistance without performance degradation and salt precipitation. Thus, Li et al. [71] developed a spongy Janus silicon structure coated with graphene, which can harvest input electrical energy simply by converting it into heat. Graphene here has two purposes, one is needed for electrical conductivity for electrothermal effect, based on Joule effect dissipation, and the second as a light-absorbing layer for photothermal effects. Silicon sponge provides a 3D network as well as serving as a hydrophobic layer that prevents salt accumulation. Under one sun and without any electrical energy input, the Janus evaporator exhibits an evaporation rate of 1.61 kg m^{-2} h^{-1} which increased to 2.34 kg m^{-2} h^{-1} via the application of an external voltage of +1 V and 1.0 sun. The highest evaporation rate of 6.53 kg m^{-2} h^{-1} was achieved at +5 V of external electrical power when placed under 1.0 sun. Later in the study, the authors supplied the electrical

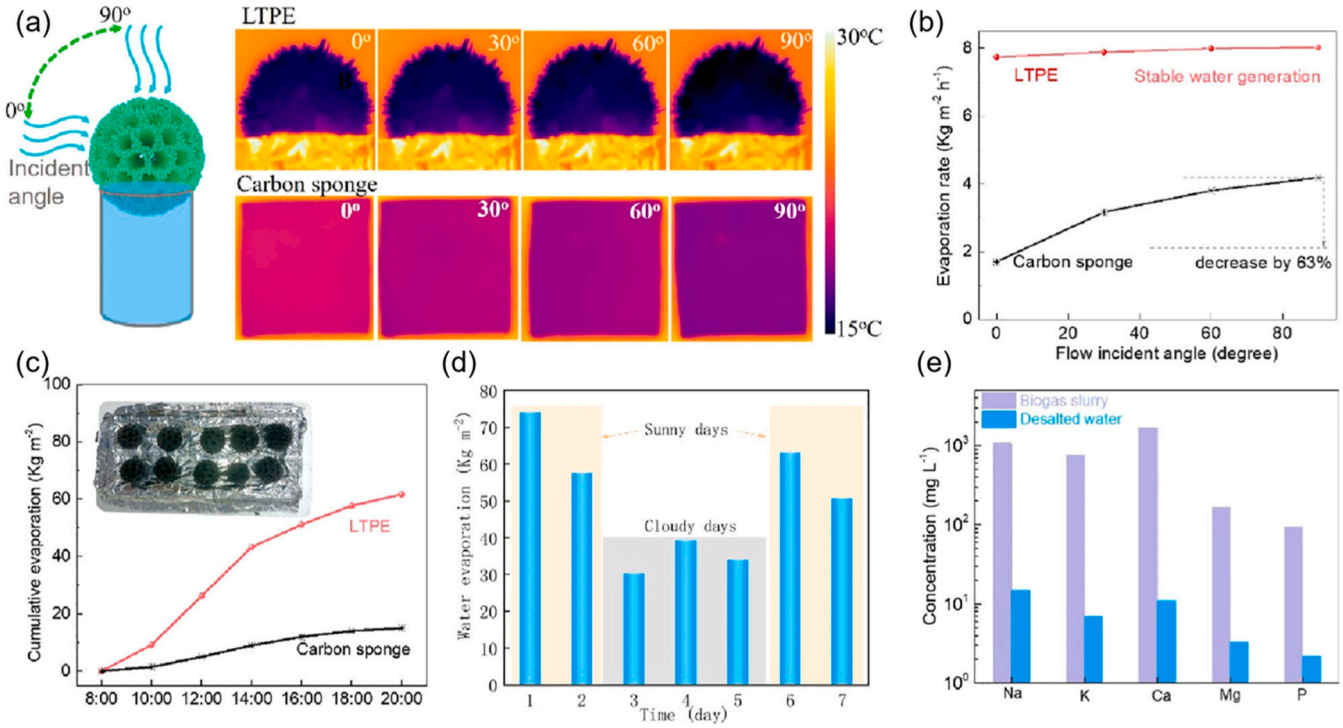

Fig. 16. Comparison of (a) infrared pictures and (b) water evaporation rates between LTPE and carbon sponge under convective flow from different directions. (c) A comparison of the outdoor water evaporation performance of LTPE with a carbon sponge. The outside large-scale equipment is shown in the inset. (d) Long-term test showing the LTPE's rapid outdoor water evaporation capability for biogas slurry treatment. (e) Purification of components in reclaimed water from biogas slurry to fulfill environmentally friendly discharge standards. Reproduced with permission from Ref. [67]. Copyright ACS, 2023.

energy from a connected solar cell to prove the real-world utility of their system. However, given the low efficiencies of commercial solar cells (< 25 %), this strategy of harvesting extra solar energy does not seem a promising path. This is mainly because solar absorbers have far higher solar-to-energy conversion ratios than solar cells and simply increasing the number of solar absorbers would give better solar-to-energy conversion outputs.

Similarly, Liu et al. [72] found out that the evaporation rate without voltage is 1.05 kg m^{-2} h^{-1}, for the carbon dots@CuS-loading carbonized polyacrylonitrile fibers under one sun. However, under application of 5 V, the system can reach evaporation rate equal to 6.66 kg m^{-2} h^{-1}.

Qiu et al. [73] developed an innovative Ti_4O_7 membrane featuring synergistic photothermal and electrothermal effects, with hydrophobic modifications at the interface between the membrane surface and water. This optimized self-floating membrane, which exhibits excellent sunlight absorption, achieved an exceptionally high evaporation rate of 7.51 kg m^{-2} h^{-1} under one sun illumination with a voltage of 3 V. Furthermore, the bilayered design of the membrane demonstrated efficient salt ion rejection, enhancing its potential for advanced solar desalination applications.

Wang et al. [74] created an integrated aerogel steam generating system that combines photo-thermal and electro-thermal effects to improve the evaporation rate. The researchers increased solar energy harvesting and electrical conductivity by employing aramid nano-fibers (ANFs) as the matrix material and adding CNTs and conductive PPy as photo-thermal and Joule heating materials, respectively. The resulting ANF/CNT/PPy aerogel evaporators demonstrated impressive vapor generation rates of 4.71 kg m^{-2} h^{-1} via photothermal conversion with solar energy alone as well as the photo-electro-thermal effect with a 5 V input, demonstrating a new and efficient approach for steam generation with increased evaporation rates. The aerogel evaporator also demonstrated promising salt tolerance and wastewater treatment capabilities.

In another study, Su et al. [75] presented an efficient technique for improving the efficiency of solar-driven interfacial evaporation for purifying salt-containing wastewater and seawater to produce sustainable clean water. The researchers obtained a record-high evaporation rate of 9.02 kg m^{-2} h^{-1} and solar-to-vapor efficiency of 287.4 % in salt brine by using commercial melamine sponge (MS)-supported reduced graphene oxides (MS@rGO) and photovoltaic electricity to power photothermal conversion. In addition, the system efficiently catalyzes oxygen reduction to produce H_2O_2, which acts as a broad-acting disinfectant in condensed water. Voltage application improves salt resistance and energy utilization efficiency, providing a cost-effective approach for highly efficient solar energy use in saline wastewater purification and seawater desalination.

Fang et al. [76] focused on a particular experimental setup using a tilted structure design with inexpensive carbon black materials (GCB) to address the lack of understanding of the underlying mechanism for evaporation-induced electricity in various materials and discussed the mechanism for solar irradiation-enhanced evaporation and electricity generation. As shown in Fig. 17 (a), the study introduces the concept of employing solar irradiation to accelerate water evaporation and explores the influence of flow-induced voltage within the GCB film. Experiments show that when water is driven under pressure through the porous GCB film, a voltage of approximately 0.38 V can be detected, as shown in Fig. 17 (b), and that this voltage is proportional to the applied pressure difference across the film, as shown in Fig. 17 (c). The observed voltage dependence is attributed to the streaming potential effect, where the negatively charged channels of the GCB film led to preferential transport of positively charged ions (H_3O^+) and higher potential downstream during water flow as shown by the schematics diagram in Fig. 17 (d). Furthermore, the authors emphasize that active metallic electrodes may not be directly related to the water evaporation rate for electricity generation, as opposed to their proposed solar-illuminated system, where output power enhancement is achieved through evaporation-driven streaming potential without active electrodes, as shown in Fig. 17 (d). This work underlines the possibility for further research into optimizing the material's structure, thickness, and surface

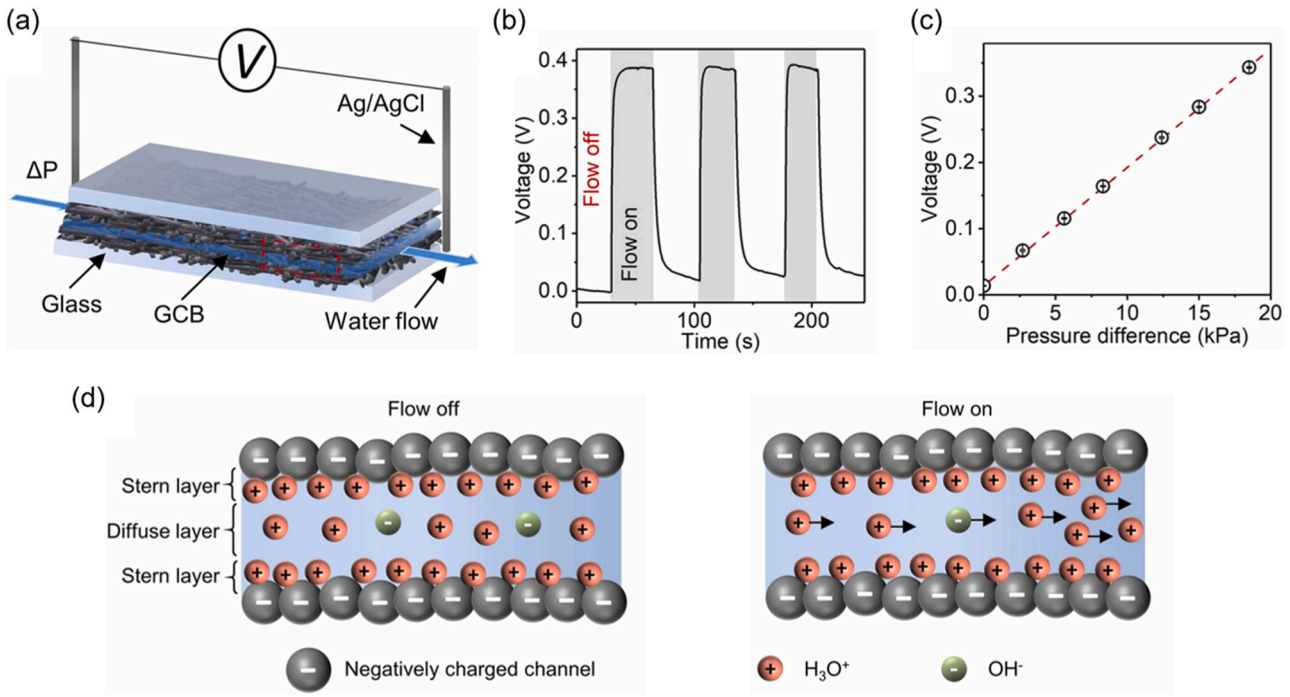

Fig. 17. (a) Schematic of the experimental setup for voltage measurement. (b) Voltage response measured while flowing water through the GCB film. (c) Voltage variation as a function of pressure difference applied across the GCB film. (d) Illustration of ion transport within negatively charged channels, emphasizing the streaming potential effect. Reproduced with permission from Ref. [76]. Copyright Elsevier, 2022.

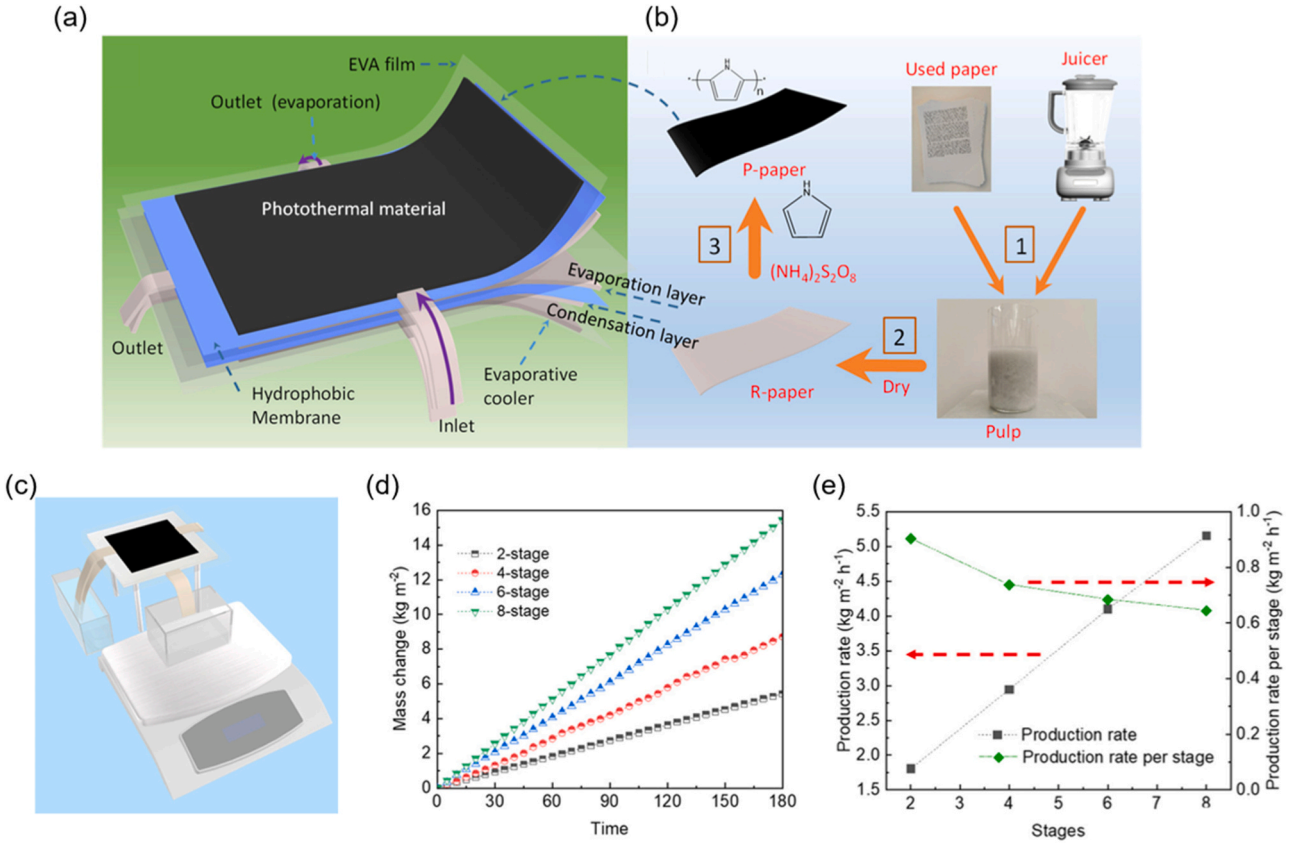

Fig. 18. Schematic illustration of the recycle of copy paper and structure of the flexible multistage membrane distillation (F-MSMD) device: (a) schematics of two-stage flexible paper-based MSMD; (b) recycle procedure of the copy paper (steps 1 and 2) and modification of the recycled paper by PPy (step 3). Clean water production performance of the F-MSMD device: (c) experimental setup; (d) mass change of the collected clean water from F-MSMD at different stages under one sun illumination; (e) relation between the clean water production rate and the number of stages. Reproduced with permission from Ref. [77]. Copyright ACS, 2021.

charge manipulation to improve the output performance of this innovative solar-irradiation-assisted power-generating approach.

2.6.2. Multistage membrane distillation

An interesting study by Wang et al. [77] utilized a novel multistage membrane distillation (MSMD) setup as depicted in Fig. 18. Each stage consists of a transparent thermal conduction layer, evaporation layer, hydrophobic porous membrane, and condensation layer. The evaporation layer consists of reused paper coated with black PPy. The water is transported to the photothermal layer via the siphoning effect due to the hydrophilic nature of reused paper. Underneath this there lies a hydrophobic polymeric separator membrane. The generated vapors pass through this membrane and condense underneath, thus effectively separating salt from water. With this design, the authors attained an evaporation rate of 3.6 kg m^{-2} h^{-1}. This design offers numerous advantages such as: (i) it is an all-in-one system where evaporation and condensation occur simultaneously, and clean water is collected; (ii) it utilizes the generated heat efficiently owing to numerous stages of heat extraction; (iii) it avoids accumulation of salt particles onto the evaporator as it concentrated sea water can be accumulated in another container.

Incorporating photothermal heating into the membrane distillation process involves integrating photothermal materials such as metallic nanostructures, inorganic semiconductor materials, carbon-based light-absorbing materials, and polymeric materials into the module structure, positioned near the feed surface. This approach aims to enhance energy absorption efficiency compared to convective fluid absorption, while also minimizing heat losses by placing the materials closer to the membrane interface. Gao et al. [78] classified three variations, the schematic of which is presented in Fig. 19, for incorporating photothermal materials into the membrane. In the embedding configuration Fig. 19 (a), these materials are uniformly mixed into the membrane structure. The bilayer configuration Fig. 19 (b) involves incorporating both the photothermal material and the membrane into a dual-layer module. In contrast, the isolation configuration Fig. 19 (c) separates the photothermal layer from the membrane, with heat being transferred to the membrane interface via the feed.

2.6.3. Electrochemical/electrothermal evaporation

Electrothermal evaporation and electrochemical evaporation are two distinct methods used for controlled evaporation processes. Electrothermal evaporation involves the application of heat to induce evaporation, while electrochemical evaporation utilizes electrochemical reactions to drive evaporation. Heat affects the evaporation rate of water by increasing the energy content of water molecules, making them more likely to overcome the intermolecular forces that hold them together in liquid form.

In the most recent study, G Jiang et al. [79] present a well-designed Thin-Film Water Evaporation System (TWES) featuring a 3D nanostructured microcone array, which effectively enhances water evaporation by addressing the trade-off between heat flux and liquid transport in the thin-film region. The incorporation of 3D nanostructured micro-steam volcanoes increases the surface area by 225 % and extends the thin-film evaporation area, while the triple-level wicking routes with multiscale structures facilitate liquid replenishment and thin-film maintenance at high speeds. The 3D thin-film configuration significantly improves the evaporation rate by 140 % and demonstrates the potential for high-flux evaporation in various applications. Under solar-driven conditions, the TWES achieves a remarkable water evaporation rate of 3.33 kg m^{-2} h^{-1}, among the highest reported for metal-based evaporators. Moreover, when attached to an electric-heating plate, the TWES achieves an electrothermal evaporation rate of 12.13 kg m^{-2} h^{-1} and efficiently reduces the temperature of a heat source by 36.2 °C. These findings highlight the potential of the ultra-thin pumpless TWES evaporator for large-scale applications in thermal management, offering a promising strategy for high-performance and cost-effective thin-film evaporators suitable for integration in various scenarios and devices.

The TWES demonstrates significantly superior optical absorption in the UV–vis–NIR region compared to the microgroove evaporation surface (MES) system. This improvement is attributed to the presence of nanoscale-feature-decorated microcones and increased surface oxygen content, facilitating efficient photothermal conversion. Importantly, the optical absorptance of the wet TWES remains consistently high, surpassing 85 %, similar to the dry TWES, even in practical working conditions, signifying its excellent photothermal conversion potential. Over time for pristine copper under one sun irradiation, the TWES, with its regular microcone array and substantial nanoparticles, experiences the highest temperature rise, reaching 67.2 °C from an initial temperature of 25 °C during the 300-second photothermal process. In comparison, the temperature rises for the MES and pristine copper surfaces are 51.6 °C and 42.1 °C, respectively, after the same duration of one sun irradiation.

As the solar flux decreases by 50 % and the placement angle changes from 0° to 60°, the surface temperature rise of the TWES diminishes from 67.2 °C to 48.3 °C. Solar irradiation intensity also influences the surface temperature rise. However, the loss of water during the process is relatively small and negligible compared to the overall mass change of the evaporators. Under solar irradiation, the TWES effectively generates vapor with visible steam observed under two-sun irradiation. The solar-driven evaporation rate of the TWES is 1.97 kg m^{-2} h^{-1} under one sun irradiation, surpassing the MES rate by 0.42 kg m^{-2} h^{-1}, highlighting the enhanced performance provided by the micro-steam volcanoes. The impact of irradiation intensity on evaporation performance reveals that higher solar flux leads to increased evaporation rates for both the MES and TWES. The TWES achieves an evaporation rate of 1.23 kg m^{-2} h^{-1} even under low solar irradiation intensity of 0.6 kW•cm^{-2}, indicating its usability on cloudy days.

Furthermore, the evaporation performance of the MES and TWES at

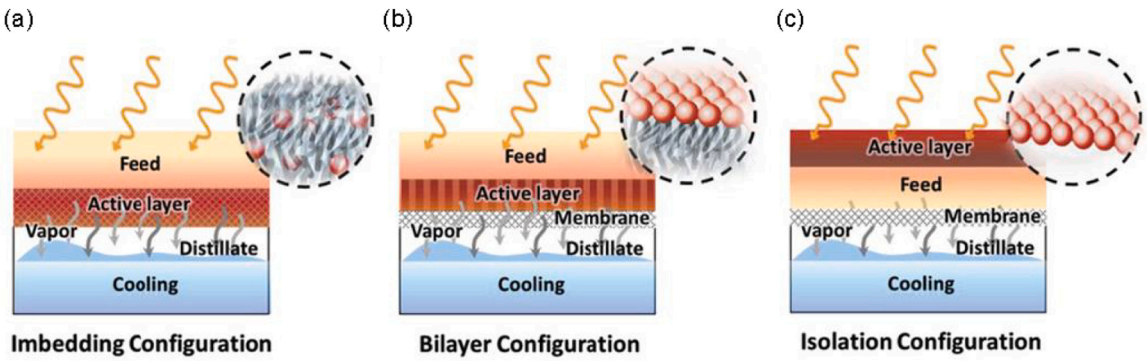

Fig. 19. Schematic diagrams of photothermal membrane distillation arrangements: (a) imbedding configuration, (b) bilayer configuration and (c) isolation configuration. Reproduced with permission from Ref. [78]. Copyright Wiley, 2021.

different placement angles is studied. As the placement angle increases, the solar flux decreases, resulting in reduced evaporation performance. However, even at a placement angle of 60° and a 50 % decrease in solar flux, the TWES maintains a relatively high evaporation rate of approximately 1.11 kg m^{-2} h^{-1}, showing its potential for operation at any time of the day. Additionally, the flexibility of adjusting the TWES to face the sun at different angles optimizes solar irradiation and further enhances evaporation performance.

3. Perspectives and challenges

In this review, we have explored and discussed in detail the strategies to obtain a high solar evaporation rate, highlighting the recent research developments, the current challenges, and the potential future paths. By examining these prospective avenues, we aim to provide insights into the opportunities and obstacles that lie ahead in achieving solar evaporation rates above 3 kg m^{-2} h^{-1} [52,71,80]. The following prospective areas highlight the potential future developments and opportunities for further advancements in this field:

3.1. Advanced materials and nanostructured surfaces

Future research can focus on the exploration and development of advanced materials and nanostructured surfaces specifically designed for enhanced solar evaporation. Nanoengineered materials, such as plasmonic nanoparticles, carbon-based nanomaterials, nanocomposites, and photonic crystals, offer unique properties that can manipulate light-matter interactions and boost energy absorption, thereby increasing the evaporation rates. Integration of these materials into the design of solar evaporators can lead to higher evaporation efficiencies and higher evaporation rates with much improved performance.

3.2. Novel solar absorbers and selective coatings

The design and development of novel solar absorbers and selective coatings hold immense potential for achieving higher evaporation rates. Ongoing research in the field of metamaterials and selective coatings aims to enhance the absorption of sunlight while minimizing thermal losses, including the design of the so-called selective solar absorbers. By tailoring the optical and thermal properties of these materials, researchers can optimize the conversion of solar energy into thermal energy, resulting in improved evaporation rates.

3.3. Multistage and multifunctional systems

Exploration of multistage and multifunctional systems can significantly contribute to achieving higher evaporation rates. Multistage solar evaporators, such as cascaded or stacked designs, allow for sequential utilization of solar energy and efficient utilization of the available heat. Additionally, incorporating multifunctional elements, such as heat exchangers, condensers, and energy storage components, can enhance system efficiency and provide opportunities for simultaneous heat recovery or utilization of waste heat, further boosting evaporation rates.

3.4. Advanced heat transfer and fluid dynamics

Efficient heat transfer and fluid dynamics play a crucial role in achieving higher evaporation rates. Future research can focus on optimizing the design and geometry of solar evaporators to enhance heat transfer and fluid flow characteristics. Innovative approaches, such as microchannel designs, enhanced surface textures, and structured flow patterns, can minimize thermal resistance and maximize fluid contact, leading to improved heat transfer and ultimately higher evaporation rates.

3.5. Integration with energy storage and management

Integration of solar evaporation systems with energy storage and management technologies can offer significant advantages. By coupling solar evaporation with thermal energy storage systems, the excess heat can be stored and utilized during periods of low solar irradiance, ensuring continuous operation and maintaining high evaporation rates. Additionally, advanced control and monitoring systems can optimize the operation of solar evaporators, taking into account environmental conditions and system performance for maximum efficiency.

3.6. Environmental sustainability and scalability

Future developments in solar evaporation should also prioritize environmental sustainability and scalability. Researchers can explore eco-friendly and biodegradable materials for solar absorbers and incorporate sustainable manufacturing processes. Additionally, efforts should be made to ensure the scalability of solar evaporation technologies, allowing for large-scale deployment in areas facing water scarcity challenges.

3.7. Challenges in achieving high solar evaporation rates under one sun irradiation

While the prospect of achieving high solar evaporation rates under one sun irradiation is enticing, several challenges need to be addressed to realize this goal. These challenges arise from the intricate interplay between various factors, including solar energy absorption, heat transfer, evaporation efficiency, and system design [44,49]. Understanding and mitigating the issues deriving from these challenges are essential for the successful development and deployment of efficient solar evaporation technologies.

3.8. Maximizing solar energy utilization

An essential challenge lies in optimizing the utilization of solar energy to enhance the efficiency of solar water evaporation systems. With limitations posed by the available energy flux under one sun irradiation, there is a critical need to develop highly efficient solar absorbers capable of capturing and converting a significant portion of incident solar energy into thermal energy. Central to this challenge is the improvement of spectral selectivity and absorption efficiency of solar absorber materials. Enhancing these properties is pivotal for maximizing energy absorption while minimizing losses attributed to reflection and transmission.

3.9. Heat transfer and thermal management

Efficient heat transfer is critical for achieving high evaporation rates. Effective heat transfer mechanisms must be employed to deliver thermal energy to the liquid interface rapidly. Heat losses to the surroundings must also be minimized through appropriate insulation and thermal management strategies. Enhancing the heat transfer coefficient and optimizing the thermal conductivity of materials involved in the system are key challenges in ensuring efficient heat transfer.

3.10. Evaporation enhancement

Enhancing evaporation efficiency is another challenge in achieving high solar evaporation rates. This involves overcoming mass transfer limitations and minimizing the resistance to vapor diffusion from the liquid interface. Strategies such as surface engineering, nanostructured coatings, and interfacial modifications can be explored to facilitate rapid evaporation and enhance the interfacial evaporation flux.

3.11. Competitive alternative to reverse osmosis systems

To effectively compete with reverse osmosis systems, the solar evaporation industry needs to use its inherent advantages while addressing key challenges. Besides being environmentally friendly, solar evaporation plants have lower operational costs once set up compared with reverse osmosis, as they primarily depend on sunlight for energy. However, to enhance competitiveness, technological advancements are crucial. Innovations in materials science can lead to more efficient solar absorbers, increasing the rate of evaporation. By investing in research and development to improve efficiency, reduce costs, and optimize processes, the solar evaporation industry can position itself as a competitor to reverse osmosis systems, especially in areas where solar energy is plentiful.

3.12. System design and scalability

Designing solar evaporation systems that are scalable, cost-effective, and adaptable to different environmental conditions is a significant challenge. The system should be capable of maintaining stable operation under varying solar irradiance, temperature, and humidity conditions. Furthermore, the integration of other components such as condensation systems, energy storage units, and water management modules adds complexity to the system design and requires careful consideration.

3.13. Durability and longevity

Ensuring the durability and longevity of solar evaporation systems is crucial for their practical implementation. Exposure to environmental factors, such as sunlight, moisture, and contaminants, can degrade the performance and functionality of the system over time. Developing materials with excellent stability, corrosion resistance, and long-term durability is vital to ensure the sustained operation of high-performance solar evaporators.

3.14. Standardization in measurement

It is crucial to standardize the testing procedure for solar water evaporation. For instance, as we have highlighted, the projected area of illumination used in several studies is not the same as the effective area of evaporation. Nonetheless, prevalent studies from the literature regarding solar water evaporation utilize only the projected area of evaporation even if they apply a long 3D structure. This put the innovative 2D materials at a disadvantage since their evaporation rates cannot even match the cold/under-dark evaporation rate of a 3D evaporator.

3.15. Applications of solar water evaporation

The primary application for solar water evaporation is production of fresh water from seawater and brackish water. It is especially useful in remote or off-grid areas where conventional desalination plants are not feasible due to lack of infrastructure or high energy costs. Promising progress has also been made recently in the development of solar-powered water-electricity generation, particularly for promoting decentralized and renewable solutions for areas with limited infrastructure. This novel method maximizes the use of solar energy by combining the production of electricity with water evaporation powered by the sun [81]. In contrast to conventional evaporation techniques resulting in significant energy losses, innovative designs that combine thermoelectric generators (TEG) and thermogalvanic generators (TGG) greatly improve efficiency [82]. Using materials such as Bi_2Te_3, TEGs serve as thermal insulators, increasing the rates at which water evaporates while generating energy at the same time. These integrated technologies provide dependable, affordable off-grid application solutions in addition to increasing efficiency.

Emerging sterilization and disinfection technologies are offering promising solutions to address pathogenic bacteria contamination in water. Recent developments indicate great potential for solar-powered systems. One technique employs a composite membrane-based device that produces steam using solar energy and offers a high sterilizing efficiency [83]. An affordable solar autoclave that successfully eliminates viruses and reduces carbon footprint is another breakthrough [84]. Concerning the problems with waterborne pathogens and public health, these developments represent an important advancement.

A promising method for treating water is the combination of photodegradation and steam generation. Using solar energy for photocatalytic processes and vapor generation, this approach effectively sterilizes microorganisms and purifies wastewater. Cutting-edge technologies like ZnO/gold particle-decorated membranes and spectrum-tailored solar harnessing aerogels show remarkable reductions in organic pollutants. This strategy provides a scalable and long-lasting solution to the problems of water scarcity and pollution [85].

Enhancing solar water evaporation rates with various approaches has important real-world applications, especially in water resource management. Evaluating these strategies' feasibility is crucial. Approaches such as using floating solar stills or using black surfaces to increase absorption are frequently workable and simple to implement into practice. Cost-effectiveness becomes evident as a crucial factor, particularly in large-scale applications. Even though some techniques, like building solar stills, may require higher initial costs, the long-term advantages in terms of water conservation generally outweigh the expenses. Furthermore, practical implementation relies on factors such as adaptability, scalability, and environmental sustainability. For example, evaporation surface area can be efficiently increased by technologies like spray systems, evaporative ponds, and porous materials. Evaporative ponds, while requiring ample space and regular maintenance, can offer practical solutions for wastewater management or brine disposal, particularly in regions with abundant land and water resources [86,87]. However, their feasibility depends on the following factors: land availability, maintenance needs, and environmental impact. Environmentally friendly and adaptable strategies are more likely to be widely used, particularly in areas with limited water resources. Scalability, cost-effectiveness, environmental sustainability, and compliance with regulations need to be carefully considered when assessing the practical implications of these solutions. Particular strategies might be immediately beneficial in certain situations, while others may require regular adjusting and customization. To promote the application of effective evaporation enhancement technologies and manage complicated problems related to water management and conservation, collaboration between industrial customers, research institutions, and governments is crucial.

4. Conclusion

Addressing these challenges requires interdisciplinary efforts and collaborative research endeavors. By systematically tackling these obstacles, researchers can unlock the full potential of high solar evaporation rates under one sun irradiation, advancing the field and facilitating the deployment of efficient and sustainable solar evaporation technologies.

Considering the energy shortage and environmental protection, producing clean water using solar energy is of great significance for sustainable development. This technology is low-cost and needs low energy consumption. In this review, how solar evaporators have achieved the above theoretical values has been discussed in detail (Table 1).

CRediT authorship contribution statement

Elisa Moretti: Writing – review & editing, Validation, Project administration, Funding acquisition. **Kamran Akbar:** Writing – review & editing, Writing – original draft, Investigation, Data curation,

Table 1
Solar water evaporation rates of materials under 1.0 sun and factors affecting these rates.

Material	Material Category	ER kg $m^{-2}h^{-1}$	Energy Efficiency, %	Surface Configuration	Energy Input other than Solar	Major Factors Responsible for High Evaporation Rate	Ref.
PVA/PPy	Hydrogel/Organic Absorber	3.2	94	2D	-	efficient Water Transport, lower Vaporization Enthalpy	[44]
Agar Gel/TiN	Hydrogel/Organic Absorber	5.15	-	2D	-	efficient Water Transport	[46]
Wood with thermal insulator underneath	Biomass/Absorber	3.92	-	2D	-	minimizing heat loss	[50]
Copper sponge with Nano textured surface	Metal	7.6	85.9	2D	Wind @ 3 m s^{-1}	wind Energy	[60]
Paper/PPy/Membrane	Multistage layers	3.6	-	2D	-	efficient design	[77]
PAA-PEDOT	Hydrogel/ Inorganic Absorber	3.05	95	2D	-	efficient Water Transport	[88]
PCH-Chitosan Gel-Hukaiwen Ink	Hydrogel/Carbon Ink	3.3	-	2D	-	efficient Water Transport	[80]
MoS2/Graphene Hydrogel	Hydrogel/ Inorganic Absorber	3.2 @ 0.9 sun	-	2D	-	efficient Water Transport, lower Vaporization Enthalpy	[89]
MXene/polydopamine (PDA)	Hydrogel/ Inorganic Absorber	3.02	94.7	2D	-	efficient Water Transport lower Vaporization Enthalpy	[90]
PVA/Graphene Oxide Hydrogel	Hydrogel/ Inorganic Absorber	3.24	99.98	2D	-	efficient Water Transport, lower Vaporization Enthalpy	[91]
Gellan gum /Cuttlefish ink	Hydrogel/Organic Absorber	3.1	-	2D	-	efficient Water Transport	[92]
Schiff-base hydrogel with Au as absorber	Hydrogel/Au	3.12	-	2D	-	efficient Water Transport	[93]
Carbon Hollow Microfibers	Carbonized Cotton	3.2	92	2D	-	efficient Water Transport	[94]
Fe- metal-organic framework (MOF)/hydrogel	Inorganic Absorber/ Hydrogel	3.2	-	2D	-	efficient Water Transport	[95]
Balsa Wood	Biomass	3.91	-	3D	Environmental	3D design/porous structure	[25]
V-RGO Foam	Synthetic foam	3.39	104.1	3D	-	porous 3D structure, enthalpy Reduction	[43]
PVA/PPy	Hydrogel/Organic Absorber	3.6	96	3D	-	3D Design, lower Vaporization Enthalpy	[45]
PVA-Ti_3C_2	Hydrogel/ Inorganic Absorber	6.35	-	3D	-	efficient Water Transport, 3D design	[35]
PDMS foam with Cu_7S_4-MoS_2-Au nanoparticles	Synthetic foam with inorganic absorber	3.824	96.6	3D	-	porous 3D structure, low thermal conductivity	[51]
TPA-BTDH	Synthetic foam with sensitizer	3.6	-	3D	-	porous 3D structure, low thermal conductivity	[52]
3D Cellulose	Synthetic 3D structure	3.01	-	3D	-	porous 3D structure, enthalpy Reduction	[47]
Bamboo Fiber cloth/rGO aerogel/ Conductive Aluminium	Aerogel/inorganic absorber	5.40	-	3D	Environmental	environmental Energy Harvesting, 3D design	[53]
Graphene aerogel on Cotton	Aerogel/inorganic absorber	7.6	178.6	3D	Environmental	3D design, environmental Energy Harvesting	[54]
Carbonized Sugar	Carbonized Carbon	10.9	-	3D	Wind @ 6 m s^{-1}	wind Energy, porous Structure	[58]
Carbonized luffa sponge	Carbonized Carbon	14.5	-	3D	Wind @ 2 m s^{-1}	wind Energy, porous Structure	[59]
Carbon Nanotubes/paper	Carbon Allotropes	5.55	278	3D	Wind @ 5 m s^{-1}	wind Energy, 3D design	[61]
Silicon/graphene sponge	Synthetic Foam with graphene absorber	6.53	-	3D	5 V electric potential	electric Energy, 3D structure	[71]
Sodium Alginate/Polyamine/Carbon Nanotubes	Inorganic Hydrogel/ Polymer/Absorber	3.2	95	3D	-	efficient Water Transport, 3D structure	[96]
Oxidized copper foam with Ge NPs/ PMMA	Inorganic support/ Absorber with thin PMMA cover	3.2	-	3D	-	minimizing heat loss	[97]
Ti_2O_3/PVA	Inorganic Absorber/ Hydrogel	3.6	~90	3D	-	efficient Water Transport	[98]
Janus PDA/(3-aminopropyl) triethoxy-silane /TiO_2-PPy hollow fiber membrane	Multilayer components	3.65	229.13	3D	Environmental	3D design/porous structure	[99]
Polyacrylonitrile/carbon nanotubes	Carbon based/ Polymer	8.31		3D	Wind @ 4 m s^{-1}	3D design/concave- convex shape/ hierarchical porous microstructure	[62]
WS_2-O-doped-graphene heterostructures/ melamine foam	Carbon based	3.23	121.8	3D		3D design/excellent hydrophilicity and self-containing water ability	[100]
Reduced graphene oxide/polyvinyl alcohol phosphate ester	Hybrid aerogel	16.22		3D	Wind @ 2.5 m s^{-1}	3D design/ interconnected pore structure	[63]
Covalent organic framework/ graphene dual-region hydrogel	Hydrogel	3.69	92	3D		3D design/ interconnected pore structure/Janus structure	[101]

(*continued on next page*)

Table 1 (*continued*)

Material	Material Category	ER kg $m^{-2}h^{-1}$	Energy Efficiency, %	Surface Configuration	Energy Input other than Solar	Major Factors Responsible for High Evaporation Rate	Ref.
PPC/polyacrylamide	Hydrogel	4.85		3D		3D design/ interconnected pore structure	[102]
MoS_2-MXene@ phase change material paraffin		3.2		3D		3D design/ hydrophobic evaporator to prevent salt crystallization	[103]
Carbon fiber coated by quinoa cellulose nanosheet activated by ZnCl2	Carbon-based	3.2		2D		unique surface microstructures of decorated CF/super-hydrophilicity/enough water transmission channel	[104]
Lotus-inspired biomimetic evaporator (LBE)	Organic based	3.23	153.20	3D		3D lotus-inspired biomimetic architecture/Janus structure	[105]
Carbon nanotubes/ poly(3,4-ethylenedioxythiophene):poly (styrene sulfonate) and	Hybrid	6.8	94.9	3D		3D design/hierarchical porous structure/ anti-salt fouling capability/ negatively-charged ionic channels	[106]
Ti_4O_7 Nanofibrous Membrane		7.51		2D	3 V electric potential	electric Energy/3D structure/ Janus structure/interconnected porous network	[73]
Graphene oxides upon porous melamine sponge	Carbon-based	3.47	97.4			superior water acti- vation property resulted/reduced water vaporization enthalpy	[107]
Highly interconnected carbon-based sponge	Carbon-based	3.87	>95	3D		3D/highly interconnected sponge (HIS)	[108]
Closed-cell 3D polymer foams	Hybrid	5.8	>90	3D		3D design/porous and hydrophilic structure	[109]
Carbonized luffa vines	Carbonized biomass	3.26	118	3D		3D design/excellent salt-deposition resistance	[110]
Polyion complex hydrogel/coal powder composite (HCC)-based	Hydrogel	3.12	88.83	3D		3D design/microporous structure of HCC	[111]
3D hydrogel industrial carbon nanotubes and polyacrylamide	Hydrogel	12.2		3D		3D design/anti-salt accumulation	[112]
Positively charged hydrogel immobilizing with protonated amine groups (R-NH3 +)	Hydrogel	3.3	95	2D		Janus structure	[80]
PVA/acidified carbon nanotubes (ACNTs) composite hydrogel	Hydrogel	3.85	87.6	3D		Excellent light absorption/heat localization/water transport capabilities	[113]
Amorphous Ta_2O_5/C nanocomposite hollow multishelled structure	Composite	4.02				hollow multishelled structure results in decreased water evaporation enthalpy	[114]
Cu−$Cu(OH)_2$-MOF foam	Biomimetic foam	11.58	160.07	3D	Wind @ 5.8 m s^{-1}	wind energy/pine needle-like hierarchical structures	[64]
Carbon nanoparticles-coated cotton fiber	Carbon-based	5.04		3D		3D/highly interconnected structure	[115]
Single-stage distillation devices modified with hydrophobic fumed silica		5.03	82.5	3D		3D design/ 10-stage multistage distillation device	[116]
Azo-rich covalent organic frameworks		3.02	94	2D		Janus structure	[117]
Carbon nanotubes-agar into polyacrylamide hydrogel	hydrogel	3	86.2	2D		hydroxyl groups rampart on the skeleton	[118]
Polyzwitterionic hydrogels	hydrogel	4.14	94	3D	10 wt% brine	3D design/more hydrated polymer network	[119]
Ovalbumin-polyacrylamide hydrogel foam was	hydrogel	3		3D	0.6 sun	3D design/water transport capabilities/anti-salt accumulation	[120]
Carbonized sunflower stalk	Carbonized Biomass	11.62	344.69	3D		3D design/water transport capabilities/salt resistant	[34]
Carbon felt	Carbon-based	5.37		2D		high surface area/ high pore density/uniform fibrous microstructures.	[121]
Aero-cryogel monolith		5.67	93.6	3D	Wind @ 3 m s^{-1}	Wind energy/3D design/ hierarchical porous structure	[122]
PPy-coated bacterial cellulose hydrogel	hydrogel	5.88	83.4	3D	Under 70 ℃ heating conditions	superior salt-rejecting ability/ excellent antifouling properties	[123]
Zn doping 1 T-MoS_2	Modified bio-waste sorghum straw	4.13		3D	Wind @ 4 m s^{-1}	wind energy/3D design/ antifouling property with	[124]
Au/ceramic	Inorganic	5.52		3D	Wind @ 3 m s^{-1}	wind energy/rational T-shaped thermal management	[125]
PVA/activated carbon/sponge	Carbon-based	4.47		3D	Under 1 sun and employing aluminum foil chimneys of 26 cm	chimney effect/high water supply	[126]

(*continued on next page*)

Table 1 (*continued*)

Material	Material Category	ER kg $m^{-2}h^{-1}$	Energy Efficiency, %	Surface Configuration	Energy Input other than Solar	Major Factors Responsible for High Evaporation Rate	Ref.
Modified bio-based floatable assembly	Biomass	3.2		3D		water transportation by micro-vessels and self-floatability	[127]
Biomimetic hydrogels with multilevel structures inspired by Setaria viridis	Hydrogel	3.5		3D		3D design/multi- structured hierarchical systems (conical spines, a groove structure, and aligned vertical channels)	[128]
$C_3N_4/NiIn_2S_4$ heterostructure	Transition metal chalcogenides hybrid	3.25	215.06	2D		absorb sunlight well/ increase the material interface temperature/ promote water evaporation	[129]
Fiber-based cigarette filter in polyvinyl alcohol /MXene	Carbonized biomass	3.38	132.9	3D		3D design/ porous architecture/ hydrophilic feature	[130]
Hazardous and noxious substance trapping device		12.28	81	3D		installation of Al mirrors on the reverse piloti structure (RPS)	[131]
Coating of biomimetic leaf structures (24 leaves) with reduced graphene oxide	Biomass	3.1		2D		increase in the effective evaporation surface area	[132]
Sodium polyacrylate/CNTs	Carbon-based	7.47	> 99 %	2D	Wind @ 5 m s^{-1}	wind energy/larger actual evaporation area/reasonable water distribution on the evaporation surface	[133]
Chitosan/agarose-multiwalled CNTs	Organic/carbon-based	3.07	85.28	3D		unique mixed pore structure with low tortuosity	[134]
CNTs decorated silk fibroin protein coating	Carbon-based	3.2	94	3D		porous structure/strong water–silk fibroin interactions	[135]
Potato-based microporous carbon cake	Biomass	3.18		3D		3D design/ interconnected pores/ super-hydrophilic surfaces	[136]
Carbon black particles /PVA/ polyethyleneimine polymeric nanonetworks in CNT cellular structures facilitated	Hydrogel	3.55	92	3D		3D interconnected porous structure/ interfacial dehydration	[137]
Nitrogen-doped CNTs encapsulated with Co/carbon fibers	Hybrid	3.85	98	3D		deliberate 3D structure/ porous structure/confined effect of Co-NCNT	[138]
Powder active carbon and Fe_3O_4 in PVA and polystyrene sulfonate (PSS)	Hydrogel	3.43	93.4	3D		Janus structure/hydrogel network	[139]
Fe_3C@ Enteromorpha doped graphene aerogels	Aerogel	3.76	127	3D		Janus structure/ salt resistance/ rich microporous structure	[140]
Magnetic three-dimensional hydrophilic carbon fiber felt	Carbon-based	7.05		3D	5 kW m^{-2}	magnetic field/3D design	[141]
Multilayer graphene oxide/ bacterial cellulose hydrogel	Hydrogel/carbon-photothermal layer	4.51	80	3D		3D design/porous structure with gradient pores	[142]
Agarose-polyvinylpyrrolidone composite hydrogel	Hydrogel	3.2	90.5	3D		3D design/microchannel structure	[143]
Chitosan/lignin hybrid aerogel with carbon nanoparticles and Ag NPs	Aerogel	3.569	92.05	3D		hydrophilicity/ synergetic effect/ salt resistance	[144]
Wood-derived porous carbon/ polymetallic oxide nanoparticles	Carbonized biomass	3.23	93	3D		3D design/hierarchical structures/ vertically aligned channels	[145]
Fe@ Enteromorpha/graphene	Aerogel	3.85		3D		3D design/ introducing a cold evaporation surface for additional environmental energy input	[146]
Coated on cotton fabrics CNTs via PVP	Carbon-based	4.55	168.43	2D		design of siphon effect/salt resistance	[147]
Black cotton cloth/EPS foam/twisted air-laid paper	Carbon-based	8.32	73.21	2D	10 sun	hydrophilicity	[148]
Laser etched cooper plating layer/ carbon-fiber fabric	Multulayer Carbon-based	3.39	96.69	2D		multilayer honeycomb structure	[149]
Carbon fibre-cotton-based cone	Biomass/carbon-based	3.27	194.4	3D		3D design/tunable water supply (via the traditional basket-weaving strategy)	[150]
Carbonized corrugated paper/MnO_2		4.314		3D		semihollow 3D structure/effective salt resistance/ porous structure/ presence of oxygen-containing functional groups	[151]
Poly(hydroxyethyl methacrylate)/ acrylic acid-based melamine foam evaporator	Hydrogel	3	90	3D		3D skeleton-supported design/ interconnected porous structure	[152]
Polydopamine-modified $Cu_{2-x}Se$ nano-composites	Composite	3.36		2D	0.5 sun	core-shell structure	[153]
Carbon nanofiber reinforced carbon aerogel	Carbon-based	3.82	95.5	3D		heteroatom doping/ hierarchically porous structure/ superhydrophilicity/salt resistance	[154]

(*continued on next page*)

Table 1 (*continued*)

Material	Material Category	ER kg $m^{-2}h^{-1}$	Energy Efficiency, %	Surface Configuration	Energy Input other than Solar	Major Factors Responsible for High Evaporation Rate	Ref.
3D fabric evaporator decorated by the hydrophilic polydopamine /polyethyleneimine and Ti3C2Tx	Carbonized	3.95		3D		3D fabric evaporator with vertical hemp-yarn arrays/multiscale pores	[155]
Carbonized sorghum straw/ wall of the 3D evaporator	Carbonized	3.27	131.2	3D		3D cup-shaped design/ super-hydrophilic characteristic/ well heat-shielding performance	[156]
C/$ZnFe_2O_{4-x}$ composite deposited on floral foam	Organic based	4.06	95.4	3D		3D design/excellent salt inhibition properties	[157]
Ionic covalent organic framework STTP	Organic based	3.55	95.8	2D		inclusion of ST-related ionic moieties improved the photothermal conversion, and reduced the water phase change enthalpy	[158]
CuS NPs/agarose gel coated oxidized cooper foam cube		4.14		3D		open interconnected pores/salt resistance	[159]
Starch and chitosan/PDA-Fe NPs	Biomass hybrid hydrogel	3.9	103.2	3D		3D design/hierarchical porous structure	[160]
PVA/MXene-decorated wood		4.31	114	3D		porous channels/intrinsic hydrophilicity of the delignified wood	[161]
Graphene wrapped Fe_3O_4 nanoparticles	Carbon-based	5.9		3D		well- designed hierarchical structure/variable magnetic field	[162]
Fe3O4- glass bubbles-cellulose/ polyvinyl alcohol	Aerogel	3.17		3D		hierarchical coordinated control strategy/salt resistance	[163]
Fused deposition modeling 3D-printed evaporator	biomimetic	4.02	220.34	3D		volcanic-shaped 3D hierarchical structure	[164]
MoS2 nanosheet arrays on activated Ti mesh		7.88	86		6 wt% brine, 3 sun	serpentine and unidirectional fluidic structure	[165]
PPy-coated nonwoven fabrics		4.75	259	3D		3D mirror-assisted and concave pyramid-shaped design/salt resistance	[166]
Wood-inspired bimodal evaporator	Biomass	3.02	91.8	3D		leaves-on-stem architecture/salt-resistance/hierarchical design/ bimodal porous structure configuration	[167]
Carbon nanofiber/graphene oxide composite	Aerogel	3.47	97.5	3D		3D design/salt-resistance/ hierarchical interconnected channels	[168]
Natural wood-derived all-carbon conductive foam	Biomass	6.73		3D	2 V input voltage	3D cross- linked bimodal cavities/ micro mesoporous structure/salt resistance	[169]
PPy/alginate/poly(n-isopropylacrylamide) hydrogel composed of alginate, poly(N-isopropylacrylamide), and PPy	Hydrogel	4.145	97	3D		3D thermoresponsive/great water release ability of polymer	[170]
Vertically arranged carbon nanotube	Aerogel	3.26	86.8	3D		3D design/super- hydrophilicity/ salt-resistance	[171]
PPy supramolecular network-packed photothermal aerogel	aerogel	3.61	97.1	3D		supramolecular network/salt resistance/reduced heat loss	[172]
Diesel particulate soot-incorporated 3D polyvinyl alcohol-based hydrogel	Hydrogel	3.01		3D		hydrophilicity/intrinsic heat localization/ excellent water transport capability	[173]
Bioinspired composite fibrous framework	Biomass	4.58	173	3D		3D design/super- hydrophilicity/ salt-resistance	[174]
Polyacrylonitrile@CoMn- layered double hydroxide membrane		3.12	94.5			hierarchical structure/the rich –OH groups in LDHs	[175]
Zeolitic imidazolate framework −67@MXene/rGO decorated rock wool		3.81	153.7	3D		hierarchical structure/improved wettability and microchannels	[176]
Reshapable $Ti_3C_2T_x$ MXene/GO/ polyaniline (PANI) (MGP) hybrids	Hybrid	3.94	135.6	3D		flower-shaped/patternable surfaces/ reduced water vaporization enthalpy/porous structure	[177]
Carbon black PVA- SO_4^{2-}	Hydrogel	3.52	97.2	3D		tunable molecular and microporous structure in large scale/interconnected porous structure	[178]
Calcinated super absorbent polymer+PVA+yogurt evaporator		3.25	96.47	3D		3D design/reducing the evaporation enthalpy of water/ interconnected porous structure	[179]
Ag-MnO2 nanostructure with N-doped graphene aerogel	Aerogel	8.57		3D	outdoor environment	unique 3D structural design by incorporating catalytic nanostructure	[65]

(*continued on next page*)

Table 1 (*continued*)

Material	Material Category	ER kg $m^{-2}h^{-1}$	Energy Efficiency, %	Surface Configuration	Energy Input other than Solar	Major Factors Responsible for High Evaporation Rate	Ref.
PVA−agar incorporated with multi-walled CNT	Hydrogel	3.1	140	3D		minimal thermal losses and continuous water supply during	[180]
Graphite/geopolymer composite		3.23	186.46	3D		good hydrophilicity/photothermal performance/salt resistance	[181]
Cu_2-$ZnSnS_4$	Hydrogel	3.249	96.3	3D		good salt resistance/ anti-bacterial properties	[182]
Polystyrene sulfonate modified polyvinyl alcohol/ oxidized carbon black	hydrogel	3.68	91.1	3D		hierarchically nanostructure/ vertically aligned microchannels/ salt resistance due to ions selectivity of the nanochannel	[183]
CNFs-COO^-/chitosan, CNFs-Si, and steel ball	Aerogel	4.21		3D		3D hierarchically nanostructure	[184]
Quinoa bran cellulose and and graphene oxide	Aerogel	3.6		3D		excellent deposited salt self-cleaning performance/the self-cleaning mechanism/porous structure	[185]
Au@Ag-Pd trimetallic nanostructure/polystyrene microsphere	Composite	3.04	99.1	2D		Janus structure/synergic effect	[186]
Highly hydratable hydrogel network (modified needle coke and PVA)	hydrogel	3.18	99	3D		hierarchically porous/highly hydratable structure/robust desalination durability	[187]
Graphene/poly(N-acryloyl glycinamide)		3.4	93	3D		3D bio-inspired lotus-petiole-mimetic microstructured	[188]
CuO/Cu_2O	Inorganic	3.2		2D		hollow multishelled structure/ hierarchical porous structure	[189]
3D folded structure		3.22		3D		7-stage device/effective salt tolerance	[190]
MOF coated with carbon cloth	Carbon-based	5.5		3D	5 V input voltage	coupling the photo- thermal evaporation and the Joule heating effec	[191]
Double network pure natural Nicandra physalodes (Linn.) Gaertn. -PVA/PPy	Hydrogel	3.51			0.78 kW m^{-2}	hydrogen bonds with excessive hydroxyl groups	[192]
Molecularly engineered zwitterionic hydrogel with incorporated phenyl-methylene-imidazole motif	Hydrogel	3.17	87.8	3D		salt binding ability/boosted hydration/improved salt tolerance/ultra-low evaporation enthalpy/durable anti-microbial ability in brine	[193]

Conceptualization. **Alberto Vomiero:** Writing – review & editing, Supervision, Funding acquisition, Conceptualization. **Anastasiia Taranova:** Writing – original draft, Formal analysis, Data curation, Conceptualization. **Ghulam Dastgeer:** Writing – original draft, Formal analysis, Data curation.

Declaration of Competing Interest

The authors declare that they have no known competing financial interests or personal relationships that could have appeared to influence the work reported in this paper.

Data availability

Data will be made available on request.

Acknowledg= ements

A.V. acknowledges the Knut & Alice Wallenberg Foundation, the Swedish Foundations Consolidator Fellowship, and the Kempe Foundation, Sweden for partial funding. The authors acknowledge the Italian Ministry of University and Research for partial funding through PNRR NEST project ("Network4 Energy Sustainable Transition", European Union–NextGenerationEU: Project code PE0000021).

References

[1] United Nations. Summary Progress Update 2021: SDG 6 — water and sanitation for all. UN-Water integrated monitoring initiative. Published online 2021:1-58. ⟨https://www.unwater.org/new-data-on-global-progress-towards-ensuring-water-and-sanitation-for-all-by-2030/⟩.
[2] E. Schlager, Managing water for people and nature, Science (1979) 292 (5519) (2001) 1071–1072, https://doi.org/10.1126/science.1058821.
[3] Z. Xi, S. Li, L. Yu, H. Yan, M. Chen, All-day freshwater harvesting by selective solar absorption and radiative cooling, ACS Appl. Mater. Interfaces 14 (22) (2022) 26255–26263, https://doi.org/10.1021/acsami.2c05409.
[4] J.R. Werber, C.O. Osuji, M. Elimelech, Materials for next-generation desalination and water purification membranes, Nat. Rev. Mater. 1 (2016), https://doi.org/10.1038/natrevmats.2016.18.
[5] J. Chen, Y. Huang, N. Zhang, et al., Micro-cable structured textile for simultaneously harvesting solar and mechanical energy, Nat. Energy 1 (10) (2016), https://doi.org/10.1038/nenergy.2016.138.
[6] G.G. Wallace, J. Chen, A.J. Mozer, M. Forsyth, D.R. MacFarlane, C. Wang, Nanoelectrodes: energy conversion and storage, Mater. Today 12 (6) (2009) 20–27, https://doi.org/10.1016/S1369-7021(09)70177-4.
[7] A. Nattestad, S. Beirne, S. Fang, et al., Carbon nanotube-reduced graphene oxide composites for thermal energy harvesting applications, Adv. Mater. 25 (45) (2013) 6602–6606. ⟨http://ro.uow.edu.au/aiimpapers/979⟩.
[8] L. Chennan, G. Yogi, S. Elias, Solar assisted sea water desalination: a review, Renew. Sustain. Energy Rev. 19 (2013) 136–163. ⟨http://ac.els-cdn.com/S1364032112006017X/1-s2.0-S136403211200617X-main.pdf?_tid=ef470378-4cef-11e7-9cef-00000aab0f01&acdnat=1496998085_4145c2b6e65952863a90f02b713fb5fb⟩.
[9] L. Zhu, T. Ding, M. Gao, C.K.N. Peh, G.W. Ho, Shape conformal and thermal insulative organic solar absorber sponge for photothermal water evaporation and thermoelectric power generation, Adv. Energy Mater. 9 (22) (2019), https://doi.org/10.1002/aenm.201900250.
[10] S. Chu, Y. Cui, N. Liu, The path towards sustainable energy, Nat. Mater. 16 (1) (2016) 16–22, https://doi.org/10.1038/nmat4834.
[11] C. Chen, Y. Kuang, L. Hu, Challenges and opportunities for solar evaporation, Joule 3 (3) (2019) 683–718, https://doi.org/10.1016/j.joule.2018.12.023.

[12] N.S. Lewis, Research opportunities to advance solar energy utilization, Science (1979) 351 (6271) (2016), https://doi.org/10.1126/science.aad1920.
[13] M. Elimelech, W.A. Phillip, The future of seawater desalination: Energy, technology, and the environment, Science (1979) 333 (6043) (2011) 712–717, https://doi.org/10.1126/science.1200488.
[14] A.D. Khawaji, I.K. Kutubkhanah, J.M. Wie, Advances in seawater desalination technologies, Desalination 221 (1-3) (2008) 47–69, https://doi.org/10.1016/j.desal.2007.01.067.
[15] F R, Desalination freshens up, Science (1979) 313 (5790)) (2006) 1088.
[16] Y. Li, T. Gao, Z. Yang, et al., 3D-Printed, all-in-one evaporator for high-efficiency solar steam generation under 1 sun illumination, Adv. Mater. 29 (26) (2017), https://doi.org/10.1002/adma.201700981.
[17] H. Bai, T. Zhao, M. Cao, Interfacial solar evaporation for water production: From structure design to reliable performance, Mol. Syst. Des. Eng. 5 (2) (2020) 419–432, https://doi.org/10.1039/c9me00166b.
[18] S.L. Wu, H. Chen, H.L. Wang, X. Chen, H.C. Yang, S.B. Darling, Solar-driven evaporators for water treatment: challenges and opportunities, Environ. Sci. (Camb. 7 (1) (2021) 24–39, https://doi.org/10.1039/d0ew00725k.
[19] Y. Sun, X. Zong, D. Qu, et al., Water management by hierarchical structures for highly efficient solar water evaporation, J. Mater. Chem. A Mater. 9 (11) (2021) 7122–7128, https://doi.org/10.1039/d1ta00113b.
[20] M. Mustakeem, J.K. El-Demellawi, M. Obaid, F. Ming, H.N. Alshareef, N. Ghaffour, MXene-coated membranes for autonomous solar-driven desalination, ACS Appl. Mater. Interfaces 14 (4) (2022) 5265–5274, https://doi.org/10.1021/acsami.1c20653.
[21] L. Huang, J. Pei, H. Jiang, X. Hu, Water desalination under one sun using graphene-based material modified PTFE membrane, Desalination 442 (2018) 1–7, https://doi.org/10.1016/j.desal.2018.05.006.
[22] B. Zhang, P.W. Wong, A.K. An, Photothermally enabled MXene hydrogel membrane with integrated solar-driven evaporation and photodegradation for efficient water purification, Chem. Eng. J. 430 (2022) 133054, https://doi.org/10.1016/j.cej.2021.133054.
[23] A. Taranova, K. Akbar, K. Yusupov, et al., Unraveling the optoelectronic properties of CoSbx intrinsic selective solar absorber towards high-temperature surfaces, Nat. Commun. 14 (1) (2023) 7280, https://doi.org/10.1038/s41467-023-42839-6.
[24] X. Li, J. Li, J. Lu, et al., Enhancement of interfacial solar vapor generation by environmental energy, Joule 2 (7) (2018) 1331–1338, https://doi.org/10.1016/j.joule.2018.04.004.
[25] J. Tang, T. Zheng, Z. Song, et al., Realization of low latent heat of a solar evaporator via regulating the water state in wood channels, ACS Appl. Mater. Interfaces 12 (16) (2020) 18504–18511, https://doi.org/10.1021/acsami.0c01261.
[26] C. Dang, M. Chen, L. Huang, et al., A multichannel photothermal rod for antigravity water transportation and high-flux solar steam generation, J. Mater. Chem. A Mater. 10 (35) (2022) 18116–18125, https://doi.org/10.1039/d2ta05395k.
[27] X. Li, G. Ni, T. Cooper, et al., Measuring conversion efficiency of solar vapor generation, Joule 3 (8) (2019) 1798–1803, https://doi.org/10.1016/j.joule.2019.06.009.
[28] M. Qin, S. Li, Y. Zhao, et al., Unprecedented synthesis of Holey 2D layered double hydroxide nanomesh for enhanced oxygen evolution, Adv. Energy Mater. 9 (1) (2019), https://doi.org/10.1002/aenm.201803060.
[29] J. Li, Y. Li, W. Song, X. Li, L. Yang, L. Yan, Boosting interfacial solar steam generation by three-dimensional bilayer cellulose aerogels, J. Colloid Interface Sci. 650 (2023) 339–349, https://doi.org/10.1016/j.jcis.2023.06.205.
[30] H. Yang, D. Li, X. Zheng, et al., High freshwater flux solar desalination via a 3D PLasmonic Evaporator with an Efficient Heat-mass Evaporation Interface, Adv. Mater. 35 (47) (2023) e230469, https://doi.org/10.1002/adma.202304699.
[31] Y. Chen, J. Hao, J. Xu, Z. Hu, H. Bao, H. Xu, Pickering emulsion templated 3D cylindrical open porous aerogel for highly efficient solar steam generation, Small 19 (48) (2023) 2303908, https://doi.org/10.1002/smll.202303908.
[32] Y. Shao, J. Li, Y. Li, et al., In situ polymerization of three-dimensional polypyrrole aerogel for efficient solar-driven interfacial evaporation and desalination, Colloids Surf. A Physicochem Eng. Asp. 680 (2024) 132662, https://doi.org/10.1016/j.colsurfa.2023.132662.
[33] Y. Bian, Q. Du, K. Tang, et al., Carbonized bamboos as excellent 3D solar vapor-generation devices, Adv. Mater. Technol. 4 (4) (2019) 1–7, https://doi.org/10.1002/admt.201800593.
[34] Z. Feng, X. OuYang, S. Zhou, et al., Carbonized sunflower stalks with or without storage tissue for highly efficient water purification and desalination, J. Environ. Chem. Eng. 11 (3) (2023) 110284, https://doi.org/10.1016/j.jece.2023.110284.
[35] C. Li, L. Fan, R. Zhu, et al., Adjusting channel size within PVA-based hydrogels via ice templating for enhanced solar steam generation, ACS Appl. Energy Mater. 3 (9) (2020) 9216–9225, https://doi.org/10.1021/acsaem.0c01584.
[36] M. Ding, D. Zhao, H. Liu, et al., Ink-stained chalk: a low-cost 3D evaporator for efficient and stable solar desalination, Sol. RRL 7 (9) (2023) 230002, https://doi.org/10.1002/solr.202300026.
[37] M. Wang, Z. Sun, J. Zhou, et al., Robust and temperature-sensitive hydrogels for high-efficiency water harvesting under low solar energy radiation, Sol. RRL 7 (9) (2023), https://doi.org/10.1002/solr.202300041.
[38] L. Hao, N. Liu, H. Bai, P. He, R. Niu, J. Gong, High-performance solar-driven interfacial evaporation through molecular design of antibacterial, biomass-derived hydrogels, J. Colloid Interface Sci. 608 (2022) 840–852, https://doi.org/10.1016/j.jcis.2021.10.035.
[39] X. Zhou, F. Zhao, Y. Guo, Y. Zhang, G. Yu, A hydrogel-based antifouling solar evaporator for highly efficient water desalination, Energy Environ. Sci. 11 (8) (2018) 1985–1992, https://doi.org/10.1039/c8ee00567b.
[40] K. Kudo, J. Ishida, G. Syuu, Y. Sekine, T. Ikeda-Fukazawa, Structural changes of water in poly(vinyl alcohol) hydrogel during dehydration, J. Chem. Phys. 140 (4) (2014), https://doi.org/10.1063/1.4862996.
[41] X. Zhou, F. Zhao, Y. Guo, B. Rosenberger, G. Yu, Architecting highly hydratable polymer networks to tune the water state for solar water purification, Sci. Adv. 5 (6) (2019), https://doi.org/10.1126/sciadv.aaw5484.
[42] A. Chand, D.K. Sahoo, A. Rana, S. Jena, H.S. Biswal, The prodigious hydrogen bonds with sulfur and selenium in molecular assemblies, structural biology, and functional materials, Acc. Chem. Res 53 (8) (2020) 1580–1592, https://doi.org/10.1021/acs.accounts.0c00289.
[43] W. Li, X. Tian, X. Li, et al., Ultrahigh solar steam generation rate of a vertically aligned reduced graphene oxide foam realized by dynamic compression, J. Mater. Chem. A Mater. 9 (26) (2021) 14859–14867, https://doi.org/10.1039/d1ta03014k.
[44] F. Zhao, X. Zhou, Y. Shi, et al., Highly efficient solar vapour generation via hierarchically nanostructured gels, Nat. Nanotechnol. 13 (6) (2018) 489–495, https://doi.org/10.1038/s41565-018-0097-z.
[45] Y. Shi, O. Ilic, H.A. Atwater, J.R. Greer, All-day fresh water harvesting by microstructured hydrogel membranes, Nat. Commun. 12 (1) (2021), https://doi.org/10.1038/s41467-021-23174-0.
[46] Y. Tian, X. Liu, S. Xu, et al., Recyclable and efficient ocean biomass-derived hydrogel photothermal evaporator for thermally-localized solar desalination, Desalination 523 (August 2021)) (2022) 115449, https://doi.org/10.1016/j.desal.2021.115449.
[47] J.J. Koh, G.J.H. Lim, S. Chakraborty, et al., Robust, 3D-printed hydratable plastics for effective solar desalination, Nano Energy 79 (August 2020)) (2021) 105436, https://doi.org/10.1016/j.nanoen.2020.105436.
[48] L. Gkoura, G. Diamantopoulos, M. Fardis, et al., The peculiar size and temperature dependence of water diffusion in carbon nanotubes studied with ^{2}D NMR diffusion-relaxation D-T 2 effspectroscopy, Biomicrofluidics 14 (3) (2020), https://doi.org/10.1063/5.0005398.
[49] X. Wu, Z. Wu, Y. Wang, T. Gao, Q. Li, H. Xu, All-cold evaporation under one sun with zero energy loss by using a heatsink inspired solar evaporator, Adv. Sci. 8 (7) (2021) 1–10, https://doi.org/10.1002/advs.202002501.
[50] J. Chen, D. Zhang, S. He, et al., Thermal insulation design for efficient and scalable solar water interfacial evaporation and purification, J. Mater. Sci. Technol. 66 (2021) 157–162, https://doi.org/10.1016/j.jmst.2020.05.075.
[51] H. Wang, R. Zhang, D. Yuan, S. Xu, L. Wang, Gas foaming guided fabrication of 3D porous plasmonic nanoplatform with broadband absorption, tunable shape, excellent stability, and high photothermal efficiency for solar water purification, Adv. Funct. Mater. 30 (46) (2020) 1–8, https://doi.org/10.1002/adfm.202003995.
[52] H. Li, W. Zhu, M. Li, et al., Side area-assisted 3D evaporator with antibiofouling function for ultra-efficient solar steam generation, Adv. Mater. 33 (36) (2021) 2102258, https://doi.org/10.1002/adma.202102258.
[53] Y. Wang, X. Wu, P. Wu, et al., Enhancing solar steam generation using a highly thermally conductive evaporator support, Sci. Bull. (Beijing) 66 (24) (2021) 2479–2488, https://doi.org/10.1016/j.scib.2021.09.018.
[54] T. Gao, X. Wu, Y. Wang, G. Owens, H. Xu, A hollow and compressible 3D photothermal evaporator for highly efficient solar steam generation without energy loss, Sol. RRL 5 (5) (2021) 1–9, https://doi.org/10.1002/solr.202100053.
[55] J. Wen, X. Li, H. Zhang, et al., Architecting Janus hydrogel evaporator with polydopamine-TiO2 photocatalyst for high-efficient solar desalination and purification, Sep Purif Technol 304 (2023), https://doi.org/10.1016/j.seppur.2022.122403.
[56] R. Jin, P. Guo, X. Wang, L. Heng, B. Wang, A renewable and antibacterial solar evaporator for efficient seawater desalination: performance analysis and empirical formula, Adv. Sustain Syst. 2300082 (2023) 1–10, https://doi.org/10.1002/adsu.202300082.
[57] L. Peng, X. Gu, H. Yang, D. Zheng, P. Wang, H. Cui, Ultra-high evaporation rate 3D evaporator with vertical sheets based on full use of convection flow, J. Clean. Prod. 345 (February)) (2022) 131172, https://doi.org/10.1016/j.jclepro.2022.131172.
[58] J. Li, X. Wang, Z. Lin, et al., Over 10 kg m−2h−1 evaporation rate enabled by a 3D interconnected porous carbon foam, Joule 4 (4) (2020) 928–937, https://doi.org/10.1016/j.joule.2020.02.014.
[59] J. Choi, H. Lee, B. Sohn, M. Song, S. Jeon, Highly efficient evaporative cooling by all-day water evaporation using hierarchically porous biomass, Sci. Rep. 11 (1) (2021) 1–9, https://doi.org/10.1038/s41598-021-96303-w.
[60] K. Yin, Z. Wu, J. Wu, Z. Zhu, F. Zhang, J.A. Duan, Solar-driven thermal-wind synergistic effect on laser-textured superhydrophilic copper foam architectures for ultrahigh efficient vapor generation, Appl. Phys. Lett. 118 (21) (2021), https://doi.org/10.1063/5.0050623.
[61] X. Liu, Z. Liu, D. Devadutta Mishra, Z. Chen, J. Zhao, C. Hu, Evaporation rate far beyond the input solar energy limit enabled by introducing convective flow, Chem. Eng. J. 429 (June 2021)) (2022) 132335, https://doi.org/10.1016/j.cej.2021.132335.
[62] Y. Liu, B. Luo, H. Liu, et al., 3D printed electrospun nanofiber-based pyramid-shaped solar vapor generator with hierarchical porous structure for efficient desalination, Chem. Eng. J. 452 (P3)) (2023) 139402, https://doi.org/10.1016/j.cej.2022.139402.
[63] J. Li, Y. Shao, W. Song, et al., Ultrahigh solar vapor evaporation rate of super-hydrophilic aerogel by introducing environmental energy and convective flow,

Chem. Eng. J. 466 (April)) (2023) 143281, https://doi.org/10.1016/j.cej.2023.143281.
[64] H. Wang, C. Zhang, X. Ji, et al., Over 11 kg m-2h-1 evaporation rate achieved by cooling metal-organic framework foam with pine needle-like hierarchical structures to subambient temperature, ACS Appl. Mater. Interfaces 14 (8) (2022) 10257–10266, https://doi.org/10.1021/acsami.1c20769.
[65] Y. Tian, C. Du, S. Yong, X. Zhou, C. Zhou, S. Yang, Catalysis-involved 3D N-doped graphene aerogel achieves a superior solar water purification rate and efficiency, Chem. Eng. J. 453 (P1)) (2023) 139793, https://doi.org/10.1016/j.cej.2022.139793.
[66] N. Li, K. Shao, J. He, et al., Solar-powered interfacial evaporation and deicing based on a 3D-printed multiscale hierarchical design, Small 2301474 (2023) 1–15, https://doi.org/10.1002/smll.202301474.
[67] Z. Zhang, W. Xu, J. Wang, et al., Improving solar vapor generation by eliminating the boundary layer inhibition effect of evaporator pores, ACS Energy Lett. 8 (5) (2023) 2276–2283, https://doi.org/10.1021/acsenergylett.3c00183.
[68] L. Zhang, X. Li, Y. Zhong, et al., Highly efficient and salt rejecting solar evaporation via a wick-free confined water layer, Nat. Commun. 13 (1) (2022), https://doi.org/10.1038/s41467-022-28457-8.
[69] C. Dang, H. Wang, Y. Cao, et al., Ultra salt-resistant solar desalination system via large-scale easy assembly of microstructural units, Energy Environ. Sci. 15 (12) (2022) 5405–5414, https://doi.org/10.1039/d2ee03341k.
[70] Y.Q. Luo, F. Song, X.L. Wang, Y.Z. Wang, Water bridge solar evaporator with salt-resistance and heat localization for efficient desalination, J. Mater. Chem. A Mater. 11 (6) (2023) 3118–3125, https://doi.org/10.1039/d2ta09244a.
[71] L. Li, J. Zhang, Highly salt-resistant and all-weather solar-driven interfacial evaporators with photothermal and electrothermal effects based on Janus graphene@silicone sponges, Nano Energy 81 (November 2020)) (2021) 105682, https://doi.org/10.1016/j.nanoen.2020.105682.
[72] C. Liu, J. Su, Q. Chang, Y. Li, J. Yang, S. Hu, Electricity-boosted solar-to-vapor conversion upon fiber-supported CDs@CuS for rapidly vaporizing seawater, Sol. RRL 6 (8) (2022), https://doi.org/10.1002/solr.202200170.
[73] X. Qiu, H. Kong, Y. Li, Q. Wang, Y. Wang, Interface engineering of a Ti4O7 nanofibrous membrane for efficient solar-driven evaporation, ACS Appl. Mater. Interfaces 14 (49) (2022) 54855–54866, https://doi.org/10.1021/acsami.2c15997.
[74] M. Wang, X. Zhang, C. Chen, et al., Aramid-based aerogels for driving water evaporation through both photo-thermal and electro-thermal effects, J. Mater. Chem. A Mater. 11 (14) (2023) 7711–7723, https://doi.org/10.1039/d2ta09950k.
[75] J. Su, Q. Chang, C. Xue, J. Yang, S. Hu, Sponge-supported reduced graphene oxides enable synergetic photothermal and electrothermal conversion for water purification coupling hydrogen peroxide production, Sol. RRL 6 (11) (2022), https://doi.org/10.1002/solr.202200767.
[76] S. Fang, W. Chu, J. Tan, W. Guo, The mechanism for solar irradiation enhanced evaporation and electricity generation, Nano Energy 101 (2022), https://doi.org/10.1016/j.nanoen.2022.107605.
[77] W. Wang, Y. Shi, C. Zhang, et al., Solar seawater distillation by flexible and fully passive multistage membrane distillation, Nano Lett. 21 (12) (2021) 5068–5074, https://doi.org/10.1021/acs.nanolett.1c00910.
[78] M. Gao, C.K. Peh, F.L. Meng, G.W. Ho, Photothermal Membrane Distillation toward Solar Water Production, Small Methods 5 (5) (2021) 1–17, https://doi.org/10.1002/smtd.202001200.
[79] G. Jiang, L. Wang, Z. Tian, C. Chen, X. Hu, R. Peng, Boosting water evaporation via continuous formation of a 3D thin film through triple-level super-wicking routes, Mater. Horiz. (2023), https://doi.org/10.1039/D3MH00548H (Published online).
[80] Q. Xiao, Y. Zhu, Y. Xi, et al., Highly charged hydrogel with enhanced donnan exclusion toward ammonium for efficient solar-driven water remediation, Chem. Eng. J. 430 (P3)) (2022) 133019, https://doi.org/10.1016/j.cej.2021.133019.
[81] T. Ding, Y. Zhou, W.L. Ong, G.W. Ho, Hybrid solar-driven interfacial evaporation systems: Beyond water production towards high solar energy utilization, Mater. Today 42 (2021) 178–191, https://doi.org/10.1016/j.mattod.2020.10.022.
[82] Y. Zhou, T. Ding, M. Gao, et al., Controlled heterogeneous water distribution and evaporation towards enhanced photothermal water-electricity-hydrogen production, Nano Energy 77 (July)) (2020) 105102, https://doi.org/10.1016/j.nanoen.2020.105102.
[83] Y. Zhang, D. Zhao, F. Yu, et al., Floating rGO-based black membranes for solar driven sterilization, Nanoscale 9 (48) (2017) 19384–19389, https://doi.org/10.1039/c7nr06861a.
[84] J. Li, M. Du, G. Lv, et al., Interfacial solar steam generation enables fast-responsive, energy-efficient, and low-cost off-grid sterilization, Adv. Mater. 30 (49) (2018), https://doi.org/10.1002/adma.201805159.
[85] X. Wang, Y. He, X. Liu, Synchronous steam generation and photodegradation for clean water generation based on localized solar energy harvesting, Energy Convers. Manag 173 (2018) 158–166, https://doi.org/10.1016/j.enconman.2018.07.065.
[86] A. Ahmadinik, A. Rahimikhoob, S. Aliniaeifard, Water use efficiency in novel integrated system of greenhouse and saltwater evaporative pond, Desalination 496 (2020), https://doi.org/10.1016/j.desal.2020.114698.
[87] S.R. Khalifeh Soltani, A. Mostafaeipour, K. Almutairi, S.J. Hosseini Dehshiri, S. S. Hosseini Dehshiri, K. Techato, Predicting effect of floating photovoltaic power plant on water loss through surface evaporation for wastewater pond using artificial intelligence: a case study, Sustain. Energy Technol. Assess. 50 (2022), https://doi.org/10.1016/j.seta.2021.101849.
[88] Y. Peng, S. Tang, X. Wang, R. Ran, A high strength hydrogel with a core–shell structure simultaneously serving as strain sensor and solar water evaporator, Macromol. Mater. Eng. 306 (10) (2021) 1–11, https://doi.org/10.1002/mame.202100309.
[89] Y. Li, X. lei Shi, L. jie Sun, et al., Composite hydrogel-based photothermal self-pumping system with salt and bacteria resistance for super-efficient solar-powered water evaporation, Desalination 515 (June)) (2021) 115192, https://doi.org/10.1016/j.desal.2021.115192.
[90] M. Pi, X. Wang, Z. Wang, R. Ran, Sustainable MXene/PDA hydrogel with core-shell structure tailored for highly efficient solar evaporation and long-term desalination, Polymers 230 (August)) (2021) 124075, https://doi.org/10.1016/j.polymer.2021.124075.
[91] Y. Chen, X. Zhao, Z. Ye, Y. Chen, P. Lin, Robust seawater desalination and sewage purification enabled by the solar-thermal conversion of the Janus-type graphene oxide evaporator, Desalination 522 (2022) 115406, https://doi.org/10.1016/j.desal.2021.115406.
[92] X. Liu, Y. Tian, Y. Wu, et al., Fully biomass-based hybrid hydrogel for efficient solar desalination with salt self-cleaning property, ACS Appl. Mater. Interfaces (2021), https://doi.org/10.1021/acsami.1c11636 (Published online).
[93] J. Ren, S. Yang, Z. Hu, H. Wang, Self-Propelled Aerogel Solar Evaporators for Efficient Solar Seawater Purification, Langmuir 37 (31) (2021) 9532–9539, https://doi.org/10.1021/acs.langmuir.1c01387.
[94] S. Lei, D. Huang, S. Liu, et al., Templating synthesis of natural cotton-based hierarchically structured carbon hollow microfibers for high-performance solar vapor generation, J. Mater. Chem. A Mater. 9 (27) (2021) 15346–15354, https://doi.org/10.1039/d1ta02117f.
[95] Y. Guo, H. Lu, F. Zhao, X. Zhou, W. Shi, G. Yu, Biomass-derived hybrid hydrogel evaporators for cost-effective solar water purification, Adv. Mater. 32 (11) (2020) 1–8, https://doi.org/10.1002/adma.201907061.
[96] C. Liu, Y. Peng, X. Zhao, Flower-inspired bionic sodium alginate hydrogel evaporator enhancing solar desalination performance, Carbohydr. Polym. 273 (August)) (2021) 118536, https://doi.org/10.1016/j.carbpol.2021.118536.
[97] Y. Xu, Z. Qi, Z. Luo, et al., Heat-concentrating solar steam generation and salt extraction based on water-repellent germanium nanoparticles-coated oxidized copper foams, Sol. Energy Mater. Sol. Cells 230 (May)) (2021) 111191, https://doi.org/10.1016/j.solmat.2021.111191.
[98] Y. Guo, X. Zhou, F. Zhao, J. Bae, B. Rosenberger, G. Yu, Synergistic energy nanoconfinement and water activation in hydrogels for efficient solar water desalination, ACS Nano 13 (7) (2019) 7913–7919, https://doi.org/10.1021/acsnano.9b02301.
[99] C. Wei, X. Zhang, S. Ma, et al., Ultra-robust vertically aligned three-dimensional (3D) Janus hollow fiber membranes for interfacial solar-driven steam generation with salt-resistant and multi-media purification, Chem. Eng. J. 425 (May)) (2021) 130118, https://doi.org/10.1016/j.cej.2021.130118.
[100] L. Wang, G. Yang, L. Jiang, et al., Improved photo-excited carriers transportation of WS2-O-doped-graphene heterostructures for solar steam generation, Small (2022), https://doi.org/10.1002/smll.202204898 (Published online).
[101] C. Li, S. Cao, J. Lutzki, et al., A covalent organic framework/graphene dual-region hydrogel for enhanced solar-driven water generation, J. Am. Chem. Soc. 144 (7) (2022) 3083–3090, https://doi.org/10.1021/jacs.1c11689.
[102] J. Zhou, Z. Sun, X. Mu, et al., Highly efficient and long-term stable solar-driven water purification through a rechargeable hydrogel evaporator, Desalination 537 (1)) (2022) 115872, https://doi.org/10.1016/j.desal.2022.115872.
[103] Z. Guo, W. Zhou, N. Arshad, et al., Excellent energy capture of hierarchical MoS2 nanosheets coupled with MXene for efficient solar evaporators and thermal packs, Carbon N. Y. 186 (2022) 19–27, https://doi.org/10.1016/j.carbon.2021.09.066.
[104] J. Yang, X. Suo, J. Zhao, et al., Carbon fiber coated by quinoa cellulose nanosheet with outstanding scaled salt self-cleaning performance and purification of organic and antibiotic contaminated water, Sci. Rep. 12 (1) (2022) 1–11, https://doi.org/10.1038/s41598-022-12889-9.
[105] R. Zhang, B. Xiang, Y. Wang, S. Tang, X. Meng, A lotus-inspired 3D biomimetic design toward an advanced solar steam evaporator with ultrahigh efficiency and remarkable stability, Mater. Horiz. 9 (4) (2022) 1232–1242, https://doi.org/10.1039/d1mh02020j.
[106] Y. Xu, J. Xu, J. Zhang, et al., All-in-one polymer sponge composite 3D evaporators for simultaneous high-flux solar-thermal desalination and electricity generation, Nano Energy 93 (October 2021)) (2022) 106882, https://doi.org/10.1016/j.nanoen.2021.106882.
[107] J. Su, Q. Chang, C. Xue, J. Yang, S. Hu, Electrochemical oxidation reconstructs graphene oxides on sponge for unprecedentedly high solar water evaporation, Carbon N. Y 194 (2022) 267–273, https://doi.org/10.1016/j.carbon.2022.04.011.
[108] Z. Mao, Y. Chen, G. Li, et al., Highly interconnected sponge with optimized water absorption and thermal conductivity for efficient solar desalination, Sep Purif. Technol. 314 (February)) (2023) 123502, https://doi.org/10.1016/j.seppur.2023.123502.
[109] L. Qiao, S. Li, N. Li, et al., Fabrication of monopile polymer foams via rotating gas foaming: hybrid applications in solar-powered interfacial evaporation and water remediation, Sol. RRL 6 (8) (2022) 1–13, https://doi.org/10.1002/solr.202200241.
[110] Y. Lv, R. Xu, K. Zhang, et al., High-performance desalination systems from natural luffa vine: a simple, efficient and environmentally friendly solution for bio-based solar evaporators, J. Clean. Prod. 402 (November 2022)) (2023) 136817, https://doi.org/10.1016/j.jclepro.2023.136817.

[111] Z. Ji, J. Zhao, S. Feng, et al., Insight into the charge-ratio-tuned solar vapor generation of polyion complex hydrogel/coal powder composites, Polymers 15 (11) (2023) 1–13, https://doi.org/10.3390/polym15112449.
[112] Y. Chen, J. Yang, J. Guo, F. Fang, A 3D photothermal bar for efficient steam generation, J. Environ. Chem. Eng. 11 (1) (2023) 109179, https://doi.org/10.1016/j.jece.2022.109179.
[113] L. Chen, Y. Wu, W. Xing, et al., Mechanically robust composite hydrogels for high performance solar driven interface evaporation, Chem. Eng. Sci. 267 (2023) 118330, https://doi.org/10.1016/j.ces.2022.118330.
[114] X. Chen, N. Yang, Y. Wang, et al., Highly efficient photothermal conversion and water transport during solar evaporation enabled by amorphous hollow multishelled nanocomposites, Adv. Mater. 34 (7) (2022) 1–9, https://doi.org/10.1002/adma.202107400.
[115] Y. Li, S. Wang, X. Liu, W. Hong, H. Li, Tuning the heat−salt−water balance for rapid and scalable solar desalination, Appl. Therm. Eng. 230 (PA)) (2023) 120667, https://doi.org/10.1016/j.applthermaleng.2023.120667.
[116] Y. Li, S. Cheng, Z. Yu, R. Gu, Y. Li, H. Chen, Enhanced evaporation performance of solar interface evaporator by modifying the evaporation layer surface with hydrophobic fumed silica, J. Clean. Prod. 392 (September 2022)) (2023) 136302, https://doi.org/10.1016/j.jclepro.2023.136302.
[117] S. Jia, L. Hao, Y. Liu, et al., Freestanding hydrophilic/hydrophobic janus covalent organic framework membranes for highly efficient solar steam generation, ACS Mater. Lett. 5 (2) (2023) 458–465, https://doi.org/10.1021/acsmaterialslett.2c01056.
[118] T. Yang, X. Mu, J. Zhou, et al., A robust Agar–PAM hydrogel for efficient solar steam generation, Sol. RRL 6 (10) (2022) 1–8, https://doi.org/10.1002/solr.202200586.
[119] C. Lei, W. Guan, Y. Guo, et al., Polyzwitterionic hydrogels for highly efficient high salinity solar desalination, Angew. Chem. - Int. Ed. 61 (36) (2022) 1–5, https://doi.org/10.1002/anie.202208487.
[120] M. Yang, H. Luo, W. Zou, et al., Ultrafast solar-vapor harvesting based on a hierarchical porous hydrogel with wettability contrast and tailored water states, ACS Appl. Mater. Interfaces 14 (21) (2022) 24766–24774, https://doi.org/10.1021/acsami.2c03597.
[121] F. Tanzim, B. Subeshan, R. Asmatulu, Improving the saline water evaporation rates using highly conductive carbonaceous materials under infrared light for improved freshwater production, Desalination 531 (December 2021)) (2022) 115710, https://doi.org/10.1016/j.desal.2022.115710.
[122] S. Li, X. Yang, Y. He, et al., Hierarchical porous aero-cryogels for wind energy enhanced solar vapor generation, Cellulose 29 (2) (2022) 953–966, https://doi.org/10.1007/s10570-021-04335-2.
[123] Z. Yu, R. Gu, Y. Zhang, S. Guo, S. Cheng, S.C. Tan, High-flux flowing interfacial water evaporation under multiple heating sources enabled by a biohybrid hydrogel, Nano Energy 98 (April)) (2022) 107287, https://doi.org/10.1016/j.nanoen.2022.107287.
[124] L. Zhang, G. Liu, L. Wu, et al., Integrated light adsorption and thermal insulation of Zn doping 1T phase MoS2-based evaporation prototype for continuous freshwater generation, Chem. Eng. J. 454 (P3)) (2023) 140298, https://doi.org/10.1016/j.cej.2022.140298.
[125] X. Wang, K. Liu, Z. Wang, L. Heng, L. Jiang, A robust and renewable solar steam generator for high concentration dye wastewater purification, J. Mater. Chem. A Mater. 10 (7) (2022) 3436–3442, https://doi.org/10.1039/d1ta10251f.
[126] X. Liang, X. Pei, Y. Yang, et al., A robust PVA/C/sponge composite hydrogel with improved photothermal interfacial evaporation rate inspired by the chimney effect, Desalination 531 (December 2021)) (2022) 115720, https://doi.org/10.1016/j.desal.2022.115720.
[127] M. Khajevand, S. Azizian, B. Jaleh, A bio-based 3D evaporator nanocomposite for highly efficient solar desalination, Sep Purif. Technol. 284 (November 2021)) (2022) 120278, https://doi.org/10.1016/j.seppur.2021.120278.
[128] X. Su, D. Hao, P. Li, et al., Setaria viridis-inspired hydrogels with multilevel structures for efficient all-day fresh water harvesting, J. Mater. Chem. A Mater. 11 (14) (2023) 7702–7710, https://doi.org/10.1039/d3ta00370a.
[129] A. Wang, H. Liang, F. Chen, et al., Facile synthesis of C3N4/NiIn2S4 heterostructure with novel solar steam evaporation efficiency and photocatalytic H2O2 production performance, Appl. Catal. B 310 (January)) (2022) 121336, https://doi.org/10.1016/j.apcatb.2022.121336.
[130] W. Li, X. Tian, X. Li, et al., An environmental energy-enhanced solar steam evaporator derived from MXene-decorated cellulose acetate cigarette filter with ultrahigh solar steam generation efficiency, J. Colloid Interface Sci. 606 (2022) 748–757, https://doi.org/10.1016/j.jcis.2021.08.043.
[131] Y.J. Kim, H.J. Kim, Y.J. Seo, J.H. Choi, H.Y. Koo, W.S. Choi, Solar-driven unmanned hazardous and noxious substance trapping devices equipped with reverse piloti structures and cooling systems, Polymers (Basel) 14 (3) (2022), https://doi.org/10.3390/polym14030631.
[132] P. Wu, X. Wu, Y. Wang, H. Xu, G. Owens, A biomimetic interfacial solar evaporator for heavy metal soil remediation, Chem. Eng. J. 435 (P1)) (2022) 134793, https://doi.org/10.1016/j.cej.2022.134793.
[133] P. Guo, S. Zhang, R. Jin, et al., A super absorbent resin-based solar evaporator for high-efficient various water treatment, Colloids Surf. A Physicochem Eng. Asp. 648 (April)) (2022) 129405, https://doi.org/10.1016/j.colsurfa.2022.129405.
[134] P. Anukunwithaya, J.J. Koh, J.C. Chuan Yeo, et al., A self-regenerating 3D sponge evaporator with a tunable porous structure for efficient solar desalination, J. Mater. Chem. A Mater. 10 (29) (2022) 15743–15751, https://doi.org/10.1039/d2ta03452b.
[135] S. Zhou, J. Zhang, C. Wang, et al., Extremely black carbon nanotube materials with three-dimensional networks for highly efficient solar-driven vapor generation, Nanoscale 14 (46) (2022) 17438–17446, https://doi.org/10.1039/d2nr04857d.
[136] S. Lal, S.K. Batabyal, Potato-based microporous carbon cake: Solar radiation induced water treatment, J. Environ. Chem. Eng. 10 (5) (2022) 108502, https://doi.org/10.1016/j.jece.2022.108502.
[137] L. Zhao, Z. Yang, J. Wang, et al., Boosting solar-powered interfacial water evaporation by architecting 3D interconnected polymetric network in CNT cellular structure, Chem. Eng. J. 451 (P3)) (2023) 138676, https://doi.org/10.1016/j.cej.2022.138676.
[138] L. Cui, C. Ma, P. Wang, H. Che, H. Xu, Y. Ao, Rationally constructing a 3D bifunctional solar evaporator for high-performance water evaporation coupled with pollutants degradation, Appl. Catal. B 337 (June)) (2023) 122988, https://doi.org/10.1016/j.apcatb.2023.122988.
[139] B. Wang, K. Yang, B. Cai, J. Zhang, C. Wei, A. Zhou, A magnetic nanostructure PAC@Fe3O4 driven design toward Janus hydrogel achieves highly efficient solar water evaporation, Chem. Eng. J. 465 (April)) (2023) 142944, https://doi.org/10.1016/j.cej.2023.142944.
[140] Y. Wei, Y. Kong, Q. Yue, et al., Magnetic field assisted synthesis of JANUS Fe3C@Enteromorpha doped graphene aerogels for simultaneous recovery of fresh water and salt in high salinity wastewater, Sep Purif. Technol. 308 (November 2022)) (2023) 122845, https://doi.org/10.1016/j.seppur.2022.122845.
[141] L. Shi, W. Tao, N. Zheng, W. Tang, T. Zhou, Z. Sun, A magnetic-enhanced 3D solar-absorbed structure inspired by cold evaporated heatsink for vapor generation, Chem. Eng. J. 469 (June)) (2023) 143813, https://doi.org/10.1016/j.cej.2023.143813.
[142] Z. Xu, X. Ran, Z. Zhang, et al., Designing a solar interfacial evaporator based on tree structures for great coordination of water transport and salt rejection, Mater. Horiz. 10 (5) (2023) 1737–1744, https://doi.org/10.1039/d2mh01447e.
[143] L. Chen, X. Chen, B. Cui, et al., Salt-resistant agarose-polyvinylpyrrolidone composite hydrogel with pitted-surface towards highly efficient water desalination and purification, Chem. Eng. J. 467 (April)) (2023) 143440, https://doi.org/10.1016/j.cej.2023.143440.
[144] S. Chen, C.G. Yoo, D. Yang, X. Qiu, D. Zheng, Multifunctional lignin-mediated biomass hybrid aerogel with plasmon-enhanced solar-driven desalination and sewage purification, Desalination 556 (January)) (2023) 116572, https://doi.org/10.1016/j.desal.2023.116572.
[145] D. Xie, M. He, X. Li, et al., Tree-inspired efficient solar evaporation and simultaneous in-situ purification of ultra-highly concentrated mixed volatile organic wastewater, Nano Energy 93 (November 2021)) (2022) 106802, https://doi.org/10.1016/j.nanoen.2021.106802.
[146] Y. Kong, Y. Gao, Y. Sun, et al., Manipulating a vertical temperature-gradient of Fe@: Enteromorpha /graphene aerogel to enhanced solar evaporation and sterilization. J. Mater. Chem. A Mater. 10 (7) (2022) 3750–3759, https://doi.org/10.1039/d1ta09807a.
[147] X. Fan, Y. Peng, B. Lv, et al., A siphon-based spatial evaporation device for efficient salt-free interfacial steam generation, Desalination 552 (October 2022)) (2023) 116442, https://doi.org/10.1016/j.desal.2023.116442.
[148] J.G. Qu, R.X. Tang, Q.Y. Cui, J.F. Zhang, Heat-transfer analysis of interfacial solar evaporation and effect of surface wettability on water condensation and collection, Int. J. Therm. Sci. 184 (September 2022)) (2023), https://doi.org/10.1016/j.ijthermalsci.2022.107911.
[149] D. Tong, B. Song, A high-efficient and ultra-strong interfacial solar evaporator based on carbon-fiber fabric for seawater and wastewater purification, Desalination 527 (January)) (2022) 115586, https://doi.org/10.1016/j.desal.2022.115586.
[150] Y. Bu, Y. Zhou, W. Lei, et al., A bioinspired 3D solar evaporator with balanced water supply and evaporation for highly efficient photothermal steam generation, J. Mater. Chem. A Mater. 10 (6) (2022) 2856–2866, https://doi.org/10.1039/d1ta09288j.
[151] Wang S., Chang H., Li L., Wang D., Deng H. Solar Interface Evaporation System Assisted by Mirror Reflection Heat Collection Based on Sunflower Chasing the Sun. ACS Appl Mater Interfaces. 14(39):44958-44968. doi:10.1021/acsami.2c10946.
[152] Y. Qiu, Z. Zhou, C. Zhang, F. Jiang, Q. Zhang, J. Chen, Confined shape-morphing and dual hydration modes for efficient solar steam generation, ACS Energy Lett. 7 (10) (2022) 3476–3483, https://doi.org/10.1021/acsenergylett.2c01700.
[153] H. Cheng, W. Xia, Z. Zhao, et al., Tailoring core@shell structure of Cu2−xSe@PDAs for synergistic solar-driven water evaporation, J. Mater. Sci. 57 (25) (2022) 11725–11734, https://doi.org/10.1007/s10853-022-07353-y.
[154] J. Yan, Q. Wu, J. Wang, et al., Carbon nanofiber reinforced carbon aerogels for steam generation: synergy of solar driven interface evaporation and side wall induced natural evaporation, J. Colloid Interface Sci. 641 (2023) 1033–1042, https://doi.org/10.1016/j.jcis.2023.03.114.
[155] Z. Lei, S. Zhu, X. Sun, et al., A multiscale porous 3D-fabric evaporator with vertically aligned yarns enables ultra-efficient and continuous water desalination, Adv. Funct. Mater. 32 (40) (2022), https://doi.org/10.1002/adfm.202205790.
[156] Z. Zhang, Z. Feng, H. Qi, et al., Carbonized sorghum straw derived 3D cup-shaped evaporator with enhanced evaporation rate and energy efficiency, Sustain. Mater. Technol. 32 (October 2021)) (2022) e00414, https://doi.org/10.1016/j.susmat.2022.e00414.
[157] Z. Yang, D. Yang, C. Yang, et al., Magnetically recyclable 3D water evaporator for desalination and purification of oil-contaminated seawater, Desalination 546 (September 2022)) (2023) 116187, https://doi.org/10.1016/j.desal.2022.116187.

[158] G. Li, Q. Yue, P. Fu, K. Wang, Y. Zhou, J. Wang, Ionic dye based covalent organic frameworks for photothermal water evaporation, Adv. Funct. Mater. 2213810 (2023) 1–9, https://doi.org/10.1002/adfm.202213810.
[159] W. Cai, X. Luo, Z. Lian, et al., Optical-concentrating solar distillation based on three-dimensional copper foam cubes coated with CuS nanoparticles and agarose gel, ACS Appl. Mater. Interfaces 15 (16) (2023) 20120–20129, https://doi.org/10.1021/acsami.3c00838.
[160] X. Zhang, M. Pi, H. Lu, et al., A biomass hybrid hydrogel with hierarchical porous structure for efficient solar steam generation, Sol. Energy Mater. Sol. Cells 242 (April)) (2022) 111742, https://doi.org/10.1016/j.solmat.2022.111742.
[161] C. Hu, W. Li, H.Y. Zhao, et al., Salt-resistant wood-based solar steam generator with top-down water supply for high-yield and long-term desalination of seawater and brine water, Chem. Eng. J. 460 (November 2022)) (2023) 141622, https://doi.org/10.1016/j.cej.2023.141622.
[162] Y. Hu, H. Ma, M. Wu, et al., A reconfigurable and magnetically responsive assembly for dynamic solar steam generation, Nat. Commun. 13 (1) (2022) 4335, https://doi.org/10.1038/s41467-022-32051-3.
[163] J. Sun, R. Teng, J. Tan, et al., An integrated cellulose aerogel evaporator with improved thermal management and reduced enthalpy of evaporation using a hierarchical coordinated control strategy, J. Mater. Chem. A Mater. 11 (12) (2023) 6248–6257, https://doi.org/10.1039/d2ta07122c.
[164] J. Zhu, J. Liu, J. Liu, et al., FDM 3D-printed volcanic-shaped structure for ultrafast solar-driven interfacial evaporation and efficient energy utilization, Desalination 548 (November 2022)) (2023) 116275, https://doi.org/10.1016/j.desal.2022.116275.
[165] Z. Chu, Z. Liu, Z. Li, et al., Hierarchical unidirectional fluidic solar-electro-thermal evaporator for all-day efficient water purification, Mater. Today Sustain. 19 (2022), https://doi.org/10.1016/j.mtsust.2022.100223.
[166] M.H. Sun, C. Li, J. Liu, P. Min, Z.Z. Yu, X. Li, Three-dimensional mirror-assisted and concave pyramid-shaped solar-thermal steam generator for highly efficient and stable water evaporation and brine desalination, ACS Appl. Mater. Interfaces 15 (22) (2023) 27120–27129, https://doi.org/10.1021/acsami.3c02087.
[167] Y. Chen, J. Yang, D. Zhang, et al., A wood-inspired bimodal solar-driven evaporator for highly efficient and durable purification of high-salinity wastewater, J. Mater. Chem. A Mater. 11 (5) (2023) 2349–2359, https://doi.org/10.1039/d2ta08275f.
[168] L.Bin Zhong, S.J. Chen, X. Hou, Q.J. Zhang, C.Y. Guo, Y.M. Zheng, Salt-resistant carbon aerogel with hierarchical interconnected channels for continuous and efficient solar evaporation of hypersaline water, Sci. China Mater. (June) (2023) 1–10, https://doi.org/10.1007/s40843-022-2467-x.
[169] F. Wang, C. Wang, G. Li, et al., Natural wood-derived all-carbon-conductive foam for sustainable all-weather monolithic photo-electrothermal interfacial water evaporation, Mater. Today Nano 23 (2023) 100352, https://doi.org/10.1016/j.mtnano.2023.100352.
[170] H.W. Lim, S.H. Park, S.J. Lee, 3D thermoresponsive hydrogel with enhanced water uptake and active evaporation for effective interfacial solar steam generation, Desalination 550 (December 2022)) (2023) 116368, https://doi.org/10.1016/j.desal.2022.116368.
[171] L. Su, X. Liu, X. Li, et al., Facile synthesis of vertically arranged CNTs for efficient solar-driven interfacial water evaporation, ACS Omega 7 (50) (2022) 47349–47356, https://doi.org/10.1021/acsomega.2c06706.
[172] X. Zhao, T. Wang, Y. Jiang, Q. Lu, J. Pan, Robust and versatile polypyrrole supramolecular network packed photothermal aerogel for solar-powered desalination, Desalination 561 (April)) (2023) 116674, https://doi.org/10.1016/j.desal.2023.116674.
[173] Wilson H.M., Raheman A.R.S., Lim H.W., Lee S.J. Conversion of Hazardous Diesel Soot Particles into a Novel Highly Efficient 3D Hydrogel for Solar Desalination and Wastewater Purification. *ACS Omega*. Published online 2022. doi:10.1021/acsomega.2c07430.
[174] D. Xu, C. Ge, Z. Chen, et al., Tree-inspired braiding fibrous frameworks enabling high-efficiency and salt-rejecting solar evaporation, J. Mater. Chem. A Mater. Publ. Online (2023) 13510–13518, https://doi.org/10.1039/d3ta02029k.
[175] R. Zheng, T. Lin, W.L. Zhao, et al., Hierarchical CoMn-LDH based photothermal membrane with low evaporation enthalpy and narrow bandgap toward highly efficient Solar-Driven evaporation, Chem. Eng. J. 470 (June)) (2023) 144103, https://doi.org/10.1016/j.cej.2023.144103.
[176] R.T. Ginting, H. Abdullah, D.A. Barus, V. Fauzia, Extremely high-efficiency solar steam generation, robust and scalable photothermal evaporator based on ZIF-67@MXene/rGO decorated rock wool, J. Mater. Chem. A Mater. 11 (10) (2023) 5296–5308, https://doi.org/10.1039/d2ta09778h.
[177] X.P. Li, X. Li, H. Li, et al., Reshapable MXene/graphene oxide/polyaniline plastic hybrids with patternable surfaces for highly efficient solar-driven water purification, Adv. Funct. Mater. 32 (15) (2022) 1–13, https://doi.org/10.1002/adfm.202110636.
[178] J. Ren, L. Chen, J. Gong, J. Qu, R. Niu, Hofmeister effect mediated hydrogel evaporator for simultaneous solar evaporation and thermoelectric power generation, Chem. Eng. J. 458 (December 2022)) (2023) 141511, https://doi.org/10.1016/j.cej.2023.141511.
[179] Y. Liu, Y. Cui, C. Yang, et al., Expired yogurt-derived, three-dimensional water evaporator with sustainable self-cleaning and high mechanical properties for the desalination and purification of oil-contaminated seawater, Desalination 550 (October 2022)) (2023) 116405, https://doi.org/10.1016/j.desal.2023.116405.
[180] H.M. Wilson, H.W. Lim, S.J. Lee, Highly efficient and salt-rejecting poly(vinyl alcohol) hydrogels with excellent mechanical strength for solar desalination, ACS Appl. Mater. Interfaces 14 (42) (2022) 47800–47809, https://doi.org/10.1021/acsami.2c14885.
[181] D. Pan, X. Deng, Y. Ge, Y. He, X. Cui, Preparation of a low-cost electric compensation photothermal evaporator for all-weather-available and efficient evaporation, Sol. Energy 259 (February)) (2023) 151–164, https://doi.org/10.1016/j.solener.2023.05.022.
[182] P. Liu, L. Xu, Z.Y. Wang, et al., A salt-resistant and antibacterial Cu2ZnSnS4-based hydrogel for high efficient photothermal distillation in seawater desalination and sewage purification, ChemSusChem (2023), https://doi.org/10.1002/cssc.202300611 (Published online).
[183] L. Li, L. Du, Y. Bai, et al., A highly efficient and durable solar evaporator based on hierarchical ion-selective nanostructures, EcoMat 5 (2) (2023), https://doi.org/10.1002/eom2.12289.
[184] J. He, N. Li, S. Wang, et al., Efficient solar-powered interfacial evaporation, water remediation, and waste conversion based on a tumbler-inspired, all-cellulose, and monolithic design, Adv. Sustain Syst. 6 (10) (2022), https://doi.org/10.1002/adsu.202200256.
[185] J. Yang, X. Suo, X. Chen, S. Cai, X. Ji, H. Qiao, Water-light induced self-blacking system constituted by quinoa cellulose and graphene oxide for high performance of salt-rejecting solar desalination, Adv. Sustain. Syst. 6 (1) (2022), https://doi.org/10.1002/adsu.202100350.
[186] Z. Chen, J. Wang, H. Zhou, et al., Janus nano-micro structure-enabled coupling of photothermal conversion, heat localization and water supply for high-efficiency solar-driven interfacial evaporation, Adv. Funct. Mater. (2023), https://doi.org/10.1002/adfm.202303656 (Published online).
[187] H. Zou, X. Meng, X. Zhao, J. Qiu, Hofmeister effect-enhanced hydration chemistry of hydrogel for high-efficiency solar-driven interfacial desalination, Adv. Mater. (2022), https://doi.org/10.1002/adma.202207262 (Published online).
[188] X. Li, Y. Tian, P. Zhang, et al., A lotus-petiole-inspired hierarchical design with hydrophilic/hydrophobic management for enhanced solar water purification, Adv. Funct. Mater. (2023), https://doi.org/10.1002/adfm.202302019 (Published online).
[189] X. Chen, P. Li, J. Wang, et al., Multishelled CuO/Cu2O induced fast photo-vapour generation for drinking water, Nano Res. 15 (5) (2022) 4117–4123, https://doi.org/10.1007/s12274-021-4063-y.
[190] Y. Li, S. Cheng, B. Jin, Z. Yu, R. Gu, A three-dimensional folded multistage distillation device with enhanced air convection for efficient solar interface evaporation, Desalination 562 (May)) (2023) 116714, https://doi.org/10.1016/j.desal.2023.116714.
[191] C. Wang, K. Xu, G. Shi, D. Wei, Water skin effect and arched double-sided evaporation for boosting all-weather high salinity desalination, Adv. Energy Mater. 13 (21) (2023), https://doi.org/10.1002/aenm.202300134.
[192] B. Luo, J. Wen, H. Wang, et al., A biomass-based hydrogel evaporator modified through dynamic regulation of water molecules: highly efficient and cost-effective, Energy Environ. Mater. 6 (3) (2023), https://doi.org/10.1002/eem2.12353.
[193] S.Y. Zheng, J. Zhou, M. Si, et al., A molecularly engineered zwitterionic hydrogel with strengthened anti-polyelectrolyte effect: from high-rate solar desalination to efficient electricity generation, Adv. Funct. Mater. (2023), https://doi.org/10.1002/adfm.202303272 (Published online).